Rostock University

A calorimetric study of non-equilibrium structures on fast cooling (100 000 K/s)

Dissertation

for obtaining the academic degree
doctor rerum naturalium (Dr. rer. nat.)
of the Faculty of Mathematics and Natural Science
of Rostock University

submitted by

Serguei Adamovski,

born on 20.03.1972 in Kirovograd, Ukraine

Potsdam, July 2010

Gutachter:

1. Prof. Dr. Christoph Schick,
   Institut für Physik
   Mathematisch-Naturwissenschaftliche Fakultät
   Universität Rostock
   18051 Rostock, Germany

2. Prof. Dr. Leslie H. Allen,
   Department of Materials Science and Engineering
   University of Illinois at Urbana-Champaign,
   Illinois 61801, USA

Verteidigungsdatum: 26.11.2010.

Contents

Definition of symbols

Symbol	Description
t	Time
ω	Angular frequency
T	Temperature
$\dot{T}$	Scanning rate, $=dT/dt$
T_s	Sample temperature
T_{prog}	Program temperature
T_0	Oven temperature, base temperature
T_B	"Bias temperature", average overheating during AC-measurements
δT	Amplitude of temperature oscillations
T_{AV}	Average temperature over a period of oscillations
Q	Exchanged heat
q	Heat flux: exchanged heat per unit of area per unit of time
δq	Heat flux amplitude
P	Heater power
δP	Amplitude of power oscillations
C	Heat capacity
c	Specific heat capacity
C_s	Sample heat capacity
C_{add}	Addenda heat capacity
ρ	Density
λ	Thermal conductivity
L	Length
l	(Thermal) wavelength

Chapter 1. Motivation

Properties of materials are known to depend on processing conditions. For example, since thousands of years, there exists a secret of Damascus steel. And only recently the reason of its outstanding properties was discovered [1]. This reason is a special non-equilibrium structure developed during repeated heating-cooling cycles in combination with a mechanical treatment.

If very hot steel is cooled down fast (like placed into cold oil), it will be very hard and brittle. If it is cooled slowly (like cooled down with the oven), it will be not so hard. At high temperature iron crystalline structure is a face-centered cubic (FCC) – so-called γ-iron; the solubility of carbon is high. Upon cooling at a transition temperature iron changes to body-centered cubic (BCC) – α-iron; the carbon solubility is less than in γ-iron; the rest of carbon should be removed from the lattice. If the material is cooled down slowly, the carbon atoms can diffuse through the matrix and agglomerate somewhere. However, if the steel is quenched, the carbon atoms will remain distributed among the material, but they will be pushed out of the unit cell, creating crystal defects. This is what gives hardness to the steel. There are other materials like polymers, where cooling conditions and generally the thermal history strongly influences the properties of the final product.

Therefore, studying of materials during and just after a thermal treatment is very important for making parts with desired properties. For such a study, one should be able to investigate materials at cooling rates relevant to the production process. Polymers are cooled down at about 1000 K/s during injection molding or extrusion. Cooling rates of 10^4 to 10^7 K/s are achieved by melt spinning to obtain some metal alloys in amorphous state.

Most of available techniques do not allow measurements at such scanning rates. Widely used Differential Scanning Calorimetry (DSC) allows scanning the temperature up to 200 K/min (3 K/s). "High performance DSC", an improvement to the standard technique called HPer DSC [2] or HyperDSC™ [3], allows to heat at up to 500 K/min (approx. 10 K/s), but still cooling at only 300 K/min (5 K/s) is possible. Time resolution is limited to 10…30 s as the best. It is possible to quench the sample putting it on a cold plate and then to place it into the calorimeter, but about the first minute after the quenching gets lost.

To cool faster, one can take a thin sample, move it rapidly from a hot region into the cold region of an apparatus and then observe the crystallization process optically [4-6]. Cooling rates up to 30 K/s are reachable with this technique, which is still slow. Cooling rates up to 2 000 K/s were achieved by water spraying [6], but one can hardly control the process and execute an advanced time-temperature program.

On the other hand, there are "fast" calorimetric methods available. An "Exploding wire" [7], also called "Pulse heating" [8] technique allows to heat the sample very fast, although it is mostly limited to conductive samples. An amazing technique was developed by the group of L. Allen which allows to heat also polymer samples as fast as 1 000 000 K/s [9] . However, none of these methods is designed for cooling experiments.

The aim of this work was to investigate kinetics of structure formation during and after cooling at high rates, which were not available before. For this purpose, a calorimeter had to be developed, which would be capable of performing measurements during such cooling as well as isothermal or fast heating scans immediately after cooling. Crystallization kinetics of poly(ε-caprolactone) (PCL), polyethylene (PE), syndiotactic polypropylene (sPP) with different content of carbon nanotubes as well as series of monodisperse n-alkanes was studied using the new technique.

Structure of the thesis is as follows: theory of calorimetry relevant to the objective of this work is summarized in Chapter 2. Chapter 3 gives an insight into the instrument development and presents measurements of crystallization kinetics for some polymer materials. Different measurement strategies are discussed; short studies on polymer materials uncover possibilities and limitations of the technique. Chapter 4 is focused on crystallization of monodisperse n-alkanes, which is important for the fundamental understanding of the behavior and properties of common used polymer materials like polyethylene. Chapter 5 gives an overview of the open questions and future possibilities of the method followed by the summary of the work. Electronics and the software are described in the appendices A, B and C.

Chapter 2. Theory of calorimetry

Calorimetry is the domain of measurement techniques used for determination of heat effects involved in various physical, chemical or biological processes [10].

2.1. Heat balance equation

If some amount of heat ΔQ is applied to an object, its temperature is increased by ΔT. The relation between these two values is one of the most important intrinsic properties of any object. It is heat capacity C. Heat capacity is defined by the equation:

$$\Delta Q = C \cdot \Delta T \tag{2.1}$$

As heat capacity itself is temperature dependent, the temperature change should be small.

Speaking of material properties, one uses specific heat capacity, i.e. heat capacity per unit of amount – for example per gram, per mole or per cubic meter. We will use mass as a measure of sample amount, specific heat is then $c = C/m$.

An apparatus for calorimetric measurements is called calorimeter. A calorimeter consists of a calorimetric cell, to which a sample is thermally connected; the surroundings with defined conditions and other equipment used to measure and control the experimental parameters as well as for data acquisition and data processing. Often a "thermostat" is used to keep the temperature of the surroundings constant.

2.1.1. Adiabatic calorimetry

A "classical" way of measurement of heat capacity is adiabatic calorimetry. The sample is in adiabatic conditions. Certain amount of heat is supplied to the sample; corresponding temperature change of the sample is measured. Heat capacity is defined by equation (2.1). This is the most "direct" way of measuring heat capacity. However, it is time consuming because one has to wait until temperature is equilibrated before and after adding of the heat. Another disadvantage is that this method works only on heating. Isothermal studies as well as measurements on cooling are not possible.

2.1.2. Scanning mode

Mostly used way of heat capacity measurement is scanning the temperature at certain rate. There is a spectrum of devices available from companies like Perkin Elmer, TA Instruments, Setaram, Mettler Toledo, Netzsch and many others to measure heat capacity by scanning the temperature.

Equation (2.1) should be fulfilled for each (small) time interval dt:

$$\frac{dQ}{dt} = C \cdot \frac{dT}{dt} \tag{2.2}$$

Equation (2.2) describes the situation where total heat flow rate to the sample is known. If a heater is attached to the sample, heater power P is measured instead (in differential systems, power difference is measured to improve the sensitivity). The sample is held by some support ("addenda") with its own heat capacity C_{add} that is added to the heat capacity C_s of the sample. In this case, the following equation describes the heat exchange.

$$P = (C_s + C_{add}) \cdot \frac{dT}{dt} + \xi \tag{2.3}$$

Function ξ represents heat transfer between the sample cell and the surrounding ("heat losses"). In *adiabatic* scanning calorimeters, heat exchange between the sample and the surrounding is negligible, so this function is zero or very small. In *heat flux* calorimeters (for example *Tian-Calvet* type [11]), there is no heater directly attached to the sample and $P = 0$; heat losses function ξ is measured using a thermopile. In *differential heat flux* calorimeters, heat flow rate to the addenda on the sample side and the reference side are assumed equal, so measured difference in heat losses equals heat flow rate to the sample. In *differential power compensated* calorimeters, the heat losses are assumed the same for a "sample cell" and a "reference cell" and therefore difference in the heater powers equals heat flow rate to the sample. The calorimeter *described in this work* is neither *heat flux* nor *power compensated* and it is not *differential*; its heat losses function is calibrated as discussed in section 3.2.1 on page 14.

2.1.3. AC-calorimetry

To measure the objects heat capacity, one should essentially change its temperature. This makes it impossible to study changes of material properties with time under isothermal conditions. One way to overcome this problem is known as AC-calorimetry. The idea is to change slightly the sample temperature periodically around some constant or slowly changing average value. The amplitude of temperature modulation should be small enough not to influence the process in the sample. Periodic part of heat flow connected to this temperature oscillation contains information about heat capacity. An additional advantage of this technique in comparison to other methods is the better signal-to-noise ratio due to selective detection at a certain frequency.

First used by Corbino [12, 13], AC technique has got its development for heat capacity measurements in the 60-th of the last century. Kraftmakher used at the beginning the sample (metal

wire) simultaneously as heater and thermometer [14]; later he changed to a separate temperature sensor [15]. Handler et al. [16] used chopped light at 26 Hz to measure heat capacity of nickel as a function of temperature near the critical point. Sullivan and Seidel [17] have introduced quasi-adiabatic and quasi-static conditions:

$$\omega \cdot \tau_{ext} \gg 1 \tag{2.4}$$

$$\omega \cdot \tau_{int} \ll 1 \tag{2.5}$$

Here ω is modulation angular frequency, τ_{int} - internal time constant of the system heater-sample-thermometer; τ_{ext} – sample-to-bath relaxation time. Under quasi-adiabatic conditions (2.4), thermal connection to the thermostat does not have to be included in the AC equation; quasi-static conditions (2.5) mean good thermal contact between the heater, the sample and the thermometer as well as high thermal conductivity of the sample, so that thermal equilibrium inside the system heater-sample-thermometer establishes much faster then the period of oscillations.

If conditions (2.4) and (2.5) are met, data treatment simplifies significantly. To describe the situation with a temperature, oscillating at angular frequency ω, one should separate power and temperature to the "average" (subscript "av") and the "oscillating" (subscript "ω") parts: $P = P_{av} + P_{\omega}$, $T = T_{av} + T_{\omega}$. For harmonic oscillations $P_{\omega} = \delta P \cdot e^{i\omega t}$ and $T_{\omega} = \delta T \cdot e^{i(\omega t + \varphi)}$. Here δP and δT are amplitudes of power and temperature respectively; φ is the phase shift between them. For the oscillating part, heating rate is a multiple of the temperature with complex factor $i\omega$:

$$\dot{T}_{\omega}(t) = \frac{dT_{\omega}(t)}{dt} = \frac{d}{dt}\left(\delta T \cdot e^{i(\omega t + \varphi)}\right) = i\omega \cdot \delta T \cdot e^{i(\omega t + \varphi)} = i\omega \cdot T_{\omega}(t) \tag{2.6}$$

Equation (2.2) should hold for the oscillating part: $P_{\omega} = C \cdot \dot{T}_{\omega}$; so $\delta P = C \cdot i\omega \cdot e^{i\varphi} \cdot \delta T$. In ideal case the phase shift $\varphi = -\frac{\pi}{2}$, so $i \cdot e^{i\varphi} = 1$ and the simplified equation is:

$$\delta P = C \cdot \omega \cdot \delta T \tag{2.7}$$

Actually heat capacity can be a complex value [18, 19]; in this case amplitudes of power and temperature in (2.7) should be calculated as complex values (with the same phase reference) taking into account the shift of $\varphi = -\frac{\pi}{2}$ mentioned above. Equation (2.7) is the main equation for temperature-modulated calorimetry. It is worth to say that fast cooling possibility is needed for measurements at high modulation frequencies.

With this method, one can measure heat capacity quasi-isothermally as a function of time. This allows following crystallinity (solid fraction) χ with time because sample heat capacity depends on crystallinity as

$$c = \chi \cdot c_{cr} + (1 - \chi) \cdot c_{am} + c_{ex} \qquad (2.8)$$

Here c is the measured specific heat capacity of the sample; c_{cr} is specific heat capacity of the crystalline phase, c_{am} is that of the amorphous phase; c_{ex} is the excess heat capacity (it is discussed for example in [20]). Equation (2.8) holds also below glass transition, where $c_{am} \approx c_{cr}$ and $c_{ex} = 0$.

For most polymers, specific heat capacity of amorphous phase c_{am} is noticeable higher than that of the crystalline phase c_{cr} at temperatures between glass transition and melting. From equation (2.8) one gets crystallinity of the sample:

$$\chi = \frac{c_{am} + c_{ex} - c}{c_{am} - c_{cr}} \qquad (2.9)$$

Therefore, heat capacity can be used as measure of crystallinity of the sample if $c_{ex} = 0$. AC-technique was already utilized for such measurements before; see for example [21, 22]. In this work, AC technique was used to study crystallization kinetics of poly(ε-caprolactone) (PCL).

2.2. Fast scanning

In many cases, scanning rate is selected according to the convenient sample size and the measuring device used. However, if sample properties are rate-dependent and high scanning rates are needed, then additional limitations should be taken into account.

For thermal measurements it is known, that there is the problem of temperature difference between sample and sensor – the so-called "heat transfer problem" [23, 24]. At high rates, also the heat transfer inside the sample becomes an important factor. In most cases, the sample is heated and cooled from outside, so the heat has to propagate through the sample. Due to the finite thermal conductivity of the sample material, this leads to a temperature difference between different parts of the sample and smearing of transition peaks. To avoid this problem, the sample should be thin.

Another limitation is cooling possibility. For heating, one can use for example electrical heater or absorption of light or microwave energy. There are lightweight high power sources available, so high heating rate can be easily obtained. For cooling, Peltier effect can be used; however, cooling power is limited by Joule heating, so today available Peltier coolers cannot cool very fast. Usually, the sample is connected to a cold block by means of some cooling agent. Properties of the cooling

agents' material restrict the highest possible cooling rate. Numerical estimation of these two effects is presented in the following sections.

2.2.1. Sample size

To estimate the influence of the sample size on the maximum scanning rate, assume a disc-shaped sample with specific heat capacity c, density ρ, thermal conductivity λ, area S and thickness L, see Figure 2.1. The sample is heated uniform from one side at constant heating rate dT/dt and has adiabatic conditions on all other surfaces.
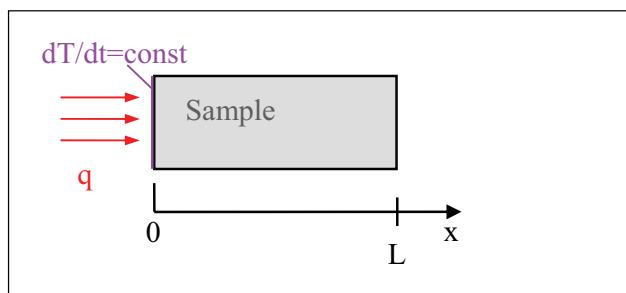
Figure 2.1: Scheme of a sample for calculation of the temperature gradient across the sample. Disk thickness L is usually much smaller than the lateral dimensions of the sample; it is shown disproportional for visual demonstration.

At each distance x from the heated surface, power needed to heat the rest of the sample at a given heating rate is $dQ/dt = \rho \cdot c \cdot S \cdot (L-x) \cdot dT/dt$, so the heat flux is $q(x) = \rho \cdot c \cdot (L-x) \cdot dT/dt$. This heat flux creates a temperature gradient at each x position: $dT/dx = q(x)/\lambda$. Total temperature difference between $x = 0$ and $x = L$ is

$$\Delta T = \int_0^L \frac{dT}{dx} dx = \frac{L^2 \rho c}{2\lambda} \cdot \frac{dT}{dt} \tag{2.10}$$

For a polymer sample with $c = 1.3$ J/gK, $\rho = 900$ kg/m³, $\lambda = 0.15$ W/mK, $L = 0.5$ mm, $dT/dt = 1$ K/s (60 K/min), which is normal for DSC technique, temperature difference across the sample is 1.0 K. At heating rate of 1000 K/s, a 0.1 mm thick sample would have temperature difference of 39 K; thickness of 20 μm reduces the temperature difference to 1.6 K at this rate. At heating rate of 10 000 K/s, temperature difference of 1.0 K appears already on a 5-μm thin sample. Heat losses from the opposite to the heater side of the sample will increase the temperature difference across the sample additionally.

For a measurement, the sample is usually placed on some support with a heater and a thermometer; this adds some heat capacity to the sample. If the sample is small, these addenda should be small either to maintain good signal to noise ratio.

2.2.2. Cooling agent

Another important point for high cooling rates is the choice of the cooling agent. Consider a system consisting of a thin sample placed at the flat face of a "cold finger" – a uniform rod with a specific heat capacity c, density ρ, thermal conductivity λ, and length L. The other face of the rod is coupled to a heat sink, which is kept at a low temperature T_0 (Figure 2.2). The temperature of the sample/rod interface is controlled by a thin flat heater with a negligible heat capacity and thermal resistance.
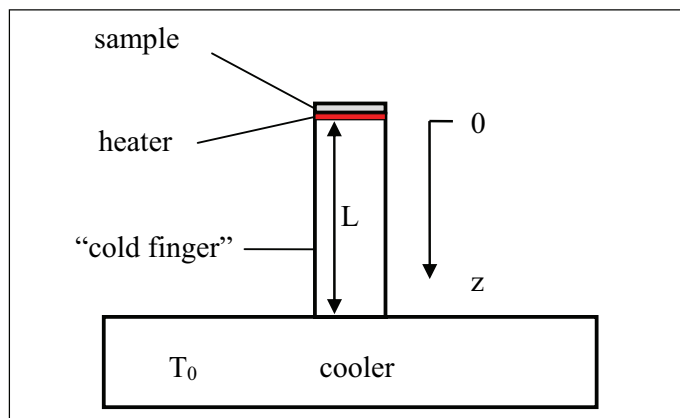
Figure 2.2: Scheme of the system with a "cold finger". The cell with the sample is placed at the flat face of a "cold finger" coupled with a cooler, which is kept at a low temperature T_0. The temperature of the sample is controlled by a thin heater located at the face of the finger.

Assume ideal thermal contacts between the sample, the heater and the rod as well as between the rod and the cooler. To determine the upper limit of the scanning rate first consider the sample is small enough so that its heat capacity can be neglected. A uniform heat flux $q(t)$ is supplied to the face of the rod at $z = 0$ and transmitted along the rod (Z-axis). The heat leakage from the lateral surface of the rod is neglected. The temperature distribution in the rod $T(z,t)$ is described by Fourier's heat-transfer equation:

$$\rho c \frac{\partial T(z,t)}{\partial t} = \lambda \frac{\partial^2 T(z,t)}{\partial z^2} \tag{2.11}$$

Usually, the sample temperature is scanned linearly with time. However, for simplicity, we will assume harmonic temperature oscillations; this will not remarkably change the result. More precise calculations for the case of linear heating/cooling can be found in [25].

Consider a harmonic heating-cooling process with angular frequency ω. The sample temperature is driven by a periodic heat flux $q(t) = \delta q \cdot (1 + e^{i\omega t})$ with an amplitude δq (the flux is changed in the

range from 0 to $2\delta q$). According to Eq. (2.11) the amplitude of the temperature oscillation of the rod surface $z = 0$ equals

$$\delta T = \frac{\delta q}{\sqrt{\omega \rho c \lambda}}, \tag{2.12}$$

provided the thermal wavelength $l = (2\lambda/\omega\rho c)^{1/2}$ is small with respect to the rod length L and reflection of thermal waves at $z = L$ can be therefore neglected.

The amplitude of scanning rate according to (2.6) and (2.12) is

$$\delta \dot{T} = \omega \cdot \delta T = \delta q \sqrt{\frac{\omega}{\rho c \lambda}} \tag{2.13}$$

The rate increases with ω. The maximum angular frequency ω is limited by the smallest acceptable scanning amplitude $\delta T^{\min}$: $\delta T \geq \delta T^{\min}$. According to (2.12), $\delta q/(\omega\rho c\lambda)^{1/2} \geq \delta T^{\min}$, or for the scanning rate using (2.13):

$$\left(\frac{dT}{dt}\right)^{\max} = \delta \dot{T}^{\max} = \frac{\delta q^2}{\rho c \lambda \cdot \delta T^{\min}} \tag{2.14}$$

Next, the temperature of the rod surface is oscillating around the average value $T_{AV} = T_0 + T_B$ that is essentially higher than T_0. To estimate the value of bias temperature T_B, one can divide the heat flux from the heater into DC ("average") and AC ("oscillating") components and calculate corresponding temperature changes separately using superposition principle. Average heat flux equals δq (as mentioned before, heat flux changes from 0 to $2\delta q$), so from the definition of thermal conductivity for the rod follows

$$T_B = \frac{\delta q \cdot L}{\lambda} \tag{2.15}$$

The largest acceptable bias temperature $T_B^{\max}$ is restricted by the possibilities of the cooling system. Note that the amplitude of the temperature oscillations cannot be larger than T_B.

One can substitute the value of δq from (2.15) into (2.14) using the largest acceptable value of bias temperature $T_B^{\max}$:

$$\left(\frac{dT}{dt}\right)^{\max} = \frac{\lambda}{\rho c} \cdot \frac{1}{\delta T^{\min}} \cdot \left(\frac{T_B^{\max}}{L}\right)^2 \tag{2.16}$$

As one can see from (2.16), the highest cooling rate can be obtained using the cooling medium with the highest value of diffusivity ($\lambda/\rho c$). Properties of selected materials are presented in Table 2.1. The best materials as cooling medium for the highest cooling rate are helium, silver, hydrogen, gold and copper.

Equation (2.16) was derived for the highest cooling rate only. In fact, we are interested in the heat flux from the sample (in the case of a thin sample[1]), which is fixed. Therefore, amplitude of heat flux from the heater δq is not a free parameter. The ratio between the heat flux from the sample and heat flux from the heater determines sensitivity of the instrument: smaller range of δq gives better sensitivity to the signal from the sample.

Therefore, one should leave δq in (2.14) and substitute λ from (2.15); the resulting limit for heating rate is

$$\left(\frac{dT}{dt}\right)^{\max} = \frac{1}{\rho c} \cdot \frac{\delta q}{L} \cdot \frac{T_B^{\max}}{\delta T^{\min}} \tag{2.17}$$

For heat capacity measurements at the highest cooling rate one should choose according to (2.17) materials with the lowest value of volumetric heat capacity ($\rho \cdot c_p$) as cooling medium. Table 2.1 is sorted ascending by this value. From materials listed, gases are the most suitable cooling agents.

Table 2.1: Heat capacity (c_p), thermal conductivity (λ), density (ρ) and their combinations for selected substances at room temperature (if not stated otherwise) [26, 27], sorted by volumetric heat capacity $\rho \cdot c_p$.

Substance	c_p	λ	ρ	$\rho \cdot c_p$	$\lambda/(\rho \cdot c_p)$
	J/(g·K)	W/(m·K)	kg/m^3	J/(m^3·K)	m^2/s
helium (He) (25 °C)	5.2	0.1546	0.1636	8.51E+02	1.82E-04
air 300 K	1.007	0.0262	1.161	1.17E+03	2.24E-05
hydrogen (H$_2$) (25 °C)	14.3	0.1859	0.0824	1.18E+03	1.58E-04
nitrogen (N$_2$) (25 °C)	1.039	0.0259	1.1449	1.19E+03	2.18E-05
polymer (25 °C)	1.3	0.15	900	1.17E+06	1.28E-07
chloroform	0.96	0.117	1483.2	1.42E+06	8.22E-08
xylene	1.72	0.13	864	1.49E+06	8.75E-08

---

[1] In case of a droplet sample, "heat flow rate from the sample" and "heater power" should be considered instead of heat fluxes.

Substance	c_p	λ	ρ	$\rho \cdot c_p$	$\lambda/(\rho \cdot c_p)$
	J/(g·K)	W/(m·K)	kg/m³	J/(m³·K)	m²/s
silicon (Si) (300 K)	0.702	124	2328.3	1.63E+06	7.59E-05
germanium (Ge) (300 K)	0.3219	64	5323.4	1.71E+06	3.73E-05
acetone	2.18	0.161	790	1.72E+06	9.35E-08
ethyl alcohol	2.44	0.169	789.3	1.93E+06	8.78E-08
aluminum (Al)	0.897	237	2700	2.42E+06	9.79E-05
silver (Ag)	0.235	429	10500	2.47E+06	1.74E-04
gold (Au)	0.129	317	19300	2.49E+06	1.27E-04
platinum (Pt)	0.133	71.6	21500	2.86E+06	2.50E-05
copper (Cu)	0.385	401	8960	3.45E+06	1.16E-04
iron (Fe)	0.449	80.2	7870	3.53E+06	2.27E-05
nickel (Ni)	0.444	90.7	8900	3.95E+06	2.30E-05
water (H₂O) (30 °C)	4.1784	0.6154	995.65	4.16E+06	1.48E-07

Even smaller values of ($\rho \cdot c_p$) can be obtained at reduced pressure because volumetric heat capacity decreases with pressure (linear in ideal case). Thermal conductivity, which is responsible for the relation between T_B and L, does not change significantly with reduction of pressure until the mean free path of gas molecules becomes comparable to the distance L from the sample to the cold surface.
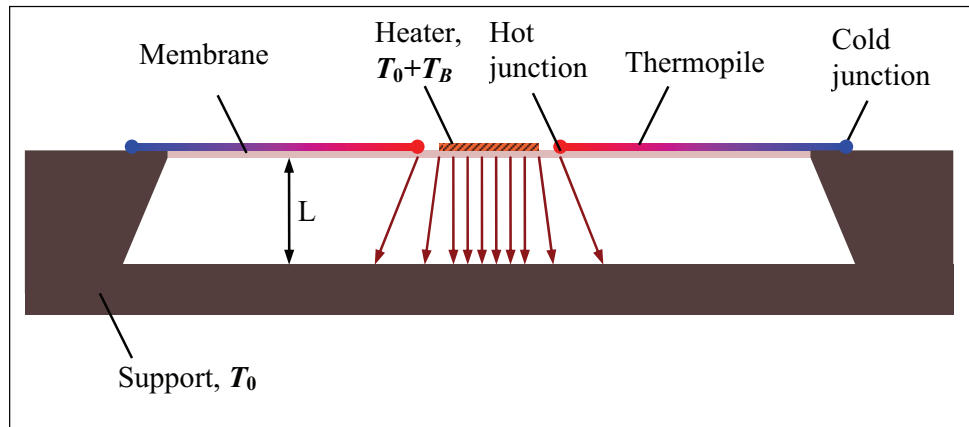
Figure 2.3: Scheme of the gas pressure gage TCG3880. Small heater (50x100 µm²) is located on the thin (0.5 µm) membrane, surrounded by hot junctions of a thermopile. Heat dissipates through the gas towards thick substrate; distance from the heater to the substrate L = 0.3 mm.

Pressure dependence of the gas thermal conductivity can be seen from the calibration curves of gas pressure/thermal conductivity gage Xensor TCG3880. Scheme of the sensor is presented in Figure 2.3. Temperature difference between the heater and the substrate measured by the thermopile corresponds to the bias temperature in Figure 2.2. Thermal conductivity is obtained from the bias temperature according to (2.15). The sensor does not exactly correspond to the "cold finger" model;

it can be described by some combination of "cold finger" and spherical symmetry. However, general behaviour does not change significantly.

Output voltage U_{tc} of the thermopile at constant heater power is plotted versus gas pressure for four gases in Figure 2.4. The voltage is in first approximation proportional to the bias temperature ($U_{tc} \sim T_B$) so it is reverse proportional to the thermal conductivity ($\lambda \sim 1/U_{tc}$). At pressures below 10 Pa, output voltage deviates from logarithmic increase with decrease of pressure due to the pressure-independent heat flow through the membrane, which exists also at high pressures. For example, in helium at pressure above 10 kPa, output voltage (~11 mV) is about 1/20 of the value in vacuum (200 mV). This means heat flow through the membrane in helium at 10 kPa is in the order of 1/20 of the total heat flow.
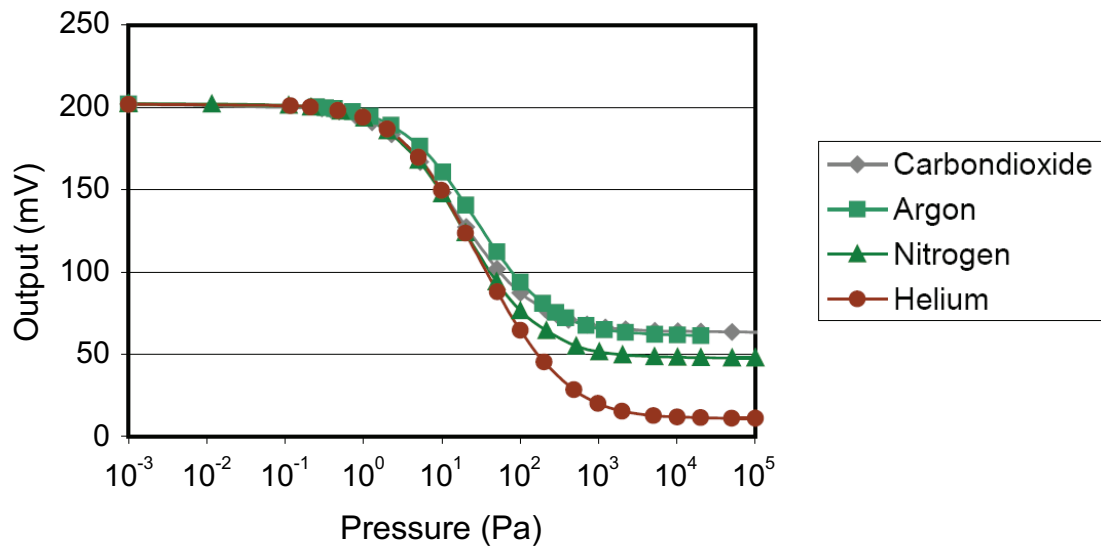
Figure 2.4: Sensor TCG 3880 [28]: output voltage versus gas pressure for different gases.

On the high-pressure side, there is almost no change of the gas thermal conductivity down to 10 kPa (see Figure 2.4). At 1 kPa, there is already noticeable pressure dependence of the measured voltage, so the measurement will be sensitive to the gas pressure. Reduced pressure of about 10 kPa was therefore used for most of the measurements presented in this work.

Chapter 3. Instrument development

In this chapter, the instrumental development is presented in historical order. Several steps of development of the sensor as well as electronics design are shown. We have started with the sensor TCG3880, which was designed by the manufacturer as pressure gage. During development, other sensors with enhanced characteristics for heat capacity measurements became available through collaboration with the manufacturer of the sensors.

For the proof of principle, stand-alone complete devices like generator, lock-in amplifier and oscilloscope were used. When it became clear that the principle works, a computer controlled system was constructed. With the time, there was a need in a second system (workplace); therefore, it was built taking into account the drawbacks of the first one.

Advantages of each system are described in the following sections.

3.1. Sensor construction

As it follows from the theory, very fast cooling requires a sensor to be light and cooling medium to be a gas. The sensor could be a very thin membrane with a heater and a thermometer made on it. At the beginning we have used a commercially available vacuum gauge TCG-3880, produced by Xensor Integration, NL [28].

The sensor is presented in Figure 3.1. The main part is a thin SiN_x membrane (thickness ca. 500 nm, size 1x2 mm^2). In the center of the membrane there is a resistive heater surrounded by six "hot" junctions of a semiconductive thermopile; see Figure 3.1 (b) and (c). A sample is placed between the heater stripes, as described in section 3.3.3 ("Sample preparation").
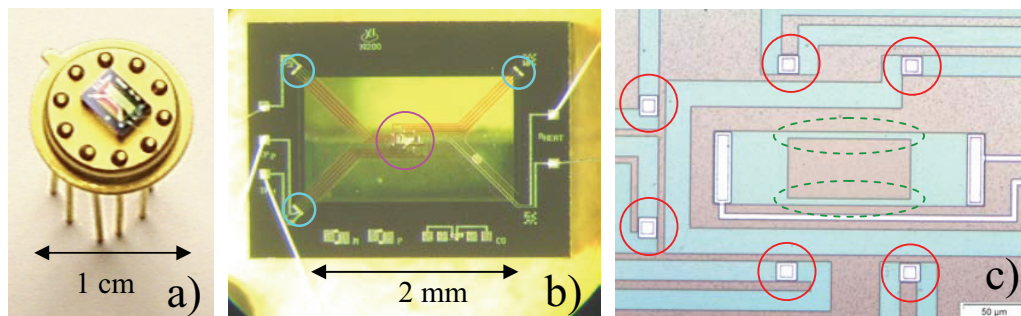
Figure 3.1: Sensor TCG3880: a) a chip on standard TO-10 housing; b) enlarged membrane with a sample: heated area with a sample are inside a pink circle; turquoise circles show "cold" thermocouple junctions; c) enlarged central part of the membrane: red circles mark "hot" thermocouple junctions; green dashed ovals show two heater stripes.

A scheme of the sensor is shown in Figure 3.2. The sample is heated by the heater and its temperature is measured by the thermopile.
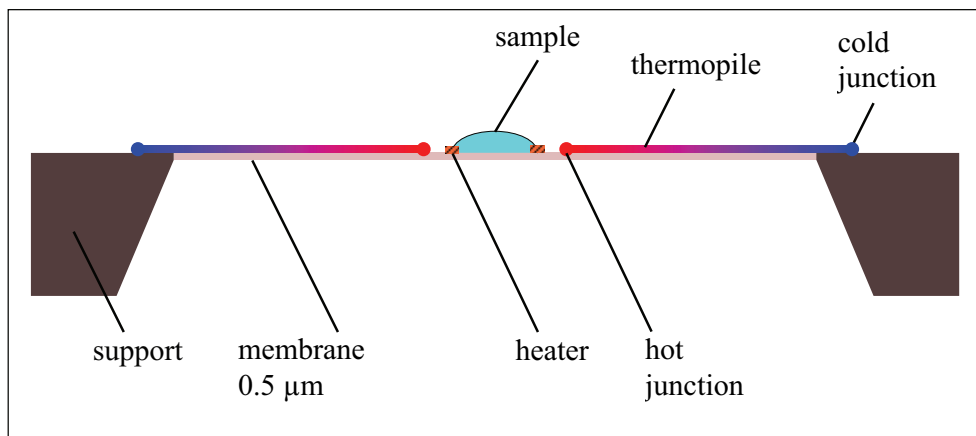
Figure 3.2: Scheme of the sensor TCG3880 for calorimetric measurements.

Heater and sample are small (the heater is 50 µm wide – see Figure 3.1) and the hot junctions of the thermopile are close to the heater (50 µm for four of six junctions). The polymer sample after melting sticks to the membrane providing a good thermal contact. Therefore, we initially assume that the temperature difference between the sample and the hot junctions of the thermopile can be neglected. Thermopile cold junctions are on a thick silicon frame that is in good thermal contact with the holder. Thus, the cold junction temperature is the temperature of the holder T_0. The thermopile measures the overheating (T_s-T_0) of the sample against the ambient temperature; the latter is measured by an additional copper-constantan thermocouple. Temperature distribution is discussed in more detail in section 3.5.5 on page 47.

3.2. Modes of operation

Different modes of operation are possible with the sensor. Scanning, quasi-isothermal and modulated modes were implemented.

3.2.1. Scanning mode

In scanning mode, sample temperature increases or decreases basically linear with time. For slow heating and cooling, the required heater power according to (2.3) is defined mostly by the heat losses ξ, which are in first approximation proportional to the overheating (T_s-T_0) of the central part of the membrane. To realize a temperature scan with linear heating/cooling one has to apply a power that in first approximation increases/decreases linearly with time. Power is proportional to square of the voltage; therefore, heater voltage should be proportional to square root of time. Here we assume that the heater resistance is constant during the measurement. In fact, it changes with sample temperature. The temperature dependence of the heater resistance was taken into account in the computer-controlled system, which is described in section 3.6.

A typical example of such measurement is shown in Figure 3.3.
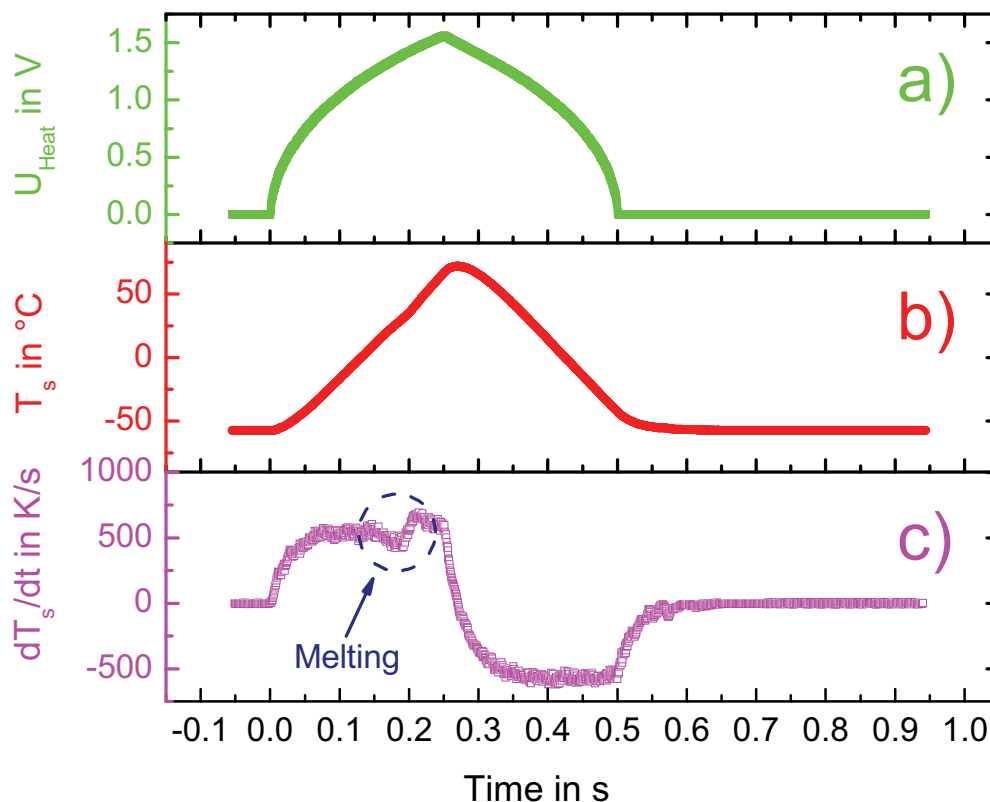
Figure 3.3: Measured data for a heating – cooling scan at 500 K/s: a) electrical voltage on the heater, b) sample temperature, c) heating rate. Sample: PCL ca. 100 ng, oven temperature -58 °C. Electronics according to Figure 3.11 (on page 26).

Heater voltage (Figure 3.3 (a)) is proportional to square root of time. Sample temperature (Figure 3.3 (b)) changes almost linear with time. In the heating rate curve (Figure 3.3 (c)), there is a good pronounced deviation from a straight line during melting of the sample (ca. 100 ng of polycaprolactone (PCL)). Such curves are hard to interpret. Therefore, common way of presentation of calorimetric scan measurement is in terms of heat capacity.

To calculate heat capacity using equation (2.3), one needs temperature, heater power and heat losses function ξ. Temperature and heater power can be directly measured during the experiment, but the heat losses function has to be determined. It depends on many factors, but for the change of heat losses during a single scan, the influence of the overheating (T_s-T_0) is dominating. Therefore, we will express heat losses as a function of overheating: $\xi = \xi(T_s$-$T_0)$. Here one important assumption is made: heat flow from the heater/sample to the surrounding is quasi steady, i.e. it depends only on the temperatures of the sample and the surrounding (oven), and thermal waves of

any kind can be neglected. It is worth to mention that function ξ changes significantly with changing the oven temperature T_0.

At the beginning, we have tried to define function ξ by isothermal calibration: choose several calibration points and then change the heater power from one point to another; wait long enough for the temperature to stabilize (0.1 s is sufficient for TCG 3880) and record values of power and temperature. In this experiment, $dT/dt = 0$ and the heat losses function is measured directly: according to the equation (2.3) $\xi = P_{heat}$. However, thermal conditions around the sample (temperature distribution in the surrounding gas and the membrane, may be also cold junction temperature) are different compared to scanning mode and this affects calibration. In fact, the difference in $\xi(T_s$-$T_0)$ between the static value and that at heating rate of 500 K/s is larger than the term $\left\{(C_s + C_{add}) \cdot \dfrac{dT}{dt}\right\}$ at such rate; this gives an error in the heat capacity of more than 100 %.

The solution is to calibrate at conditions close to the experimental ones. A symmetric heating–cooling scan (with the same absolute scanning rate) is performed. Figure 3.4 shows heater power as a function of temperature from such measurement with an indium sample. Two transitions are visible in this graph: melting at overheating (T_s-T_0) of about 60 K and crystallization at overheating of about 49 K.

As follows from the equation (2.3), heater power is

$$P = \xi + C \cdot \frac{dT}{dt} \tag{3.1}$$

Only the sign of the heat capacity term changes in (3.1) between heating and cooling (because of the sign of the heating rate), assuming that there are no transitions in the sample and its heat capacity depends only on temperature. In this case, the heat loss function is just the mean value of heater power on heating, *P_heat,* and that on cooling, *P_cool*: $\xi(T_s$-$T_0) = (P\_heat(T_s$-$T_0) + P\_cool(T_s$-$T_0))/2$. However, in case of some effect like melting or crystallization, the power deviates from the straight line as shown in Figure 3.4. Any effect in one curve will affect the mean function and this will reduce the effect as well as influence the result calculated from the other curve.

To increase the sensitivity to heat losses, one can do a calibration at reduced heating/cooling rate (say 10 K/s), so the last term in (3.1) reduces and *P_heat* is close to *P_cool*. However, different temperature distribution does not allow using such data.

Another idea is to take some smooth function and fit it to both measured curves (heating and cooling) simultaneously. A second or forth order polynomial was found to be suitable in most cases.

The last polynomial coefficient (constant) should be zero because heat losses are zero at zero overheating. Green curve in Figure 3.4 represents the heat losses function as quadratic fit.
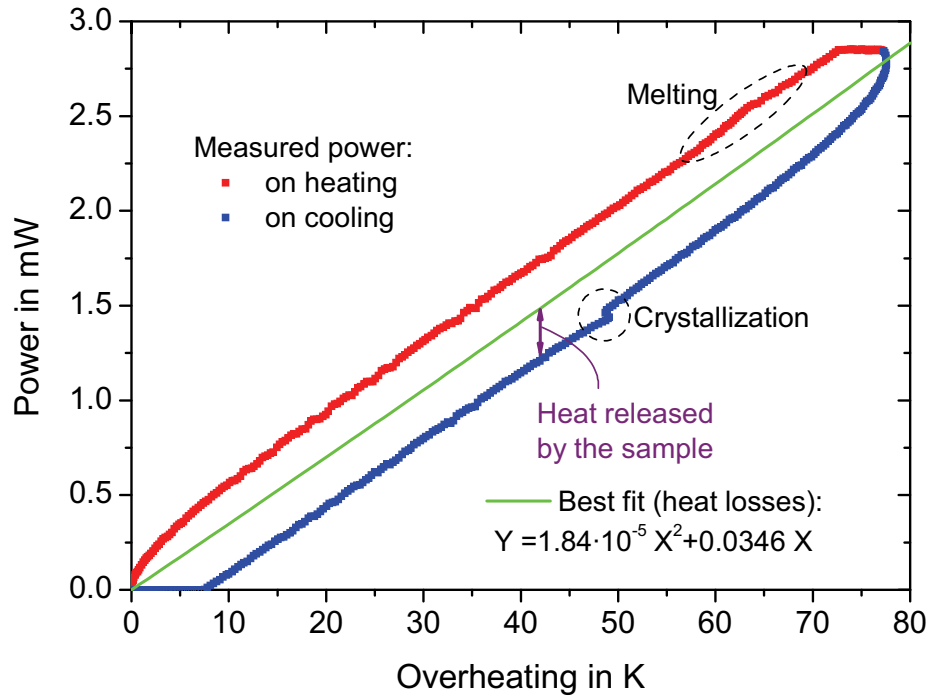
Figure 3.4: Symmetric heating-cooling scan at 500 K/s. Sample: Indium, oven temperature 98 °C. Red curve: power on heating, blue: power on cooling, green: heat losses function (quadratic fit).
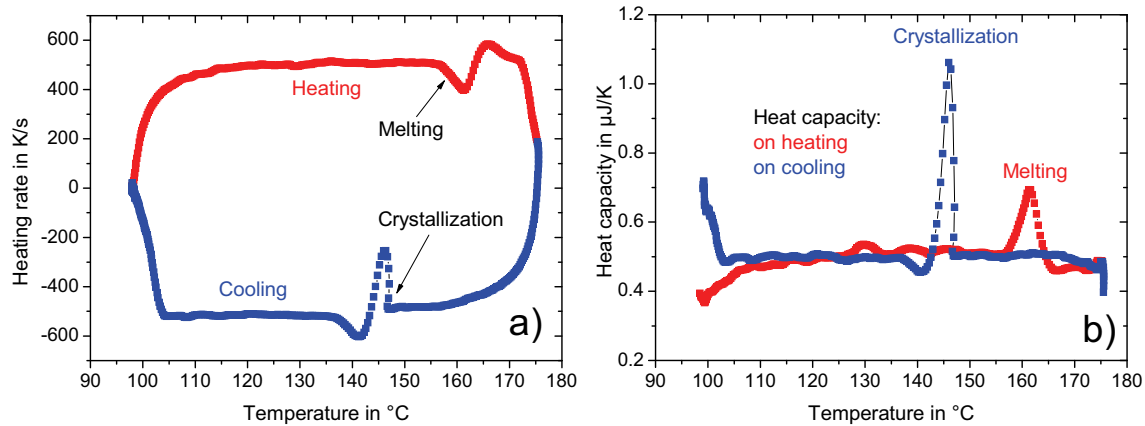
Figure 3.5: a) heating rate during melting and crystallization; b) calculated heat capacity. Sample: Indium; oven temperature 98 °C; assumed thermopile sensitivity 0.657 mV/K.

One of the best solutions is to perform the same temperature scan without the thermal effect in the sample and determine the heat losses function, which can be used for evaluation of the measurement of interest. For example to study isothermal crystallization kinetics of a relatively

slowly crystallizable material, the sample after the crystallization can be heated twice above the melting temperature. During the first heating, the sample melts and the melting transition is recorded. During the second heating and cooling, the sample remains amorphous because of the lack of time, so this scan can be used to determine the heat losses function $\xi(T)$.

For heat capacity calculation the derivative of temperature (i.e. heating rate) is used in Eq. (3.1); an example is shown in Figure 3.5 (a). The total heat capacity $(C(T) + C_{add}(T))$ is represented in Figure 3.5 (b).

Figure 3.5 (b) gives a good example of heat capacity measurement on cooling at 500 K/s; absolute value of heat capacity is in a good agreement with that on heating. Therefore, the technique can be used for heat capacity measurements on cooling at very high rates not available before.

To get sample heat capacity one can measure heat capacity $C_{add}(T)$ of an empty sensor under the same conditions (surrounding gas, oven temperature, heating rate) in advance and then subtract it from the measured total heat capacity with the sample.

3.2.2. Quasi-isothermal crystallization

In the previous section, it is shown how to measure heat capacity during fast heating or cooling. Alternatively, fast scanning possibilities can be used to prepare a sample with a certain thermal history and then processes like crystallization can be followed at nearly constant temperature with time resolution better than milliseconds.

Scanning mode is used to prepare a sample with the desired thermal history. Afterwards, heater power remains constant and sample temperature is recorded. After equilibration time, the temperature is almost constant; its deviation from the equilibrium value is a measure of the heat flow from the sample and hence the thermal processes inside the sample, as it is known for isoperibol calorimeters [29].

An example of a measurement on a polymer sample is shown in Figure 3.6. The sample is heated above melting temperature to melt it and to erase thermal history; then the sample is rapidly cooled down to the crystallization temperature (in this case it is oven temperature T_0). The sample does not crystallize on cooling, but afterwards during the isotherm. Crystallization is an exothermic process; the corresponding temperature increase is shown in the insert in Figure 3.6.

With a constant thermal link to the surrounding, sample overheating $(T_s\text{-}T_0)$ is to a first approximation proportional to power that is evolved in the sample. Integral of the power over time is energy; divided by the heat of fusion of the infinite crystal it is proportional to the change in crystallinity. The peak is relatively symmetric; areas under the curve to the left and to the right form

the maximum (areas *a* and *b* in the insert in Figure 3.6) are nearly equal. Consequently, crystallinity reaches in this moment about half of its end value.
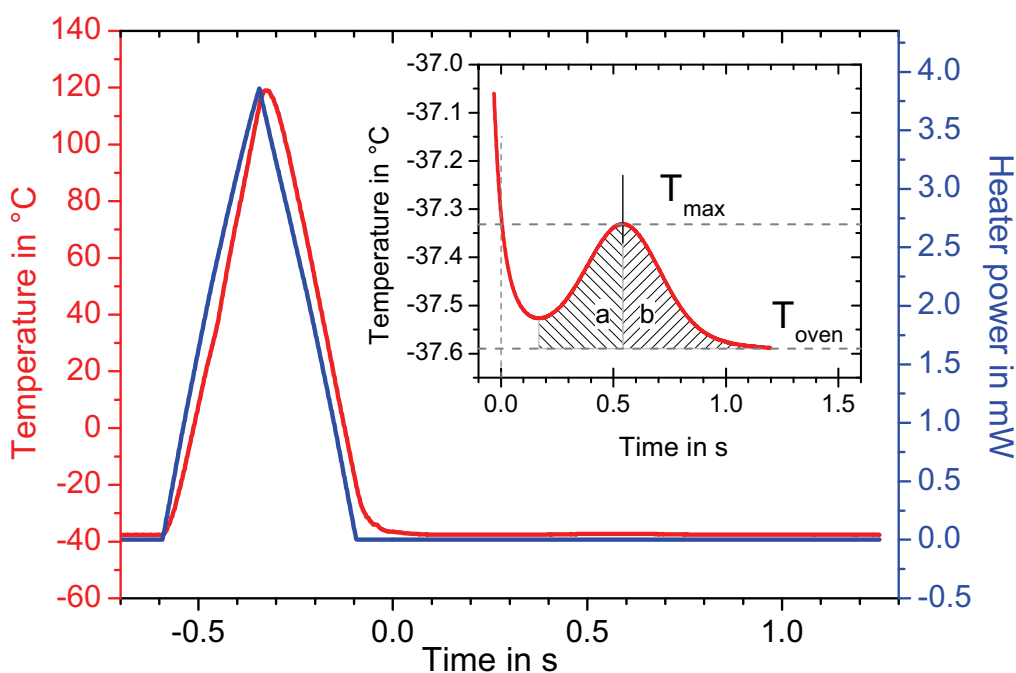

Figure 3.6: Isothermal crystallization experiment. Sample: poly(ε-caprolactone) (PCL); heating/cooling rate ca. 700 K/s; oven temperature $T_0 = -37.6$ °C; sensor: TCG3880. Insert: zoom in of the temperature signal with crystallization peak.

Therefore, the time from the start of crystallization to the maximum in the temperature signal is in good agreement with the crystallization halftime, so we will call it crystallization halftime ($t_{1/2}$). Its reciprocal value is a measure for the overall crystallization rate.

One should also mention some problems with determination of the crystallization temperature. In most cases, the final temperature can be used. However, when crystallization is very fast, significant part of the process can be completed before the sample reached the final temperature. For example, when polyethylene is crystallized at oven temperature of 106 °C (Figure 3.7), sample temperature remains about 1 K above the oven temperature during the main part of crystallization process. In this case, one should assign the resulting crystallization halftime to the sample temperature at that time and not to the asymptotic end temperature value.

Depending on the material and crystallization temperature, the crystallization peak looks different, so proper understanding of the curve is important.

During polyethylene crystallization at oven temperature of 102 °C, there is even no minimum and no maximum of the sample temperature during crystallization (Figure 3.7). The reason is that the crystallization peak is overlapped with the exponential temperature decay from the fast cooling.
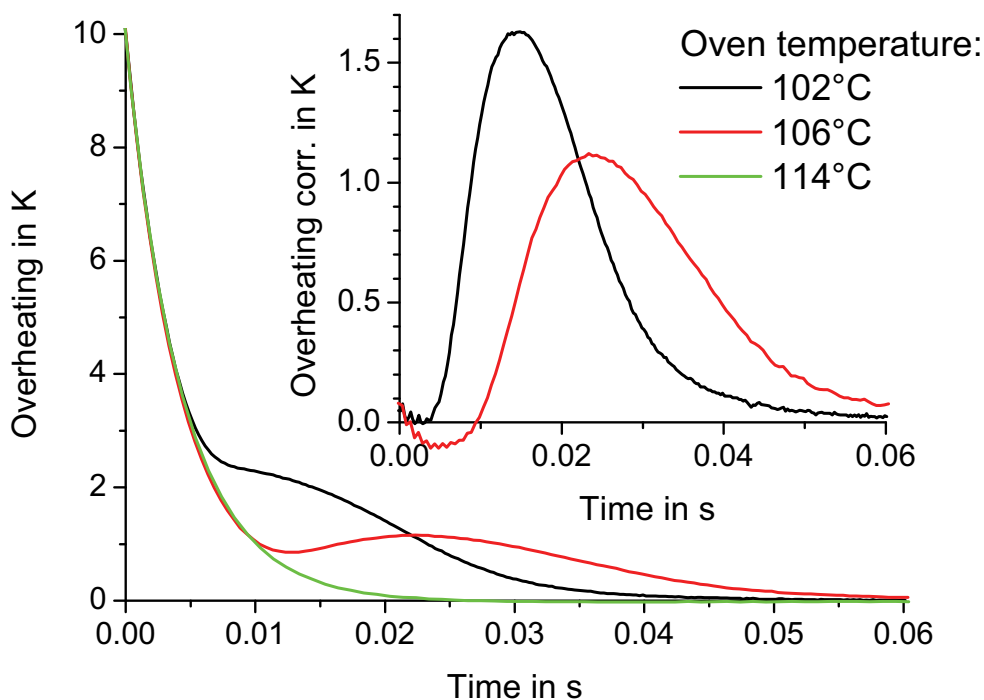
Figure 3.7: Crystallization curves for polyethylene (NBS SRM 1484) by rapid cooling from 170 °C. Sample mass about 100 ng. Insert: crystallization peaks at T_{oven} = 102 °C and 106 °C after subtraction of the curve at T_{oven} = 114 °C used as a "baseline". Time t = 0 is defined at ΔT = 10 K. Surrounding: helium at 5 kPa. Sensor: TCG3880; electronics according to Figure 3.11 (page 26)

To evaluate such measurements, one needs a "baseline" – similar cooling curve, but without the thermal effect in the sample. There are several possibilities to obtain such curve:

a) to measure the empty sensor (in advance or another sensor);

b) to measure another sample of similar heat capacity (in advance or on another sensor);

c) to measure the same sample at different condition (thermal history);

d) to measure the same sample at different temperature.

With an empty sensor (a), heat capacity is different from the sample measurement, which can lead to a difference in the cooling dynamics. To avoid this, one can use some "reference" sample with similar total heat capacity in the temperature range of the measurement (b). However, it is difficult to prepare a sample with desired mass.

Options with measurements in advance (a and b) imply that all crystallization temperatures are known from the beginning, which means that too many calibration measurements should be performed before the sample preparation if the sample is not studied jet. Another point is that

surrounding conditions, as gas pressure and composition, should be exactly reproduced; this created additional unnecessary difficulties.

If one uses another sensor as a reference (a and b), the difference between sensors can play an important role. The problem is known from differential scanning calorimeters (DSC), where selection of matching pairs of sensors for a differential system is an important stage of instrument production.

Special thermal history (c) can be the following. The quenching measurement starts from the temperature below the melting temperature of the sample (this works with many polymer samples). This temperature should be high enough, so that crystallization does not start during the short time (1-2 s) needed for temperature equilibration around the cell. For the "crystallization" measurement, sample should come to the start temperature from the temperature above the melting temperature, so that it is liquid. For the "base line" measurement, sample should be already crystallized, so that no measurable crystallization occurs during the "base line" measurement.

The last possibility (as listed above) is to use another temperature for the baseline measurement (d). In the example with polyethylene (Figure 3.7), one can take 114 °C to evaluate results at 102 and 106 °C. At 114 °C, the process is slow enough, so that one can say crystallization does not take place in the interesting time range. Measurements at 102 and 106 °C after subtraction of the measurement at 114 °C used as a baseline are shown in the insert in (Figure 3.7).

One can also combine methods: reduce the temperature and crystallize the sample before the "base line" cooling.

Another problem of measuring crystallization half time is determination of *time zero.* It can be defined in different ways:

a) *reaching of the oven temperature*;

b) *approaching the oven temperature with some precision ΔT (say 1 K)*;

c) *characteristic time of an exponential fit;*

d) *crossing the peak temperature T_{max} (see below);*

e) *temperature minimum before the crystallization peak*;

f) *start of the programmed isotherm.*

Reaching of the oven temperature (a) is the first what one thinks about, however this cannot be used since the oven temperature is reached asymptotically and it takes too long; in most cases it is not reached at all before the crystallization peak (see curves $T_{oven} = 102$ and 106 °C in Figure 3.7; Figure 3.8).

Approaching the oven temperature with some precision ΔT (b) can be a good option. However, it is sensitive to the choice of ΔT. For example, $\Delta T = 1$ K is acceptable for polyethylene at 106 and 114 °C (Figure 3.7), but at $T_{oven} = 102$ °C this condition is reached only after the peak, so at least $\Delta T = 3$ K is needed. Such a large threshold gives wrong results for higher oven temperatures (106 °C), because crystallization kinetics of polyethylene in this temperature region is strongly temperature dependent and 2 ms of cooling from 109 °C to 108 °C is not equivalent to the same time at 107 °C. On the other hand, this method can be used if the sample crystallizes slower and the lowest overheating before the crystallization peak is small (say less than 1 K). An example is shown in Figure 3.8; the starting time is labeled "$\Delta T = 1$ K".
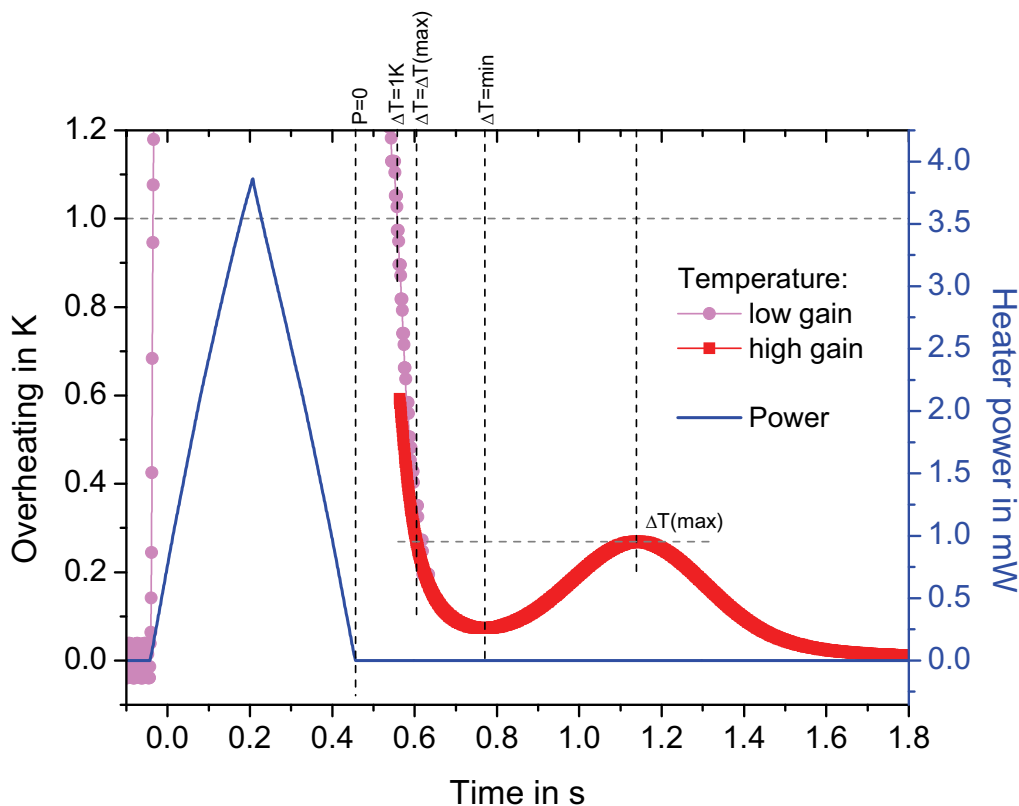
Figure 3.8: Definition of the crystallization time. Sample: ca. 100 ng Polycaprolactone. Sensor: TCG3880. $T_{oven} = -38$ °C. $T_{max} = 120$ °C. Electronics according to Figure 3.11 (page 26). Temperature signal recorded at two gain settings of the preamplifier.

The first part of the temperature curve can be fitted to "$\Delta T = T_0 \cdot exp(-(t-t_0)/\tau)$", then *time zero* can be chosen as the *characteristic time of the exponential fit t_0* (c), T_0 is a free parameter and it corresponds to the threshold ΔT defined in the previous method.

One can use the peak temperature T_{max} during crystallization as a temperature threshold and define *time zero* as time of *crossing the peak temperature T_{max}* (d); it is labeled "$\Delta T = \Delta T(max)$" in Figure 3.8. Such way defined starting time depends on temperature increase during crystallization,

but it should be kept not too high as long as we want to study isothermal kinetics and not too low to have enough sensitivity. Since this method uses parameters out of experiment, it is used in most of experiments presented in this work if not stated otherwise.

Temperature minimum before the peak (e) is shown in Figure 3.8 as "$\Delta T = \min$". Here also only experimental parameters are used; however, crystallization obviously starts before the minimum.

The latter two methods can be used even if there is no minimum before crystallization: one can subtract a baseline as described above and take time information from the curve after subtraction.

Start of the programmed isotherm (f). On one hand, this is may be the most "definite" choice; on the other hand, it gives the value of crystallization halftime that is set too high. This method gives better results with faster sensors as described in section 4.1 (page 63).

The absolute physical definition would exist if the temperature were immediately switched from the value in the melt to the crystallization temperature in the whole sample; the time of the switch would be $t = 0$. However, the possible cooling rate is limited, so one should choose some method of start time definition and pay attention when comparing different results. In this work, different methods were used for different sensors and samples; the method used is specified for each group of measurements.

3.2.3. Modulated mode

For relatively fast crystallization, the heat flow rate due to the enthalpy change is large and one can observe a crystallization peak in the temperature signal, like the one in Figure 3.6. At temperatures close to the glass transition, viscosity is high and this slows down crystallization process by orders of magnitude, so conventional DSC could be used to follow the isothermal process under such conditions. However, to reach this temperature from the molten state, the sample should pass the temperature region, where crystallization is fast. At moderate cooling rate, used in commercial calorimeters, a fast crystallizing sample stays long enough in this temperature region during cooling and crystallizes before the desirable crystallization temperature is reached. Therefore, one does need fast cooling capabilities of the calorimeter and thin sample in order to reach the crystallization temperature without crystallization on cooling.

When crystallization is slow, its heat production rate and corresponding temperature increase becomes too small to distinguish it from noise. However, AC-technique can be used to measure crystallinity as a function of time as described in section 2.1.2.

To use simplified equation (2.7), one should make sure that conditions (2.4) and (2.5) are met; otherwise, the absolute precision will not be high. If one is interested in the absolute value of heat capacity, some calibrations are already available. Thermal contact between the sample and the

membrane as well as thermal waves inside the sample are discussed by Merzlyakov [30]. Minakov at al. [31] have calculated temperature distribution around the sample and heated area. However, relative heat capacity changes can be detected with good resolution due to lock-in technique. To study crystallization kinetics, it is enough to measure relative changes of heat capacity and therefore we neglect all calibrations and corrections that should be otherwise applied for such sensor and use equation (2.7).

A small oscillating voltage is applied to the heater to generate an oscillating power of a few microwatts and the amplitude of the temperature oscillations on the second harmonic of the heater voltage is detected. Frequency range of optimum sensitivity is discussed in [32].
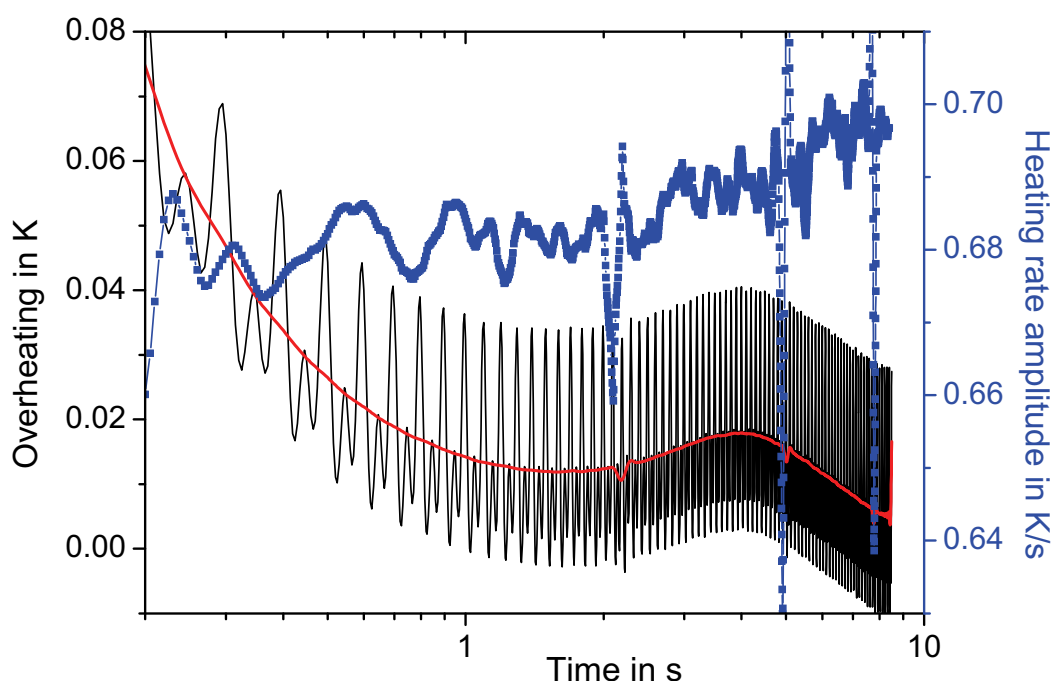
Figure 3.9: Temperature signal during quasi-isothermal crystallization after quenching the PCL sample from the melt – combination of DC and AC modes. Amplitude of temperature oscillations (blue line) contains information about heat capacity; change of the mean value reflects heat production due to crystallization. Oven temperature $T_0 = -54$ °C, 2f = 20 Hz.

Modulated mode can be combined also with other modes of operation. Thus, not only heat capacity but also enthalpy changes can be measured simultaneously. An example of such measurement is shown in Figure 3.9. After exponential decay, the temperature increases due to heat production by the crystallization process, a maximum is at about 4 s. When the sample crystallizes, its heat capacity decreases and the heating rate amplitude increases (blue curve in the Figure 3.9). The effect is more pronounced at higher frequencies; 20 Hz is shown here to demonstrate the raw signal. The non-sinusoidal shape of the signal (large amount of the first harmonic) is mostly due to diode effect on the connection junctions of the semiconductive heater.

Heat capacity is calculated then according to Equation (2.7). We are interested only in the time scale of the change in heat capacity, so it is taken in its scalar form including only modulus of amplitudes of temperature and heat flow neglecting the phase relation between them.

3.3. First experimental setup

3.3.1. Vacuum setup

For the measurements the sensor should be placed in a temperature controlled surrounding. Very low oven temperatures are needed for high cooling rates; high oven temperatures are needed for calibration and reducing temperature gradients (this will be discussed in section 3.3.3, "Sample preparation"). Surrounding gas should be controlled for several reasons. One should be able to remove oxygen to prevent sample oxidation at high temperatures. Additionally, as shown in [25], measurement conditions are strongly affected by heat capacity and thermal conductivity of the surrounding gas. Therefore, its pressure and composition should be controlled.
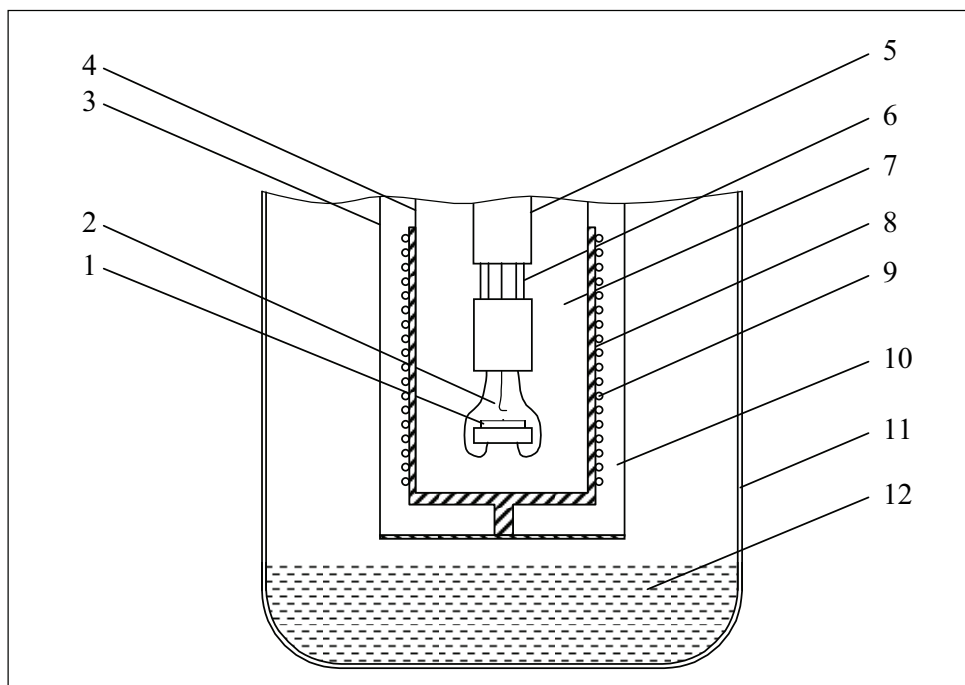
Figure 3.10: The oven of the calorimeter (not to scale). 1 – sensor, 2 –thermocouple to measure surrounding temperature, 3, 4, 5 – thin wall tube, 6 – connector, 7 – internal pressure controlled volume, 8 – copper oven, 9 – heater, 10 – external vacuum volume, 11 – Dewar vessel, 12 – liquid nitrogen.

Vacuum-tight volume is a good solution for this. As the sample holder is small, it was possible to put the whole system inside the vessel with liquid nitrogen for cooling, see Figure 3.10. To reduce heat losses from the oven and subsequently oven power and temperature gradients around the

sensor, there is an additional vacuum volume (pos. 10 in Figure 3.10) enclosed by a thin-wall tube (pos. 3). This vacuum isolation also saves liquid nitrogen. Tube (pos. 5) is used to hold the sensor (pos. 1). A thin wire Cu-Constantan thermocouple (pos 2) is used to measure the sensor temperature. It is located as close as possible to the sensor.

The thermal gradient across the tube from the measurement cell to the top part that is at room temperature could reach up to 200 K, so heat transfer along the tube had to be reduced. Seamless tubes were used to prevent increased heat transfer along the seam and asymmetric temperature distribution inside the tube. The tubes were made of stainless steel with wall thickness of 0.2 mm. Thermal isolation of the system from the surrounding is so good that it is enough to keep it in the Dewar vessel above the level of liquid nitrogen as shown in Figure 3.10 for sample temperatures down to -150 °C.

The internal volume can be filled with some gas (air, nitrogen or helium were used) at controlled pressure between 10 Pa and 100 kPa (0.1 mbar to 1 bar).

3.3.2. First electronics and experimental details

For the measurements the sensor is connected to the electronic setup shown in Figure 3.11 (see also [33]). All three modes of operation (section 3.2) were realized with this setup.
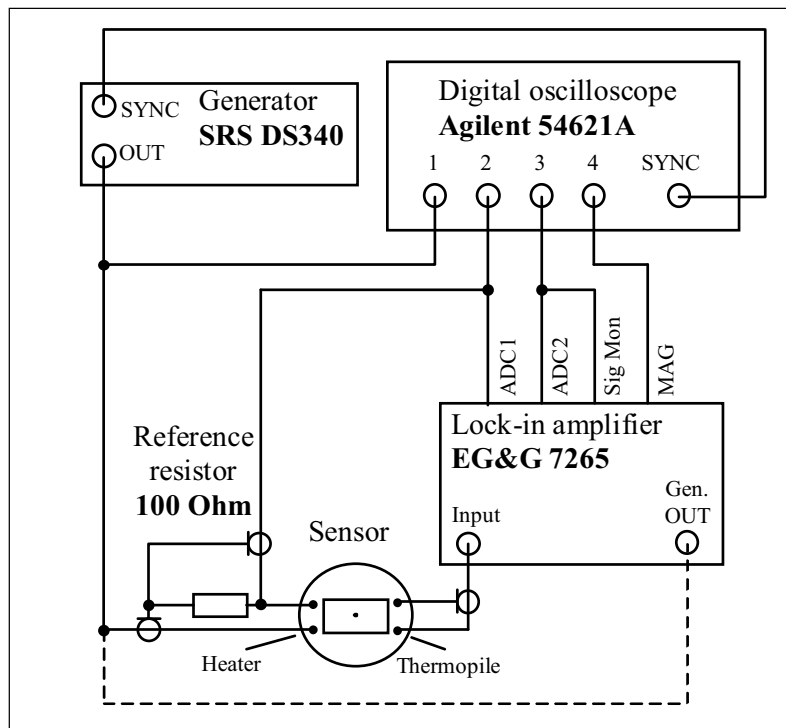
Figure 3.11: Scheme of the experiment. Grounding as well as temperature control and computer connections are not shown for simplicity.

To generate heater voltage a Stanford Research DS340 programmable arbitrary function generator was used. The output voltage as a function of time was calculated in advance by a computer and then downloaded into the DS340 via its computer interface. To measure the heater current a 100 Ohm reference resistor was connected in series with the heater (the heater resistance itself is about 600-700 Ohm depending on temperature).

At the beginning, a lock-in amplifier model 7265 from EG&G Instruments (now Signal Recovery, subdivision of AMETEK) was utilized to record the signal. The thermopile from the sensor was connected to the input of the lock-in amplifier.

In the lock-in amplifier, there is no way to read the voltage from the main analog-to-digital converter (ADC) directly; so a general purpose ADC of the device (with an effective resolution of 13 bits) was used to get the temperature signal. The "Signal monitor" output of the lock-in amplifier was connected to ADC2 (see Figure 3.11). Actual gain of the preamplifier (from the "Input" to the "Signal Monitor") was calibrated for each gain setting. Another ADC (ADC1) was used to measure the current through the heater. Readouts of both ADCs were stored in the internal buffer memory of the lock-in amplifier in burst mode with a sampling interval between 500 µs and 5 ms and read out by the computer after the measurement.

This way, two signals are available out of the experiment – heater current and thermopile voltage as a function of time. Knowing the generator voltage (it can be also measured in a separate run) one can calculate the heater power. As for the temperature, the sensitivity of the thermocouple was not known initially. We have started with a manufacturer's value of 3 mV/K and then changed it to less than 1 mV/K according to the melting temperature of indium. More precise temperature calibration is described in section 3.5 (page 37).

In AC-mode, the internal generator of the lock-in amplifier instead of the DS340 was used to apply small periodic power oscillations (dashed line in Figure 3.11). The lock-in amplifier measured the amplitude of the temperature oscillations at the 2nd harmonic. Typical heater voltage amplitude was 30 mV, corresponding to power amplitude of about 1 µW. The voltage at the thermopile was about 30 µV, corresponding to temperature amplitude of about 30 mK at a thermal frequency of 6 Hz (generator frequency 3 Hz).

To perform "scan" and "oscillating" measurements simultaneously the generator output of the lock-in amplifier was connected in parallel to the DS340 output. The 50-Ohm internal output resistance of each generator resolves the problem of electrical connection of the two outputs. Note that the output resistance of each generator acts as an additional 50-Ohm load in parallel with the system (heater + reference resistor) for the other output, so generator output voltage should be adjusted for this.

Next, a digital oscilloscope 54621A from Agilent Technologies was used for data acquisition instead. This digital oscilloscope records the input data continuously and not only after the synchronization impulse. Therefore it was possible to record the whole signal completely also before the sync. This gave a stable time reference to the start of the heating and has opened a possibility to use the "averaging" function of the scope to average the signal over several measurements and to improve the signal to noise ratio. Actually, the oscilloscope has only two inputs, so only two of the four signals (normally 2 and 3) were connected during a single measurement.

Continuously repeating heating/cooling cycles were performed with a cycle time of 2 to 100 seconds; the results were mostly averaged over 4 to 16 scans (maximum 128). Because of the limited resolution of the oscilloscope (12 bit effective, even after averaging) large temperature scans (for melting) and small temperature changes (during crystallization) were recorded separately with different settings of sensitivity.

The oscilloscope was used for AC measurements as well. The AC voltage (e.g. at 3 Hz) from the internal generator of the lock-in was applied to the heater and the lock-in amplifier has measured the thermopile signal at the second harmonic. The lock-in was programmed such way that the magnitude (MAG) appears at one of the analog outputs which was connected to the oscilloscope (shown as "input 4" in Figure 3.11) for averaging over several scans.

The oven temperature was controlled by a Eurotherm 818S controller. Temperature near the sensor was measured by a type K thermocouple, the reference point was electronically stabilized at 50 °C and the voltage was measured by a Prema 6001 digital multimeter.

3.3.3. Sample preparation

The sample should be placed on the center of the membrane, between the heater stripes (Figure 3.12), where the temperature is more or less homogenous (see also Figure 3.27 on page 47 for temperature distribution in the membrane). An optimal sample size is in the range of $40*40*40 \ \mu m^3$; this corresponds to a volume of $64*10^{-9} \ cm^3$. Common polymers have a density of about 1.5 g/cm^3, so the mass of such sample is about 100 ng. Smaller samples with lower thickness can be used for high scanning rates. The absolute mass of the sample was not measured because of sample handling problems with such small samples.

A piece of material is cut under the microscope using two scalpels. Even hard polymers feel very soft on such scales because one can apply huge pressure with relatively small force. Then the sample should be put onto the membrane. The problem is that the membrane breaks immediately as soon as one touches it with almost any tool. A 0.07 mm thin copper wire was found to be

nondestructive for the membrane. The sample is taken by the wire and placed on the membrane in the heater center. For such a small sample, an electrical force caused by stationary electrical charges on the surface is much stronger than gravitation force; the sample normally sticks to the membrane. This effect is much more pronounced in winter, when the humidity is low; polymer samples start to jump on the membrane from time to time; sometimes they even jump away. In such cases, one has to increase humidity in the room at least locally to prepare a sample.
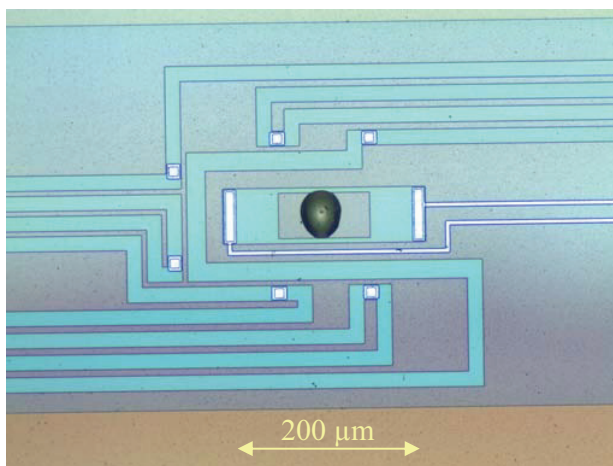

Figure 3.12: Membrane with a sample. Sensor: TCG3880, sample: sPS.

Then the cell is connected to the calorimeter hardware and the sample is heated once above its melting temperature (or glass transition temperature for amorphous samples) at a moderate heating rate; 200 K/s was used in most experiments described in this work. During the first melting (softening), the internal stresses of the sample are released and the sample normally changes its shape as well as the position on the membrane. Therefore, it should be mechanically moved back to the heater center and heated again. After this procedure is done several times, the sample finds its place and the sensor can be placed into the vacuum system for the measurements.

Some metal samples were measured for calibration. To produce good thermal contact, a tiny amount of Apiezon® N cryogenic vacuum grease was used. This helped also to remove the sample afterwards and to use the same sensor for several samples. Actually, this grease is specified to use only up to +30 °C, but at such amount and being heated for such short time, it did not cause any problems. On the other hand, it worked well down to -170 °C.

In some cases, if sample viscosity in the molten state is very low, the sample does not remain on the heater. For example, a small droplet with diameter of about 25 µm of n-alkane $C_{122}H_{246}$ in the middle of the membrane is shown in Figure 3.13 (a). After six times heating from 30 °C to 150 °C, the sample moved to the side (Figure 3.13 (b)). After following heating cycles from the oven temperature of 30 °C to 150 °C, the sample moved out of the heater area (Figure 3.13 (c)).
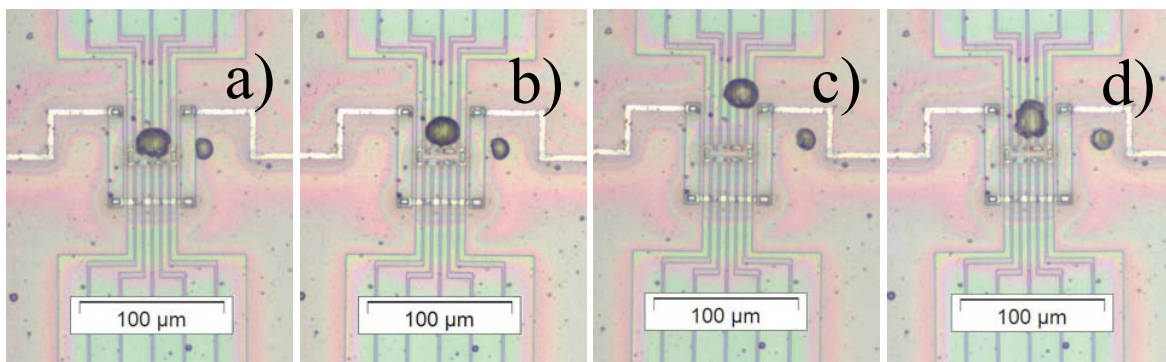
Figure 3.13: $C_{122}H_{246}$ sample: a) after first melting; b) after six times heating from 30 °C to 150 °C; c) after many heating/cooling cycles between 30 °C and 150 °C; d) after crystallization at oven temperature from 100 °C to 117 °C, heating up to 140 °C. Sensor: XI240.

Next, crystallization experiments at oven temperature between 100 °C and 116 °C were performed; the amplitude of temperature change for melting of the sample was smaller (highest temperature 150 °C). During these experiments, the sample moved back towards the center of the sensor (Figure 3.13 (d)). This shows that for samples with very low viscosity in the melt, one should try to reduce temperature amplitude and set the oven temperature as high as possible to keep the sample on the active area.
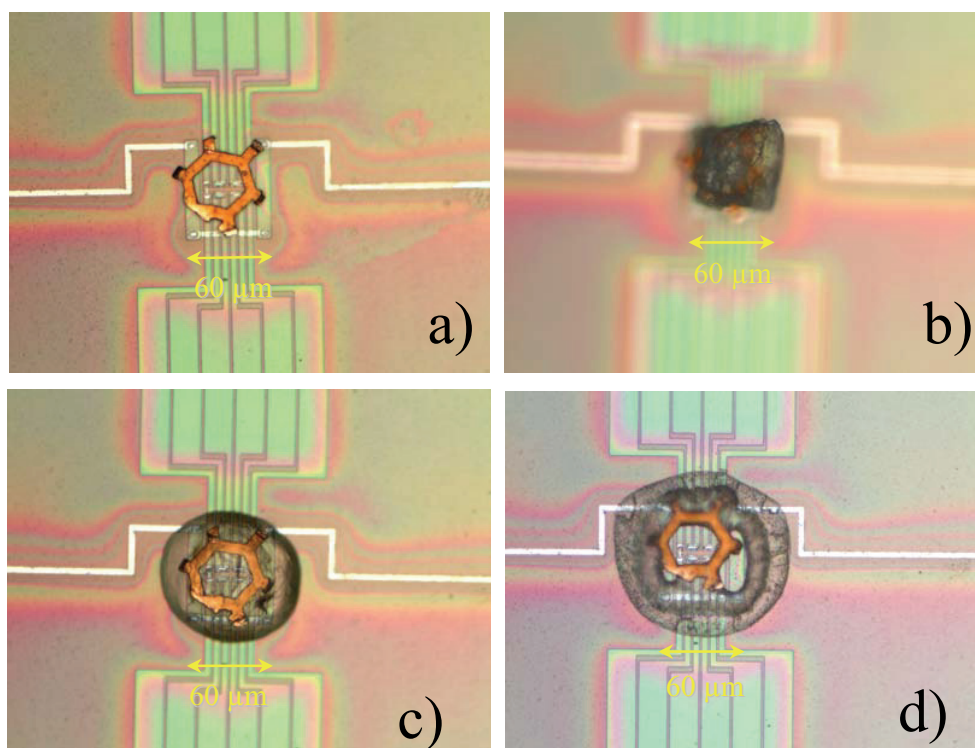
Figure 3.14: a) copper cell on the membrane XI240; $C_{32}H_{66}$ sample: b) before the first melting; c) after the first melting; d) after many measurements.

Even shorter chain n-alkane, dotriacontane ($C_{32}H_{66}$) was spread in form of little droplets around the heater and all over the membrane after several heating cycles. In such cases, one can use some cuvette to keep the sample. A single cell was cut out of a copper net originally made for electron microscopy and put on the membrane (Figure 3.14 (a)). Then the sample was put on top of the ring (Figure 3.14 (b)). After the first heating above the melting temperature, the sample was covering the copper ring; see Figure 3.14 (c).

With this sample, the two peaks with less than 5 K in between could be well resolved up to high heating rates; details are presented later in this work (section 3.9).

3.4. First measurements

The first test sample was poly(ε-caprolactone) (PCL) obtained from Sigma-Aldrich (Prod. No. 81277). After melting several times on the membrane the sample was a droplet of 60…80 μm diameter. Sample mass was ca. 100 ng. PCL was measured in air at pressure of ca. 5 kPa.

Selected curves at different cooling rates are shown in Figure 3.15 (a). There is a crystallization peak at cooling rates of 50 and 100 K/s. At a cooling rate of 250 K/s, the crystallization peak disappears; the sample remains amorphous and it shows only a glass transition. If the amorphous sample (after cooling to -190 °C at 1000 K/s) is heated at a rate of 500 K/s (Figure 3.15 b), there is a "cold crystallization" peak (crystallization above the glass transition on heating) and then melting. This effect decreases upon increasing the heating rate. At 2500 K/s, the sample remains amorphous also on heating (Figure 3.15 b).
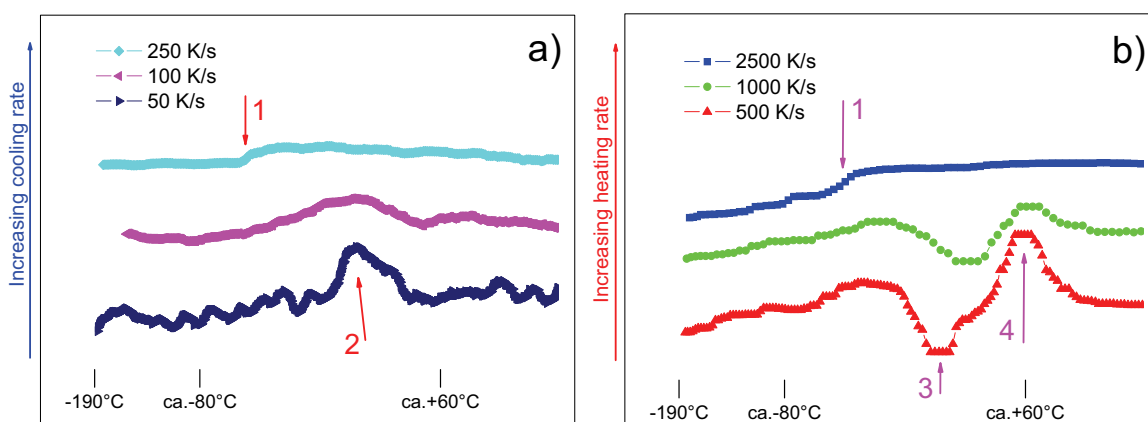
Figure 3.15: PCL heat capacity: a) cooling; b) heating from amorphous state. 1 – glass transition; 2 – crystallization "from hot"; 3 – crystallization "from cold"; 4 – melting. Sensor: TCG3880; oven temperature: -190 °C.

This experiment shows that the technique is suitable for fast calorimetric measurements. To our knowledge, this was the first heat capacity measurement on cooling at such high cooling rates.

Relatively fast crystallizable polymer (PCL) was obtained in amorphous state directly in the calorimeter. For PCL it was found that the scanning rate needed to prevent crystallization on heating (2500 K/s) is about ten times higher than the rate needed to prevent crystallization on cooling (250 K/s). A similar ratio of about 10 was observed later for other polymers.

Temperature calibration of the thermopile was an open question (it is discussed in more detail in section 3.5), so the temperature was not known exactly when the heater on the membrane was active. However, oven temperature was measured independently with good precision, so sample temperature was known when thermopile voltage was close to zero. At the oven temperature, isothermal crystallization kinetics could be studied. For temperature dependence study, measurements were performed at different oven temperatures. We were interested in crystallization halftime as a function of temperature during isothermal crystallization. It is known, that PCL crystallizes reasonably fast at 20 °C. Therefore, the oven temperature was set to 20 °C at the beginning and heat/cool cycles with increasing amplitude of heater voltage were applied until melting peak like the one in Figure 3.3 (on page 15) was observed. Crystallization peak was not visible on that setting of the amplifier gain; therefore, the sample was left for some time at the oven temperature to crystallize between the pulses. Thermopile sensitivity was estimated in the first approximation from the thermopile voltage in the melting peak. With increased amplifier gain, the crystallization peak after the heating pulse became visible. Then the oven temperature was decreased by 10 K and the heater voltage adjusted to observe the melting peak. The crystallization peak could be recorded with increased amplifier gain.

Such studies were carried out before for example on poly(ethylene terephthalate) (PET) [34-36] and syndiotactic polystyrene (sPS) [5], where only the "slow" ends of the curve were measured. For these materials, both sides of the curve can be studied using common DSC; in other cases only the high-temperature end of the curve could be obtained [37-39]. We have chosen PCL and PE, a fast and a very fast crystallizing polymer, to check the limits of the new calorimeter for isothermal measurements.

3.4.1. PCL: Quasi-isothermal crystallization

Selected crystallization curves of PCL at different oven temperatures are shown in Figure 3.16. At these temperatures, crystallization is relatively fast and heat production rate is high enough to give a good signal. At temperatures where the crystallization is slower, the peak becomes broader. The area under the peak corresponds to the total melting enthalpy, so with broadening the peak its height decreases.
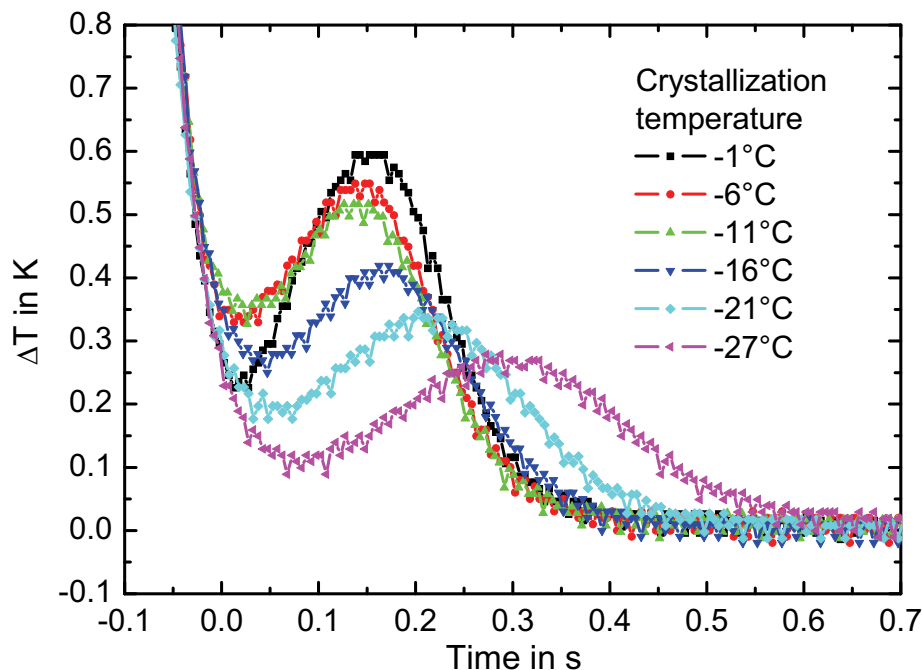
Figure 3.16: Isothermal crystallization of PCL at different oven temperatures after heating/cooling at 500 K/s. Sample mass ca. 100 ng. Sensor TCG3880; air pressure 30 Pa.

At crystallization half times longer than about ten seconds, the signal from the crystallization process falls below the noise level and cannot be measured by the temperature increase. Nevertheless, such slow crystallization process can be followed by heat capacity measurements (AC calorimetry) as described in section 3.2.3 (page 23).

3.4.2. PCL: AC measurements

A relatively high oscillating frequency ($2F = 140$ Hz) was chosen to get better resolution in time and to follow crystallization almost from the very beginning.

The crystallization half time by heat capacity change $t_{0.5\ \Delta Cp}$ is defined as a time when the heat capacity crosses the middle value between the heat capacity in the molten state and that in the crystalline state. Blue curve in Figure 3.17 shows heat capacity at oven temperature of -54 °C. The value was reduced so that at the beginning, when the sample is still amorphous, it corresponds to the heat capacity of amorphous PCL from the ATHAS databank [40] at this temperature.

At the beginning, the sample is liquid, so heat capacity equals to that of liquid phase and is constant. As for value "after crystallization", it is already known that after the main crystallization is finished there is a long process of reorganization which takes orders of magnitude more time than the primary crystallization [41]. However, we are interested in the primary crystallization, so some asymptotic slope shown in the Figure 3.17 by a dash line was taken as an "end value". An average

line between the two limits was taken as a half-crystallinity value (dash line in Figure 3.17); time when this line is crossed is defined as a "heat capacity crystallization half time" $t_{0.5\Delta Cp}$. Figure 3.17 shows a measurement where both crystallization halftimes can be determined simultaneously.
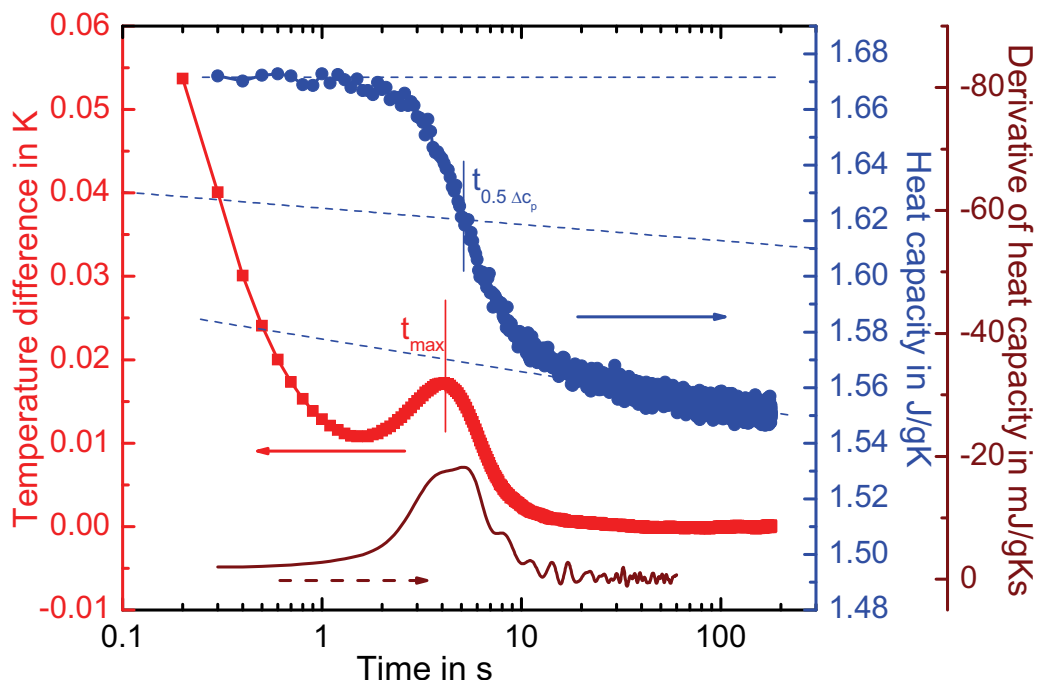

Figure 3.17: Different modes of PCL crystallization kinetics measurement. Sensor: TCG3880. Heat capacity evolution and enthalpy change were measured simultaneously at oven temperature of –54 °C. Heat frequency 2F=140Hz. The curves represent the average over 128 measurements utilizing the oscilloscope. Derivative of the heat capacity is shown with reverse axis direction for better comparison with temperature signal.

As one can see from Figure 3.17 the time t_{max} of maximum of temperature, or heat production ("Enthalpy mode") and time $t_{0.5\,\Delta Cp}$ defined by the half value of heat capacity change ("Heat capacity mode") do not coincide exactly. May be it is because of a separate reorganization process after the main crystallization which makes the end value of heat capacity lower than at the end of main crystallization and this shifts the result a bit. On the other hand, the heat capacity curve may be simply not symmetric in sense that maximum slope which corresponds to the maximum of crystallization rate and thus maximum in the temperature is not in the middle of the main crystallization process. The first derivative of heat capacity is shown in Figure 3.17 below the temperature signal. Despite of oscillation-type noise, one can say that rate of decrease of heat capacity coincides with the temperature increase due to heat production.

Anyway, this difference between $t_{0.5\,\Delta Cp}$ and t_{max} appears to be not serious if one compares the results. They are combined in Figure 3.18. On the low temperature side there is no significant difference between the results from "enthalpy mode" and from "heat capacity mode".

On the high temperature side, classical DSC devices were used to continue the curve. "Pyris 1" from Perkin Elmer with a sample mass of 11.6 mg was used for intermediate times and a "Setaram 121" with a sample of 274 mg for long measurements with crystallization halftimes up to 3 days.
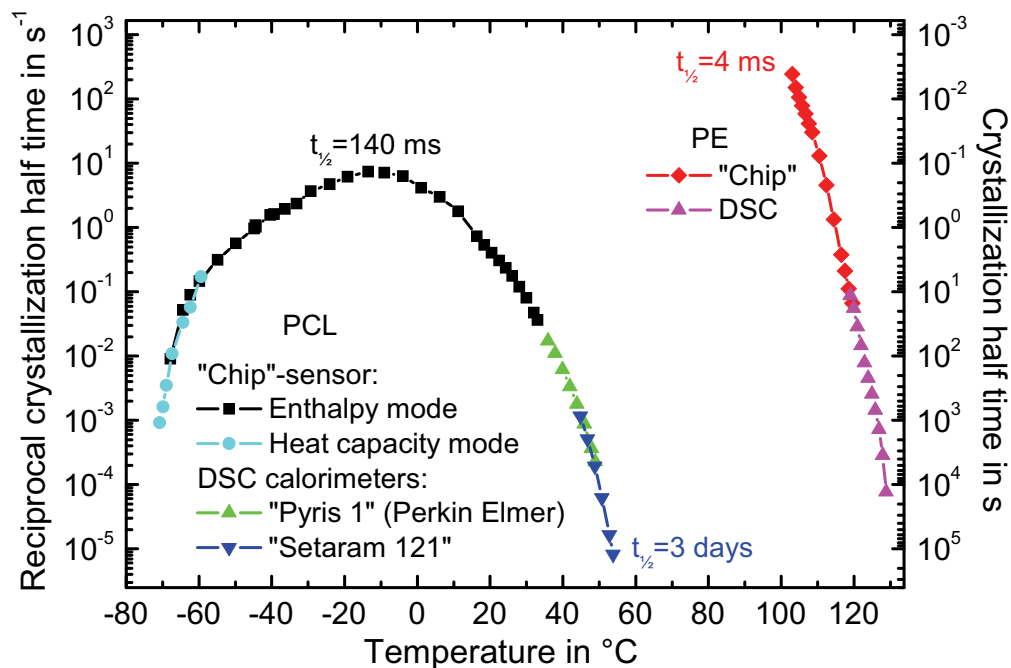

Figure 3.18: Poly(ε-caprolactone) (PCL) and polyethylene (PE) isothermal crystallization rate (in terms of reciprocal crystallization halftime). Sensor: TCG3880; electronics according to Figure 3.11 (page 26); sample mass about 100 ng; crystallization at oven temperature. PCL was measured in air at reduced pressure of ca. 5 kPa. PE was measure in helium at similar pressure.

The crystallization half time of PCL shows typical bell-shaped temperature dependence (Figure 3.18) with a maximum of crystallization rate at about -10 °C. The whole curve looks symmetric, however there is a small shoulder on the low-temperature side at about -40 °C, which is not present in the high-temperature part of the curve. Actually there is no reason for the curve to be symmetric because the overall crystallization rate is controlled by at least two different processes – nucleation and crystal growth rate; each of them has its own temperature dependence [36, 42]. At temperatures close to the glass transition, temperature mobility decreases dramatically so crystal growth rate becomes very low and crystallization rate decreases by orders of magnitude (Figure 3.18). On the other side of the curve, close to the equilibrium melting temperature, nucleation becomes a limiting factor; crystallization rate also decreases. At about -10 °C there is an optimum combination, so the overall process is the fastest. Similar dependence was seen for example on poly(ethylene terephthalate) [43] by measuring crystallinity via optical density. Cobbs and Burton have observed crystallization halftimes down to 40 s; with our device, much faster processes could be studied.

3.4.3. Limits of the sensor time resolution: polyethylene

The shortest time measured for PCL is 140 ms; as one can see in Figure 3.16 on page 33, the time resolution of the sensor is much better. A very fast crystallizing material was needed to check the limits of the system.
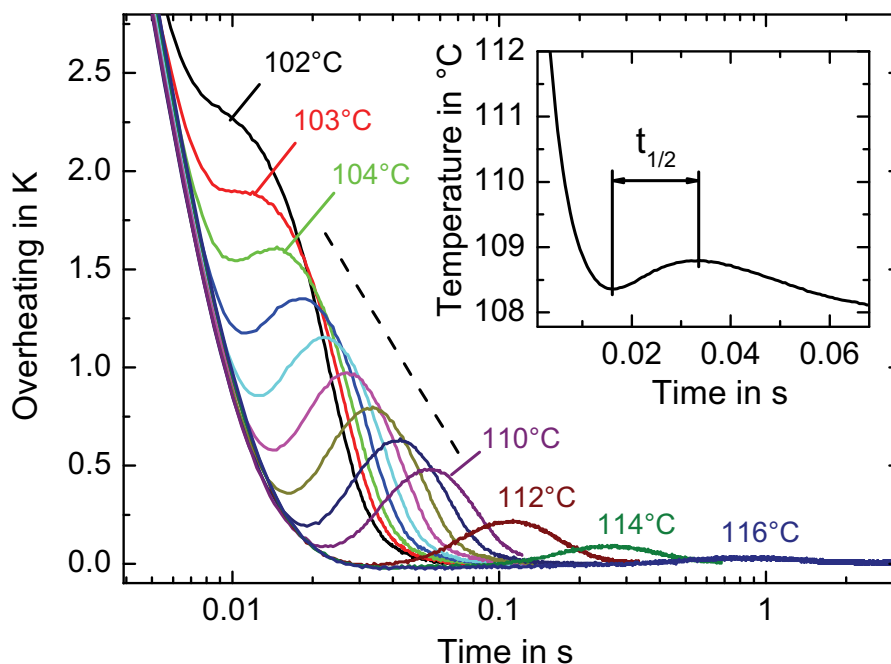
Figure 3.19: Crystallization curves for polyethylene (NBS SRM 1484). Sensor: TCG3880. Indicated temperatures are oven temperatures. Measurement in Helium at 5 kPa. Sample was heated to 170 °C with 250 K/s; then the heater was switched off; highest cooling rate was 14 000 K/s. Insert: definition of "crystallization halftime".

Such material is linear polyethylene (PE) (Standard Reference Material SRM 1484 from National Bureau of Standards) with molar mass of about 100 000 g/mol and ratio M_w/M_n mass- to number-average molar mass of the order of 1.2. Characterization of this material is given in [44]. The sample was prepared in the same way and had similar size as PCL. Because PE crystallizes very fast, helium surrounding at reduced pressure (5 kPa) was used to increase the cooling rate and to prevent crystallization during cooling as much as possible.

This sample crystallizes much faster; even at the highest cooling rate, it was impossible to obtain an amorphous sample below 110 °C. Measured temperature traces are shown on Figure 3.19.

One can see that at temperatures below 110 °C crystallization starts already at cooling. Therefore, the lowest value of temperature before the crystallization peak (and not the oven temperature) was assumed "crystallization temperature". Next, time of that temperature minimum was assumed the "start time". Definition of "crystallization halftime", $t_{1/2}$, is shown on the insert in

Figure 3.19. For low temperatures, where the temperature even did not reach a minimum (oven temperature 103 °C) we did not define a "crystallization halftime". Nevertheless, time resolution of the thin film calorimeter is below 10 ms.

3.5. Temperature calibration

In the measurements shown above, the temperature scale was based on the melting temperature of the material and scaled linearly with the thermopile voltage. It was enough to check the technique on some known samples; the exact value of melting temperature was not needed.

Therefore, when it was proved, that the technique works, the task came up to calibrate the temperature signal.

The best calibration is on the measured effect. Therefore, we have used melting points of several reference metals. However, for a good calibration one needs enough points that would mean one needs many calibration substances and many sensors since one cannot remove the sample easily. This can produce additional problems if the sensors for any reason are not identical. The alternative solution to get more points is to use a few samples and measure the melting points at different oven temperatures. Three metals (indium, tin end lead) were used.

### 3.5.1. Heater resistance as a thermometer

The best thermometer would be the heater itself. Its resistance changes with the temperature, so it could be used as a thermometer, as some other groups do. L. Allen and coworkers [45] for example use an extremely stable current source for the heater to obtain sufficient signal-to-noise ratio for heater resistance measurement. The disadvantage of this construction is that the heater current cannot be controlled according to a given temperature program; measurements on cooling are not possible. Therefore, we have used the thermopile for temperature measurement.

In our case, the signal of the heater resistance was too noisy to use it for calculation of heat capacity. However, information about heater resistance could be used to calibrate the thermocouple.

First, heater resistance itself should be calibrated. For this, one has to know heater resistance and temperature simultaneously. Heater temperature is known when no current flows through the heater: in this case, the heater has the oven temperature. However, to measure the resistance one has to feed some current through the heater; corresponding Joule heating will increase heater temperature and distort the result. The workaround is to measure the heater resistance as a function of heater power and then extrapolate it to zero power (Figure 3.20 (a)). Corresponding extrapolated values for different oven temperatures are represented by squares and black curve in Figure 3.21.
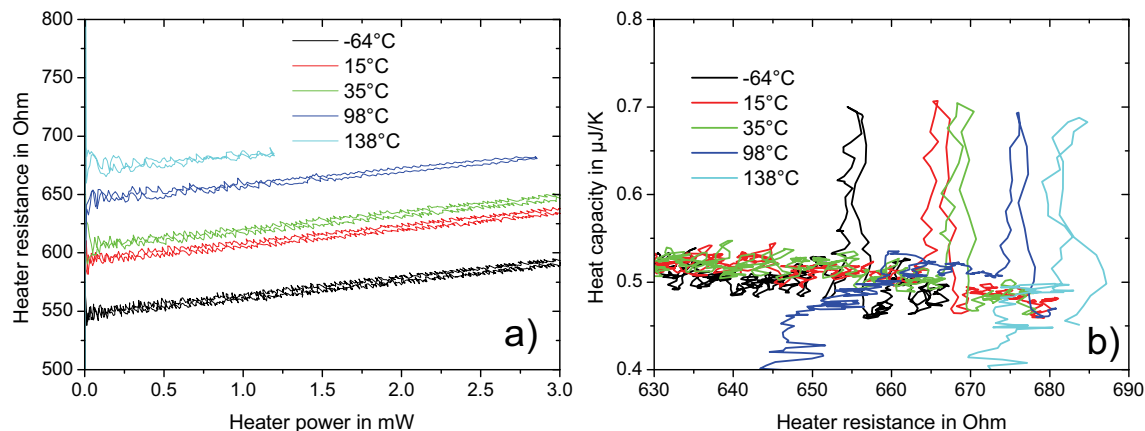
Figure 3.20: Calibration of the thermopile through the heater resistance: a) heater resistance versus power (heating/cooling scan at 500 K/s); b) indium melting peak (heater resistance is used as a measure of temperature). Sensor: TCG3880; oven temperatures are indicated in the legend.
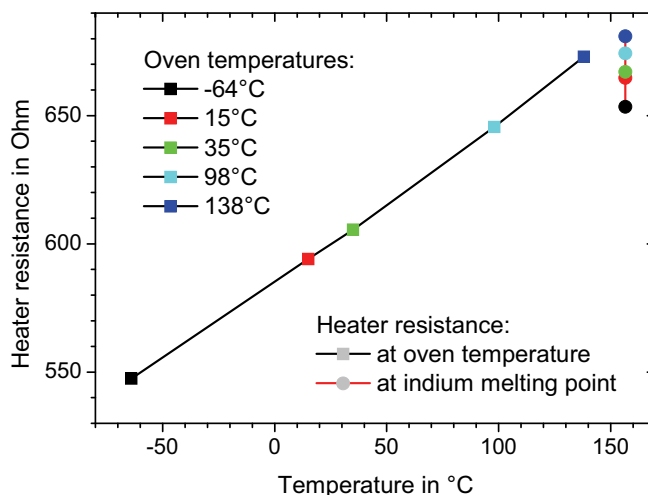
Figure 3.21: Heater resistance versus sample temperature at different oven temperatures. Two points are known for each oven temperature: the oven temperature itself and the melting temperature of a reference material (indium). Black curve represents heater resistance at the oven temperature and red curve – at indium melting temperature. Sensor: TCG3880.

The dependence is almost linear. However, there is another known point for each measurement – melting point of indium (the sample was on the sensor in previous experiment). Heater resistance at the melting temperature of indium can be obtained from the melting peak onset in Figure 3.20 (b), where heat capacity is plotted against heater resistance. One can see that melting temperature of indium corresponds to different values of heater resistance at different oven temperatures. To evaluate the absolute temperature error due to this effect, we have plotted these results in Figure 3.21 (circles with red curve) together with calibration points at oven temperature.

At oven temperature of -64 °C and T_s = 156.6 °C (melting of Indium), heater resistance was 653.4 Ohm. On the calibration curve from resistance measured at oven temperature, this resistance value corresponds to temperature 109.6 °C. This gives an error of about 50 K.

The problem is most probably that the resistance of connecting wires (especially those on the membrane) is also temperature dependent and this adds a significant contribution to the total measured heater resistance. So, heater resistance of the gauge TCG 3880 cannot be used to determine absolute temperature. One possible solution would be a four-wire connection for heater resistance measurement. Still one would need thermocouple because of noise of the resistance signal. Another problem, which was not carefully studied, is aging of resistance. Any case, sensors with four-wire connection were not available at that time, so we went another way and did absolute calibration of the thermopile.

3.5.2. Calibration data

As heater resistance did not work, I had to calibrate the thermopile voltage using melting points of metals.

The "classical" thermopile calibration presumes that the "reference" junction is always at the same temperature (for example ice-water mixture) and only the "sample" temperature is changed. This way, calibration function is a function of only one variable.

Many different calibration standards are needed for nonlinear temperature-voltage dependence. In my case, this implies usage of different sensors because the sensor is often destroyed if one tries to remove the sample. Difference between the sensors used for calibration as well as difference in the sample position will introduce systematic slope error into all measurements. Another point is that the oven temperature has to be changed in small steps; this is especially needed for sample mechanical stability, see section 3.3.3. That is why the following procedure was used.

Only a few calibration substances (indium, tin and lead) were used. Instead of replacing samples and so changing "sample temperature", I have changed "oven temperature" (at constant "sample temperature" – melting point of metal) to get more calibration points. Afterwards, the calibration function was used to recalculate thermopile voltage into "sample temperature" at constant "oven temperature". Therefore, I call it "reverse calibration".

Thermopile voltage corresponding to melting point of indium, tin and lead was defined at different oven temperatures. Melting point was defined as an onset of melting on heating in the graph of heat capacity versus temperature according to GEFTA recommendation [46]. Typical measurement is shown in Figure 3.22 (a). Thermopile voltage was used on the temperature axis; this way voltage corresponding to the sample melting point was obtained.
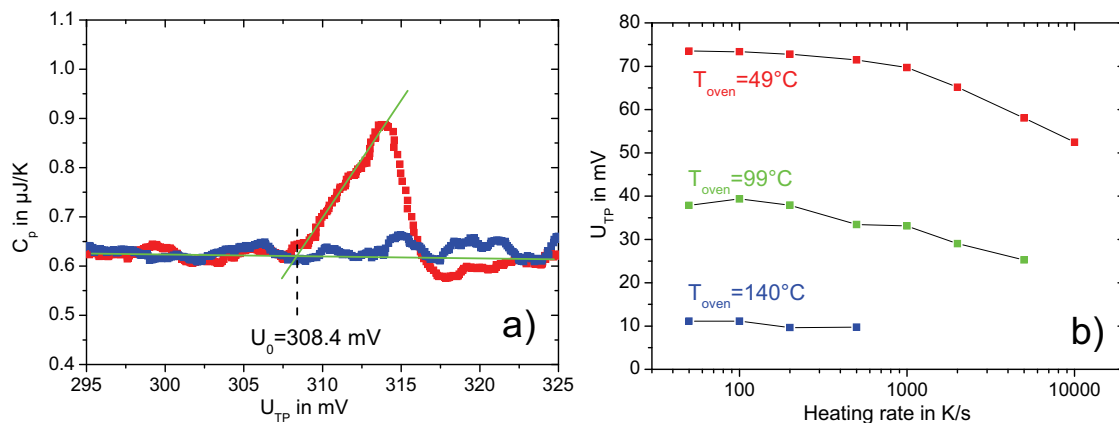
Figure 3.22: a) definition of the melting point as the onset of melting for lead at $T_0 = -103$ °C; b) heating rate dependence of the measured melting point of indium at oven temperatures of $T_0 = 49$ °C (blue points), 99 °C (green) and 140 °C (red). Sensor: TCG3880.
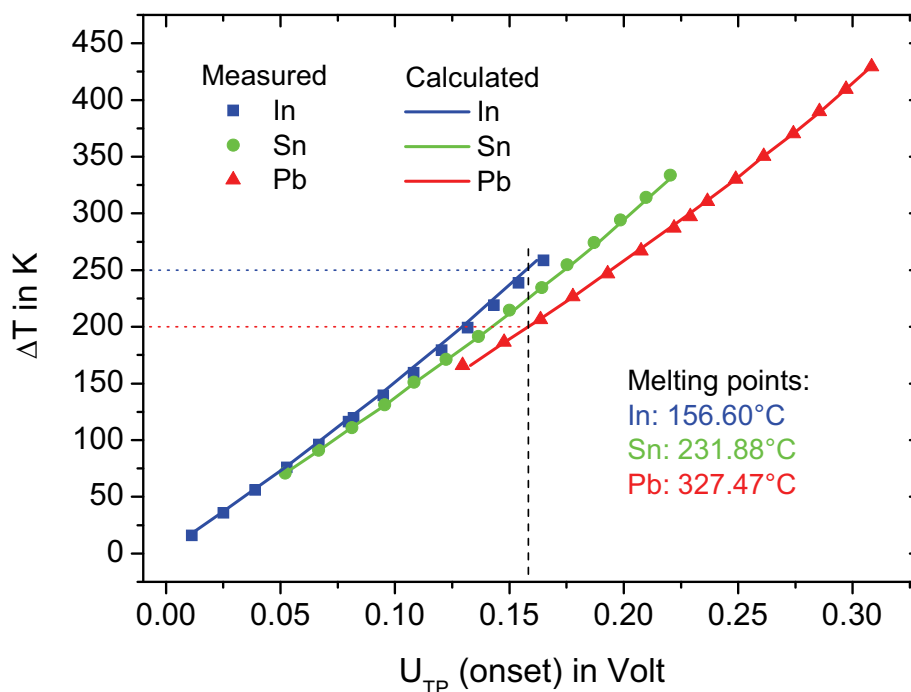
Figure 3.23: Thermopile calibration of the TCG3880 sensor. Overheating (temperature difference between the sample and the oven) against the thermopile voltage for melting points of In, Sn, and Pb at different oven temperatures. Symbols represent measured points; lines are from calculated function (section 3.5.4).

The value of thermopile voltage corresponding to indium melting point was found to be rate dependent – see Figure 3.22 (b). It changes slightly with an increase of heating rate from 50 K/s to 1 000 K/s and decreases significantly between 1 000 K/s and 100 000 K/s. This is because of heat capacity of the membrane outside the heater and limited thermal conductivity of the membrane between the heater and the thermocouples: at higher heating rate, more energy should be transferred

along the membrane per time unit. This increases the temperature gradient in the region between the heater and the thermocouples and so the temperature difference between the sample and the thermometer. Measured temperature during melting of indium is decreased by this difference. In fact, measured melting point shows linear heating rate dependence. In ideal case, the heating rate during calibration should be the same as for real measurements. A moderate heating rate of 500 K/s was chosen.

Overheating $\Delta T = T_s - T_0$ is plotted versus thermopile voltage U_{TP} in Figure 3.23. Each color corresponds to one metal i.e. one hot junction temperature.

Thermopile voltage is a function of two variables (sample temperature and oven temperature), so the calibration function is two-dimensional. The question was how to reduce its dimensionality.

3.5.3. Simple approach: $\Delta T = f(U_{TP})$

At first, thermopile voltage was considered depending only on the overheating $\Delta T = T_s - T_0$. For the calculations (to get the sample temperature) in this case one needs a function that converts thermopile voltage into overheating: $\Delta T = f(U_{TP})$. However, even if the curves in Figure 3.23 look close to each other, one gets different values of ΔT for the same voltage U_{TP} from different calibration curves. For example, voltage of about 0.16 V (vertical dashed line in Figure 3.23) corresponds to 200 K overheating in case of lead (oven temperature $T_0 = 127$ °C) and about 250 K overheating for indium ($T_0 = -95$ °C). The difference of 50 K is not acceptable.

3.5.4. Reverse calibration. Electrical potential

To solve the problem, the following model was used. Consider one thermocouple consisting of different conducting materials as shown in Figure 3.24. One material (material *"A"*) is used for conductors *1* and *3*; another one (material *"B"*) is used for conductor *2*. In our case, the two materials are n- and p-doped silicon. The thermocouple has two junctions, one under the sample (it has the sample temperature T_s) and another on the frame (it has the oven temperature T_0). Connecting wires (*4* and *5*) are made of the third material (material *"C"*); so there are additional connections from material *"A"* to material *"C"* at the oven temperature. In our case, conductors *4* and *5* are made of a series of materials: thin aluminum wires connect semiconductor stripes on the membrane to gold-coated nickel pins that are welded to copper wires with lead/tin solder. However, contacts in lines *4* and *5* consist of the same series of materials and have the same temperature (even it is not exactly T_0 due to gradients in the system), so this does not influence the measured voltage U_{tc}; one can discuss each pair of connections it the same way as *1-4* and *3-5*, see below.
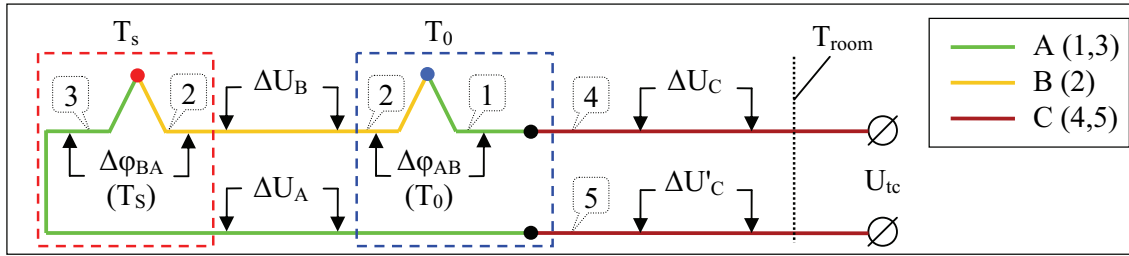
Figure 3.24: Electrical schema of the thermocouple. Conductors *"1"* and *"3"* are made of thermocouple material *"A"*, *"2"* – thermocouple material *"B"*, connecting wires *"4"* and *"5"* are made of material *"C"* (finally copper, see text). T_{room} is a room temperature; it is not used and shown only for clarity.

The output connections U_{tc} are connected at room temperature to a voltmeter. In our case, the voltmeter consists of an amplifier and an ADC converter. The input impedance of the amplifier is high, thus the electrical current is negligible.

Three effects contribute to the output voltage of the thermocouple: (i) contact potential difference; (ii) "thermoelectric power" in the volume with temperature gradient due to charge carrier diffusion; (iii) phonon drag.

Contact potential difference $\Delta\varphi$ is caused by the difference in the work function W between conducting materials x and y at the contact temperature T: $\Delta\varphi_{xy}(T) = \dfrac{W_y(T) - W_x(T)}{-e}$; here e is charge of an electron.

In a conductor with temperature gradient, free charge carriers on the hot side have higher impulses than that on the cold side; therefore, charge flow from the hot side to the cold side is not compensated by the charge flow in the opposite direction. This produces gradient in the charge carrier density and thus an electric field; the latter creates a flow of the charge carriers in the opposite direction. In steady state, these two flows are compensated with remaining electrical field $E = S \cdot \nabla T$ where S is Seebeck coefficient of the material. On the wire with one end at temperature T1 and another end at temperature T2, there is a voltage called thermoelectric power:

$$\Delta U = \int_{x_1}^{x_2} S(T) \cdot \nabla T \cdot dx = \int_{T_1}^{T_2} S(T) \cdot dT \tag{3.2}$$

Similar to charge carriers, phonon flows hot→cold and cold→hot are not compensated. When phonons interact with charge carriers, the latter are pushed against the temperature gradient. This effect is significant only at low temperatures (below 200 K) and included in Seebeck coefficient.

The measured voltage U_{tc} according Kirchhoff's Voltage Law is:

$$U_{tc} = \Delta U_C + \Delta\varphi_{CA}(T_0) + \Delta\varphi_{AB}(T_0) + \Delta U_B + \Delta\varphi_{BA}(T_S) - \Delta U_A + \Delta\varphi_{AC}(T_0) - \Delta U'_C \qquad (3.3)$$

As $\Delta\varphi_{xy} = -\Delta\varphi_{yx}$ and $\Delta U_C = \Delta U'_C$ the first two and the last two terms in (3.3) are compensated. Using expression for ΔU from (3.2), we can rewrite this equation:

$$U_{tc} = \Delta\varphi_{AB}(T_S) - \Delta\varphi_{AB}(T_0) + \int_{T_0}^{T_S}(S_B(T) - S_A(T))dT \qquad (3.4)$$

This equation can be separated into two parts, one part being function of only temperature T_S and another one being similar function of T_0.

$$U_{tc} = \left\{ \Delta\varphi_{AB}(T_S) + \int_{T_x}^{T_S}(S_B(T) - S_A(T))dT \right\} - \left\{ \Delta\varphi_{AB}(T_0) + \int_{T_x}^{T_0}(S_B(T) - S_A(T))dT \right\} \qquad (3.5)$$

Here T_x is some constant temperature, for example 0 °C.

We do not know the absolute value of $\Delta\varphi$ at any temperature. Instead, only its change with the temperature is measured. Therefore, I define calibration function $F(T)$ with some constant X:

$$F(T) = \Delta\varphi_{AB}(T) + \int_{T_x}^{T}(S_B(T^*) - S_A(T^*))dT^* + X \qquad (3.6)$$

X can be equal for example $(-\Delta\varphi_{AB}(0 °C))$. Then equation (3.4) transforms to

$$U_{tc} = F(T_s) - F(T_0) \qquad (3.7)$$

The thermopile in TCG 3880 consists of six thermocouples connected in series. If all the hot junctions have temperature T_s and all the cold junctions have temperature T_0, equation (3.7) is also valid for the whole thermopile. The temperature dependent part of the function $F(T)$ in this case is six times higher than that of a single thermocouple.

So both the hot and the cold junction of the thermopile can be described with a single function $F(T)$. To define this function in the complete required temperature range one should take some smooth analytical function and fit it to the measured data as described below.

To find parameter values which give the best fit of the equation (3.7) for all measurements of different reference materials and different oven temperatures a set of parameters $(a_1, a_2, \ldots)$ is needed that gives the minimum for the following *Error* function:

$$Error(a_1, a_2 ...) = \sum_i \left\{ (U_{measured})_i - \left(F((T_s)_i, a_1, a_2 ...) - F((T_0)_i, a_1, a_2 ...) \right) \right\}^2 \qquad (3.8)$$

Here i is the number of the measurement.

Note that (3.8) is significantly different from a "classic" function fit. In the "classic" case, one has an array of arguments x_i and array of values of function F_i; one looks for a function $F(x)$ that best fits the equation $F(x_i) = F_i$ for all i. Here I have two arrays of arguments, x_i and y_i, and an array of the differences of the function values for two arguments ΔF_i and the equation $F(x_i)-F(y_i) = \Delta F_i$ should be fitted for all i.

A second order polynomial $F(T) = a_0 + a_1 \cdot T + a_2 \cdot T^2$ was found to be suitable function. The measured thermocouple voltage is always a difference of values of calibration function at two temperatures, therefore the constant term X in (3.6) can be chosen freely. I have chosen $a_0 = 0$ having temperature expressed in degrees Celsius, so the calibration function $F(T)$ equals zero at zero temperature $F(0\ °C) = 0$. In this case, $F(T)$ equals to the measured thermopile voltage when the sample junctions are at temperature T and the reference junctions are at zero degrees Celsius: according to (3.7) if $T_0 = 0\ °C$ then $F(T_0) = 0$ and $U_{tc}=F(T_s)$.

The fit was performed using Mathcad® software. The code is presented in Appendix B. The resulting calibration function is the blue line in Figure 3.25.

The usage of the calibration is as follows. According to (3.7):

$$F(T_s) = U_{measured} + F(T_0) \qquad (3.9)$$

To obtain sample temperature, a reverse function F^{-1} [1] is applied to both sides of (3.9):

$$T_s = F^{-1}\left(F(T_0) + U_{measured} \right) \qquad (3.10)$$

The calculation is graphically represented by the red arrows in Figure 3.25. For a certain oven temperature one takes the value $F(T_0)$ and according to (3.9) adds the measured thermopile voltage U_{tc}; then the reverse calibration function according to (3.10) gives the sample temperature. Special care was taken in the software to have exactly the same although not analytically expressed relation between T and $F(T)$ for forward and reverse transformation to keep $F^{-1}(F(T)) \equiv T$ and still perform calculations fast enough for large number of points.

---

[1] Reverse calibration function F^{-1} is defined so that $F^{-1}(F(T)) \equiv T$ for any temperature T.
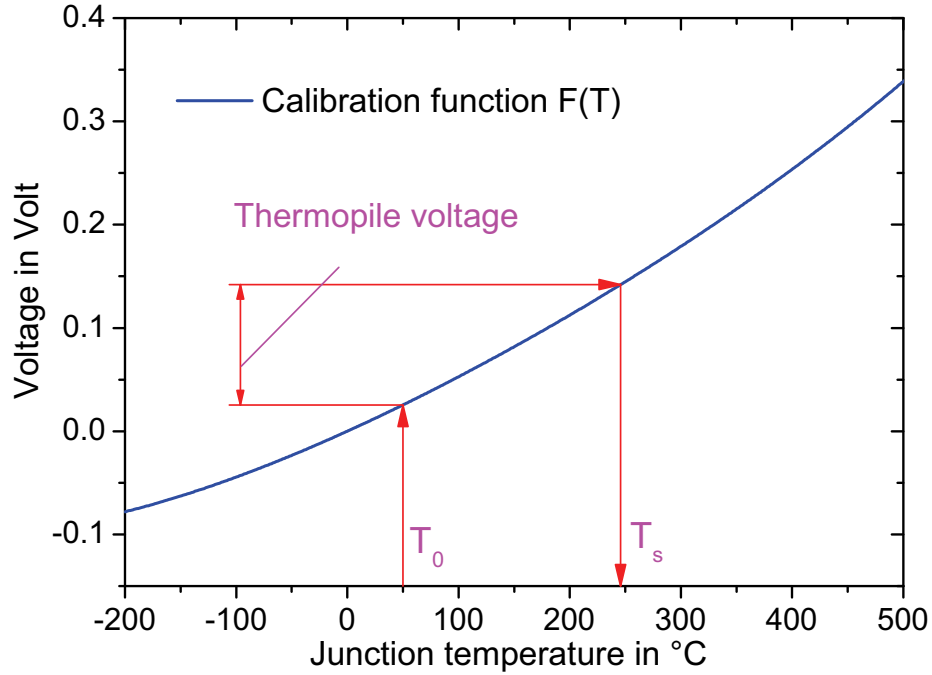
Figure 3.25: Calibration function and scheme of calculation of the sample temperature.

Temperature calculated from the thermopile voltage according to this calibration is represented by the lines in Figure 3.23. It is in good agreement with the measured points.

The deviation of the measured points from the calculated line using a second order polynomial is less than 5 K. Higher order polynomials for function *F(T)* give better fit for the measured points but regions away from the measured points become more curved and this leads to larger deviations, so higher order polynomials should not be used.

A thermodynamic model of any thermocouple consisting of two metals was developed by V. A. Drebushchak [47]. He has shown, that the voltage of any metal thermocouple with one junction at temperature *T* and another junction at zero Kelvin can be expressed as

$$U(T) = \varepsilon_0 \left[T - \Theta_V \ln\left(1 + \frac{T}{\Theta_V}\right) \right] \qquad (3.11)$$

with limiting sensitivity ε_0=86.17 µV/K and characteristic temperature Θ_V which is specific for the metals pair.

According to indium measurements, an average sensitivity of our thermopile is 0.66 to 0.8 mV/K; taking into account that the thermopile consists of 6 thermocouples the sensitivity of a single thermocouple is at least 220 µV/K which is significantly higher than 86.17 µV/K. The reason

is that we have a semiconductive thermocouple and its properties are different from metal. Still the function (3.11) can be used considering ε_0 as a fit parameter.

Temperature in (3.11) is in Kelvin and the voltage equals zero at zero Kelvin, so the formula had to be adapted for temperature in degrees Celsius and another reference junction temperature:

$$F(T) = \varepsilon_0 \left[T + 273.15 - \Theta_V \ln\left(1 + \frac{T + 273.15}{\Theta_V}\right) \right] + F_0 \qquad\qquad (3.12)$$

Here T is temperature in grad Celsius, ε_0 and Θ_V are fit parameters, constant F_0 is defined such way that $F(0\ °C)=0$.

A fit was done with melting of indium with a newer sensor XI240 (see section 3.9 on page 59) in the range of oven temperatures from -190 °C to 150 °C. Fit parameters are: $\varepsilon_0 = 4.156*10-3$ V/K; $\Theta_V = 307.14$ K; $F_0 = -0,323$ V. This corresponds to a value of $\varepsilon_0 = 693$ µV/K for a single semiconductive thermocouple, which is 8 times more than the limiting value of 86.17 µV/K for the metal thermocouple reported by Drebushchak [47].
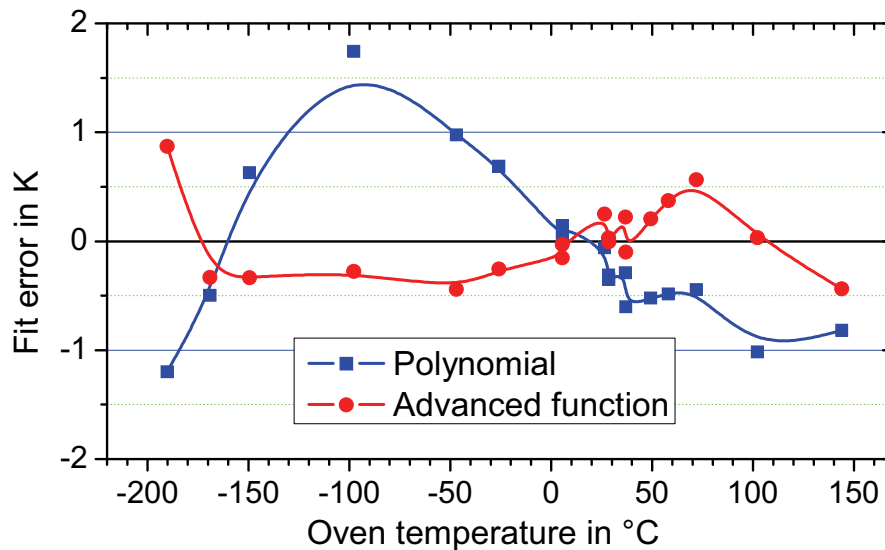
Figure 3.26: Fit error for second order polynomial and function (3.12). Data: indium melting point at oven temperatures from -190 °C to +150 °C. Sensor: XI240.

The quality of the fit is presented in Figure 3.26 by the difference between measured and calculated temperature for second order polynomial (blue squares) and for the function (3.12) (red dots).

The fitting error is up to 2 K for polynomial and below 1 K for function (3.12). This shows that the function (3.12) can be used to describe a semiconductive thermopile and it gives better results than a second order polynomial.

The paper [47] appeared during writing of this thesis after the experiments were done, so a second order polynomial function was used in all experiments for temperature calibration. Still the calibration with only indium reference (without tin and lead) works reasonable well (deviation less than 2 K) in the temperature interval from -180 °C to 200 °C and this is the region where all measurements were performed.

3.5.5. Temperature distribution in the membrane

Actually if we have a look onto the sensor (Figure 3.1 (c) on page 13), we can see that the thermocouples are not just on the heater, but four of them are located outside at a distance of 50µm from the heater stripes and another two are at about 120 µm from the heated zone. The question is, "What is the temperature distribution around the heater and what is the temperature of the sample in compare to that measured by the thermocouples?"
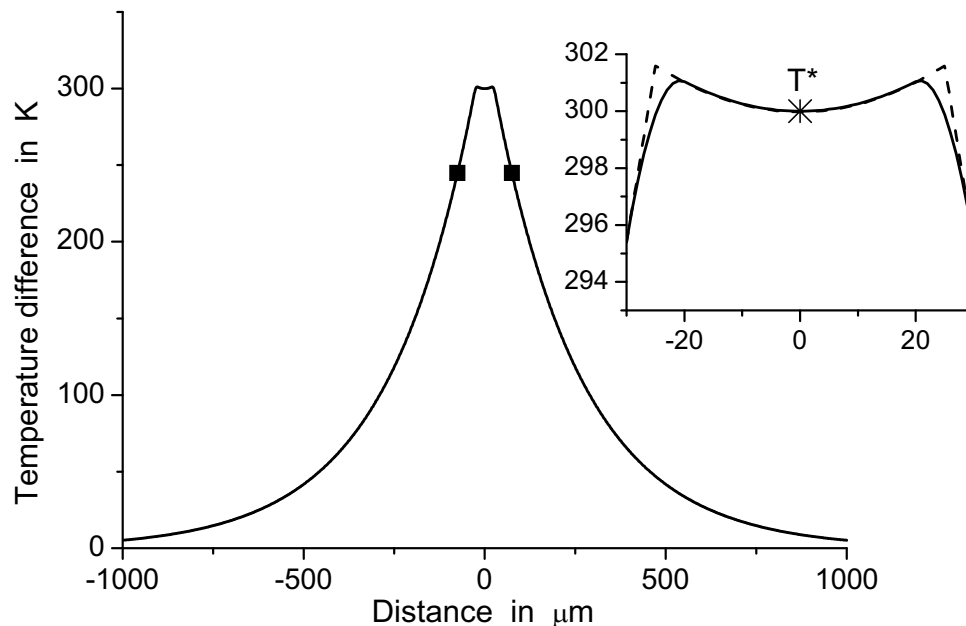
Figure 3.27: Temperature distribution T(x,0) in the membrane plane along the X axis at T* - T_0 = 300 K. The square spots point to the position of the thermocouples. The central region is shown enlarged in the insert: the dashed curve was calculated for the infinitely thin heater and the solid line corresponds to 5 µm wide heater stripes.

Assume the thermal properties (heat capacity, thermal conductivity) of the membrane and the surrounding gas are temperature independent, so we can describe temperature distribution in terms of overheating (temperature difference to the surrounding $T - T_0$) instead of absolute temperature.

Assume also the silicon frame and the thermopile cold junctions are far enough from the heated area. In this case temperature distribution in the membrane without a sample can be calculated theoretically [25]. Resulting static temperature distribution for the overheating of the membrane center (sample position) of $T^* - T_0 = 300$ K is shown in Figure 3.27. Overheating at a distance of 1 mm (position of the silicon frame) is below 2 % of the overheating of the membrane center. Therefore, the boundary conditions at the membrane periphery are not important for the calculation of the temperature distribution around the heater.

As one can see, the temperature difference measured by the thermocouple is about 82 % of the whole temperature difference between the sample and the surrounding. As the thermopile has only four such thermocouples, and another two that are even further from the heater, the actual average temperature measured by the thermocouple is even less. Nevertheless, this does not make the thermopile calibration procedure completely wrong even for the sensor TCG3880: in the calibration function, we get not a "real", but an "effective" sensitivity. The situation was improved by the introduction of a new sensor, XI240, where thermocouples are inside the heated area, see section 3.9 (page 59).

3.6. Computer control

Only simple heat-cool cycle was possible with the generator; setting of the maximum temperature and heating rate was indirect. To perform advanced investigations of materials, there was a need to execute complex temperature programs with different heating and cooling rates, melting temperatures, isothermal times and other parameters. On large temperature scales, temperature dependence of the heater resistance and nonlinearity of heat losses should be taken into account. Therefore, heater power had to be controlled according to program of the experiment and other factors. Good solution is a computer-based system with digital-to-analog (DAC) and analog-to-digital (ADC) converters. Heater voltage should be controlled by the DAC; heater power, heater resistance and thermopile voltage should be measured by ADC. After the measurement, heat capacity can be calculated as described in section 3.2.1.

3.6.1. Mathematics

The idea of the measurement is to control sample temperature according to the desired time-temperature profile and to obtain material properties out of the system response during and after the change of temperature. The "program temperature" is defined as a function of time $T_{prog}(t)$.

Widely used method of temperature control is to measure the sample temperature continuously and adjust heater power so that the measured temperature follows the program temperature. However, high speed of the measurement (DAC update rate of 50 000 samples/s was typically used)

does not allow calculation of the output voltage on the fly: operating systems of modern computers are too slow for this. Therefore, output voltage has to be calculated in advance and sent to the DAC buffer before the measurement.

Heater power can be calculated according to equation (2.3): $P = \left(C_s + C_{add}\right) \cdot \dfrac{dT}{dt} + \xi$. This formula contains two unknown terms: heat capacity and heat losses. One could take into account addenda heat capacity, but sample heat capacity is not known before the measurement. Another point, for relatively slow experiments, heat losses term is much larger than the heat capacity term. Therefore, we neglect heat capacity term and set heater power according to heat losses only. It was already mentioned in section 3.2.1, that the heat losses function depends mostly on overheating. "Programmed overheating" is used here to calculate the "program heater power":

$$P_{heat}(t) = \xi\left(T_{prog}(t) - T_0\right) \tag{3.13}$$

There was a try to add the second, "heat capacity", term to the control algorithm, but it did not improve the situation significantly. Therefore, the simple formula (3.13) was used for heater power.

The dependence $\xi(T_s\text{-}T_0)$ can be defined from a relatively slow symmetric heating-cooling scan (typically 200 or 500 K/s was used); heater power as a function of overheating $(T_s\text{-}T_0)$ is fitted by a second order polynomial (Figure 3.28 a). Constant term is set to zero during this fitting, because heat losses are zero at zero overheating.
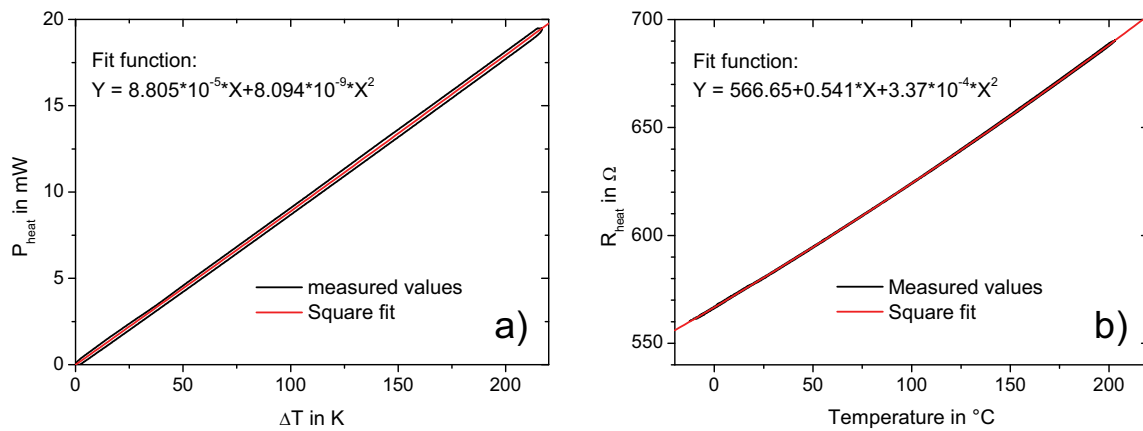
Figure 3.28: Calibration functions for the heater control: a) heater power versus overheating; b) heater resistance versus temperature. Sensor: TCG3880; helium surrounding at 10 kPa; heating rate 500 K/s (assumed thermopile sensitivity 0.5 mV/K); $T_0 = -14$ °C; sample: iPP, mass about 100 ng.

For each measurement, heater power is calculated according to (3.13) as a function of time. To control the heater one should apply certain voltage by the digital to analog converter. To get certain power P_h on the heater with electrical resistance R_h, one has to apply following voltage:

$$U_h = \sqrt{P_h \cdot R_h}$$

(3.14)

The heater is connected to an amplifier in series with a reference resistor R_{ref}; output resistance of the amplifier is R_{out}. "Unloaded" output voltage of the amplifier is

$$U_{out} = \frac{R_h + R_{ref} + R_{out}}{R_h} \cdot U_h = \frac{R_h + R_{ref} + R_{out}}{R_h} \cdot \sqrt{P_h \cdot R_h} = \left(R_h + R_{ref} + R_{out}\right) \cdot \sqrt{\frac{P_h}{R_h}}$$

(3.15)

The output amplifier (gain G_{out}) is controlled by the DAC output voltage U_{DAC}:

$$U_{DAC} = \frac{U_{out}}{G_{out}} = \frac{R_h + R_{ref} + R_{out}}{G_{out}} \cdot \sqrt{\frac{P_h}{R_h}}$$

(3.16)

The only unknown parameter in (3.16) is the heater resistance. It is also defined from the calibration scan mentioned above and fitted as a function of absolute temperature by a second order polynomial (see Figure 3.28 b).

Equation (3.16) gives DAC output voltage U_{DAC} needed to achieve any desired sample temperature. This eliminates the need of an ultra-fast real time control circuit for the heater and allows calculating DAC voltage as function of time in advance.

3.6.2. Hardware

Hardware part of the computer-controlled calorimeter (Figure 3.29) consists of a sensor 1, amplifier block 2 and ADC/DAC board 3 inside the personal computer (PC). The details of the electronics are given in Appendix A.

The output voltage of a Digital-to-Analog Converter (DAC) is amplified with a buffer amplifier IC1 and applied to the heater in series with a reference resistor R_{ref} (100 Ω). Voltage from the reference resistor (heater current signal) and heater voltage are amplified with amplifiers IC2 and IC3 respectively and are fed to inputs of an Analog-to-Digital Converter (ADC). This gives a possibility to measure heater current and heater voltage independently, so a true value of heater power and heater resistance can be calculated.
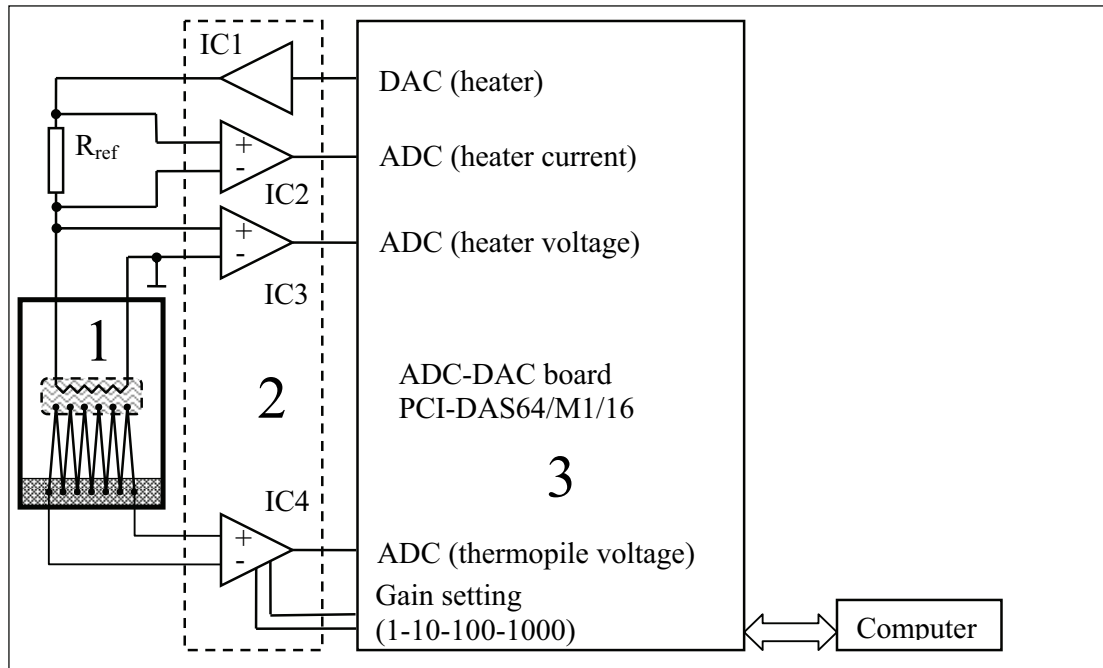
Figure 3.29: Scheme of the calorimeter: 1 - sensor; 2 – amplifier; 3 – ADC/DAC board

Another amplifier (IC4) is used for the thermopile voltage. It has a 2-bit digital (TTL) input to change the gain between 1, 10, 100 and 1000. This input is connected to the digital output of the ADC-DAC board; the amplifier output is connected to the ADC input.

3.6.3. Software

For any measurement, desired sample temperature is defined as a function of time as described in Appendix C. To realize the time-temperature profile program temperature is tabulated at a certain DAC rate (typically 50 000 samples/s). For each point static heater power P_h and heater resistance R_h are calculated from the calibration functions shown in Figure 3.28; corresponding DAC voltage is calculated according to the formula (3.16). An array of DAC output voltages is sent to the DAC buffer. Then analog-to-digital (ADC) and digital-to-analog (DAC) converters are started simultaneously and the experiment is performed.

After the measurement, three ADC channels (heater voltage, heater current and thermopile voltage) are zero-corrected and recalculated into thermopile voltage, heater resistance and heater power according to sensitivity of each channel, gain of the amplifiers IC2, IC3 and IC4 and the resistance of the reference resistor R_{ref} (Figure 3.29). Thermopile voltage is recalculated into sample temperature.

Then heat losses function needed for heat capacity is calculated using a polynomial function. Either the actual (last) measurement can be used to fit the measured power versus overheating

dependence (see Figure 3.4 on page 17) or the polynomial can be "frozen" after one of previous calculations. This is useful for example to evaluate very fast measurements, where a polynomial from some slower measurement could be used. Then the heat capacity is calculated as described in section 3.2.1.

The result of the measurement can be saved as a text file containing time, heater resistance, heater power, thermopile voltage, sample temperature, overheating, heating rate, heat capacity, step number of the temperature program and some other values. Detailed description of the software is given in Appendix C.

3.7. Test of computer controlled system: polyethylene

To test the computer controlled system, the same polyethylene as before (see section 3.4.3 on page 36) was measured. Temperature program of the experiment is shown in Figure 3.30 (a).

The sample was molten, then rapidly cooled down to crystallization temperature and kept for 1 s, rapidly cooled down to the oven temperature of -183 °C and heated up to 170 °C at 5 000 K/s. Maximum measured cooling rate was about 50 000 K/s on the first cooling segment and about 100 000 K/s on the second cooling segment. Crystallization temperature was varied between 0 °C and 130 °C.
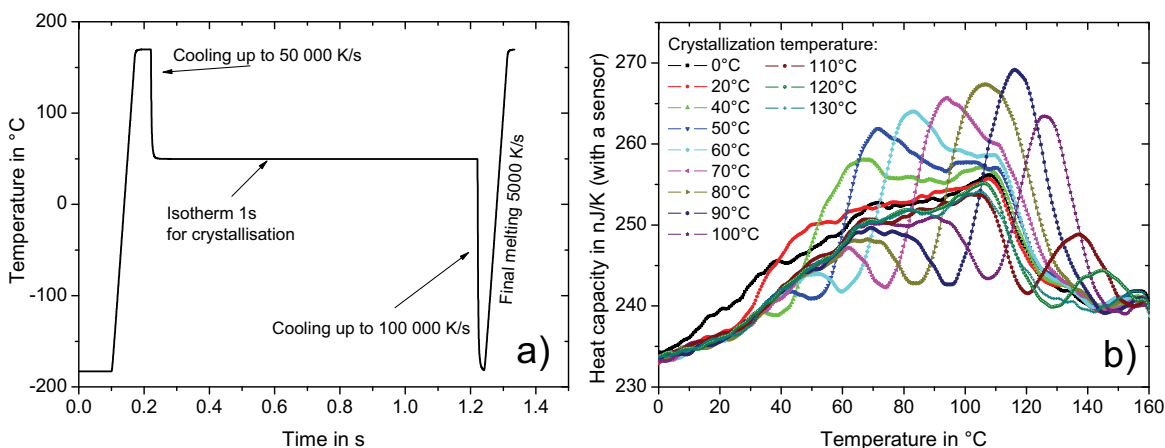
Figure 3.30: a) Temperature program; b) melting curves ("final heating") of polyethylene (NBS SRM 1484). T_0 = -183 °C; T_{melt} = 170 °C; t_{iso} = 1 s. Surrounding: helium at atmospheric pressure. Sample mass about 100 ng. Sensor: TCG3880.

In the heating curves (Figure 3.30 (b)), there is a broad melting peak between 30 °C and 130 °C common for all crystallization temperatures. However, after 1 s crystallization, no melting occurs between the crystallization temperature and 10 K above it; then the large melting peak starts. This means after fast cooling there is a broad distribution of crystal sizes, which gives a broad melting peak (from 30 °C to 120 °C). If the sample is annealed at some temperature (for example 70 °C)

then the crystals with melting temperatures between 70 °C and 80 °C are perfecting to more stable structures and in the melting curve there is a gap between 70 °C and 80 °C; an additional peak between 80 °C and 105 °C is seen.

This effect is already known as "fractionated crystallization"; it was observed for example in confinement in immiscible blends or diblock copolymers [48] or in HDPE [49]. However, reorganization takes place on heating in common DSC, so the effect is less pronounced.

This shows that the calorimeter gives reasonable results on polymer materials.

3.8. Intermediate rate range: syndiotactic polypropylene

We have already full crystallization kinetics for PCL (Figure 3.18) and iPP [50, 51]. Only the high temperature part of crystallization kinetics for polyethylene could be studied because this material crystallizes too fast for the technique. Other materials like **syndiotactic polypropylene (sPP)** crystallize too slowly: heat production rate during crystallization is too low to be detected with our device. On the other hand, it crystallizes too fast for conventional DSC calorimeters. In Figure 3.31(a), DSC heat flow versus time is shown for crystallization at temperatures between 100 °C and 120 °C. Crystallization halftime of pure sPP as well as of that with addition of 1 % of carbon nanotubes (CNT) are plotted in Figure 3.31(b). One can see that influence of 1 % nanofiller is huge – crystallization process becomes about 10 times faster at 110 °C. However, crystallization halftimes shorter than one or two minutes are not accessible by DSC; therefore further developing of the curves in the region of question marks in Figure 3.31(b) cannot be investigated by these devices. On the other hand, the fast scanning device does not see crystallization peaks longer than several seconds.
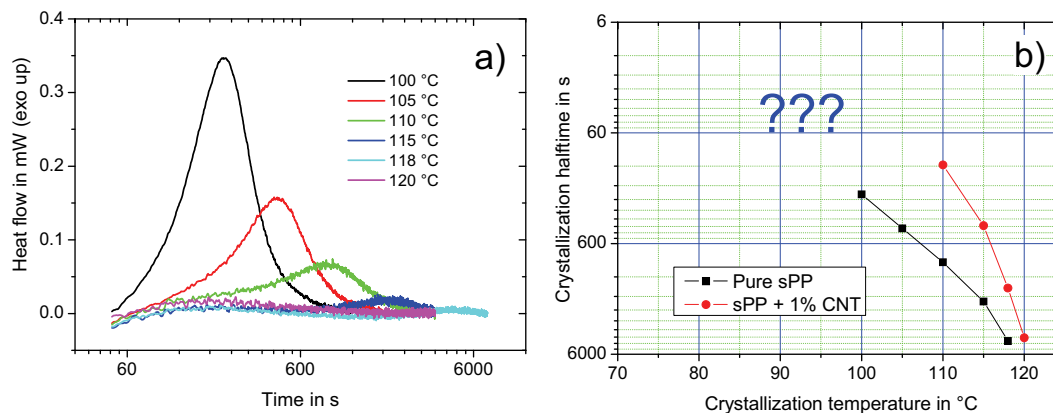
Figure 3.31: Crystallization curves of pure sPP: a) DSC curves; b) halftime versus temperature. Pyris DSC (Perkin Elmer). Sample mass: pure sPP – 2.6 mg; sPP + 1% CNT – 5.25 mg.

As one can see, there is a need in a technique for intermediate range between DSC and fast scanning calorimetry. In this section, it is shown how crystallization kinetics of such materials can be studied by our new calorimeter. Influence of nanofiller – carbon nanotubes (CNT) on the crystallization kinetics of syndiotactic polypropylene (sPP) was studied. Some studies of such materials are already published [52], however they were limited to high temperatures because of limitations of DSC technique. Three samples were investigated in this work: pure sPP, sPP + 1 wt.% CNT, sPP + 10 wt.% CNT. Syndiotactic polypropylene was obtained from Sigma-Aldrich, $M_w \sim 127\,000$, Prod. No. 452157. Thin multi-wall carbon nanotubes with carbon purity of 95 % were obtained from Nanocyl s. a. [53]. The nanocomposites were prepared using a laboratory-scale conical twin-screw extruder ThermoHaake Micro-Compounder Minilab [54]. The samples were kindly provided by F. De Santis, Salerno, Italy.

Following technique was used to investigate crystallization kinetics utilizing the fast scanning calorimeter. The sample was heated from the oven temperature of -50 °C to a temperature above the melting point (180…200 °C), kept 0.01 s, so the results were not affected by degradation. Then the sample was quenched to the crystallization temperature, kept for crystallization time and quenched to -50 °C. Afterwards it was heated up again to check the melting peak. Cooling to -50 °C was needed for better comparison of melting curves after different crystallization temperatures as well as to check the step height of the glass transition. The lowest temperature of -50 °C is well below the glass transition temperature and the cooling/heating rate of 1000 K/s is high for the material, therefore this cooling and heating back to the crystallization temperature should not influence the structure.
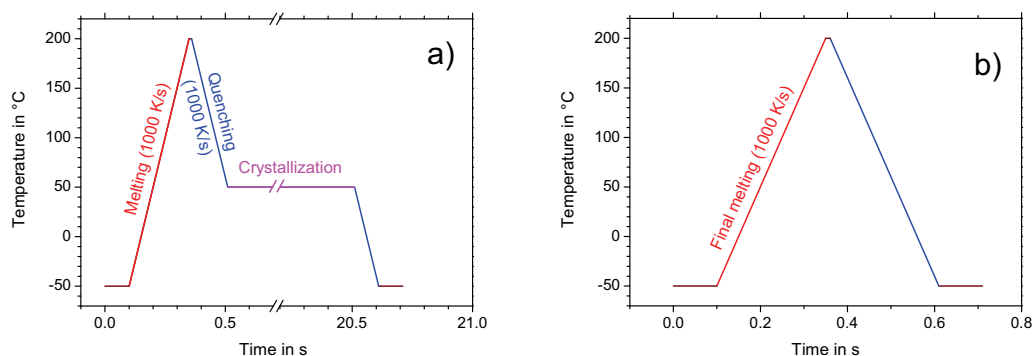
Figure 3.32: Temperature program for long-time crystallization study: a) crystallization part (low ADC rate); b) melting part (high ADC rate). Maximum temperature 200 °C, oven temperature -50 °C; all heating/cooling rates 1000 K/s.

Crystallization time had to be quite long (> 1 s) and the heating afterwards quite fast. One needs low ADC sample rate for long measurements, so that all points fit into the memory, and high sample rate to evaluate the fast heating processes. The temperature program was divided into two

parts (Figure 3.32); the first one with low ADC rate and the second one with high ADC rate.

All three samples were crystallized at temperatures between 20 and 120 °C in 10 K steps. Crystallization time was set between 1 s and 200 s (sometimes longer) with three measurements per decade (1-2-5-…). Selected melting curves are presented in Figure 3.33.

As one can see, no crystalline structure is formed at both temperatures (30 and 120 °C) within 1 s. There is a glass transition at 10…20 °C. With increasing crystallization time, a melting peak appears. It starts at 50…60 °C after crystallization at 30 °C and at about 140 °C after crystallization at 120 °C. The melting peak after crystallization at 30 °C is broader than that after 120 °C (peak width at the half-height after crystallization for 500 s is 30 K and 19 K respectively). A stable structure is formed at 120 °C; it melts upon heating at a certain temperature: onset and peak position are not changed with increasing of crystallization time. Less stable structure is formed in a short time at 30 °C; on heating, it starts to melt at much lower temperature. With increasing crystallization time, onset is not changed significantly, while the peak grows towards higher temperatures. This indicates perfection of the structure during isotherm that leads to higher final melting temperature (whether with reorganization on heating or not).
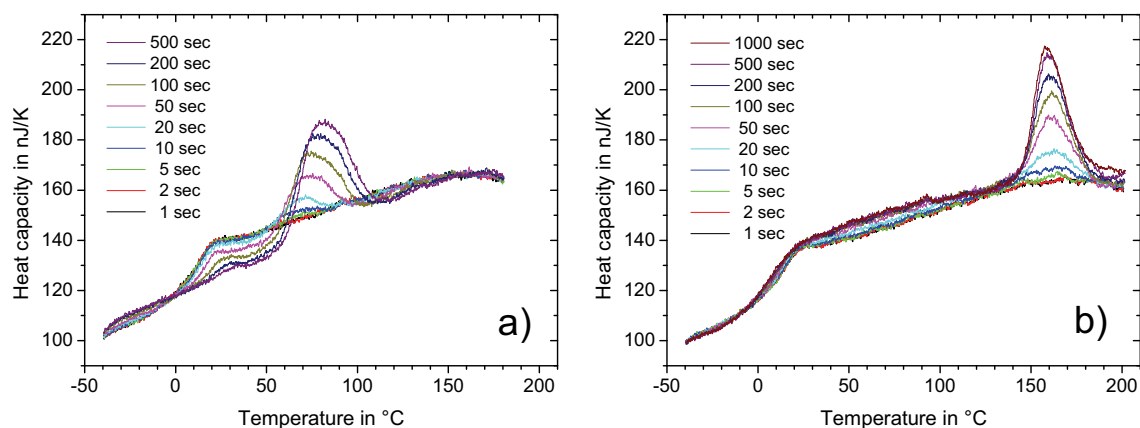
Figure 3.33: Melting curves of sPP + 1 % CNT crystallized at 30 °C (a) and 120 °C (b) for different time. Addenda heat capacity is not subtracted. $T_0 = -47.5$ °C. Heating/cooling rate 1000 K/s. Sensor: XI240.

Remarkably, the heat capacity step in the glass transition region decreases with increasing crystallization time at 30 °C and almost disappears after 500 s. Contrary, crystallization at 120 °C affects the step height of heat capacity in the glass transition very little; This effect was seen on all three samples (pure sPP, 1% CNT, 10% CNT). Step height in the glass transition of the crystallized sample increases continuously with increasing the crystallization temperature. This means final crystallinity decreases significantly with increasing crystallization temperature.

For all samples, crystallization temperatures and times, melting peak area was plotted as a function of logarithm of crystallization time (Figure 3.34 (a, b, c)). Melting peak areas after 500 s at 30 °C and 120 °C are not much different, so sample after 500 s at 30 °C had also low crystallinity. Together with almost no heat capacity step in the glass transition, this tells that three-phase model [55] should be applied to this material; it forms remarkable "rigid-amorphous" fraction at low crystallization temperatures but no detectable rigid-amorphous at high crystallization temperatures even with similar degree of crystallinity.
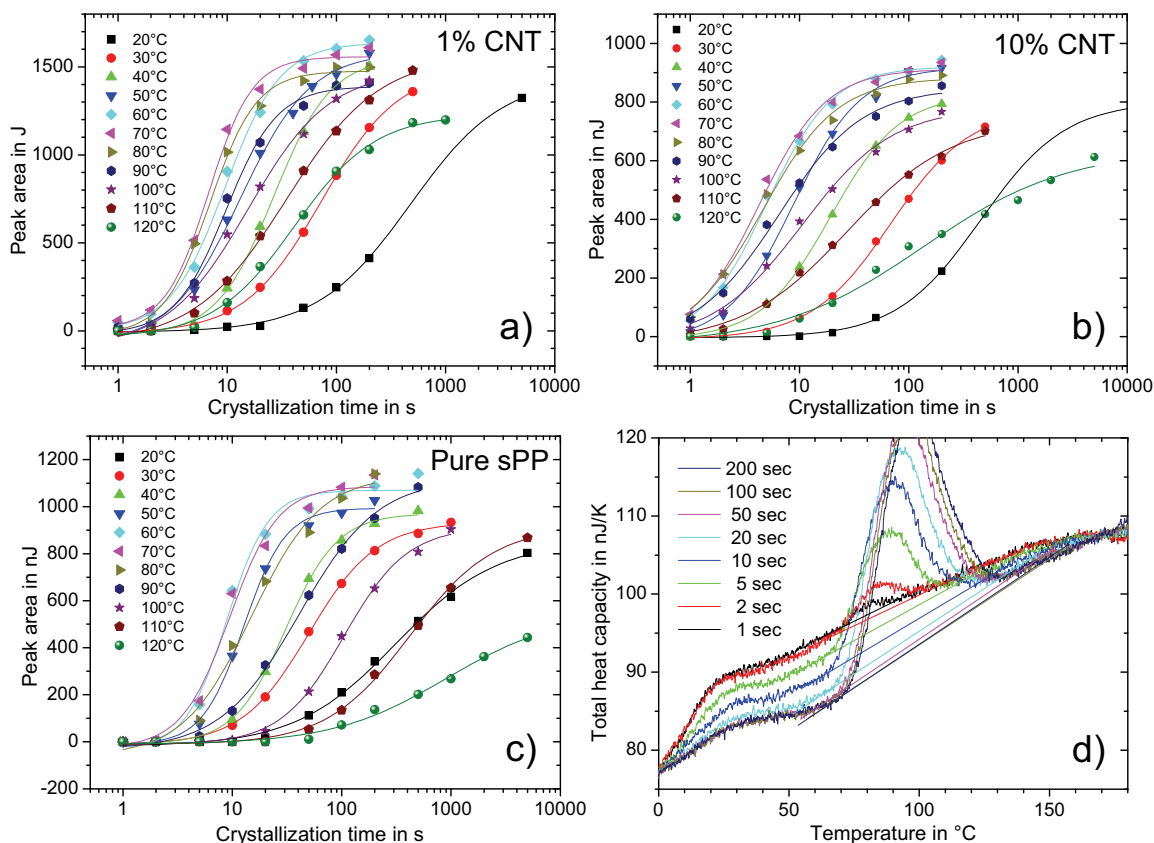
Figure 3.34: Melting peak area versus crystallization time of sPP and: a) 1 % CNT; b) 10 % CNT; c) pure sPP. Lines are guides to the eyes only; they represent sigmoid fit. Crystallization temperatures are indicated in the legend. d) definition of a base line heat capacity to calculate the peak area: sPP + 10 % CNT, crystallized at 50 °C; crystallization times are indicated.

For calculation of peak area, a straight line as a tangent to the curve before the peak and to some point on the curve after the peak was used as a baseline (Figure 3.34 (d)). Uncertainty of the baseline definition is increasing with increasing of the peak area. In addition, a measured absolute value of heat capacity in the melt did not exactly coincide. This is why simple sigmoid function and not Kolmogorov-Johnson-Mehl-Avrami theory as for example in [51] was used to determine the crystallization halftime, i.e. the crystallization time after which crystallinity (or peak area) reaches

the half of its asymptotic end value. Application of more complicated theories would need data that are more precise.

As it was mentioned before, melting temperature depends strongly on crystallization temperature. To look on this dependence more closely, melting peak temperature was plotted against crystallization time for 1 % CNT sample (Figure 3.35). With increasing crystallization time, peak temperature increases for low crystallization temperatures and slightly decreases for high crystallization temperatures.
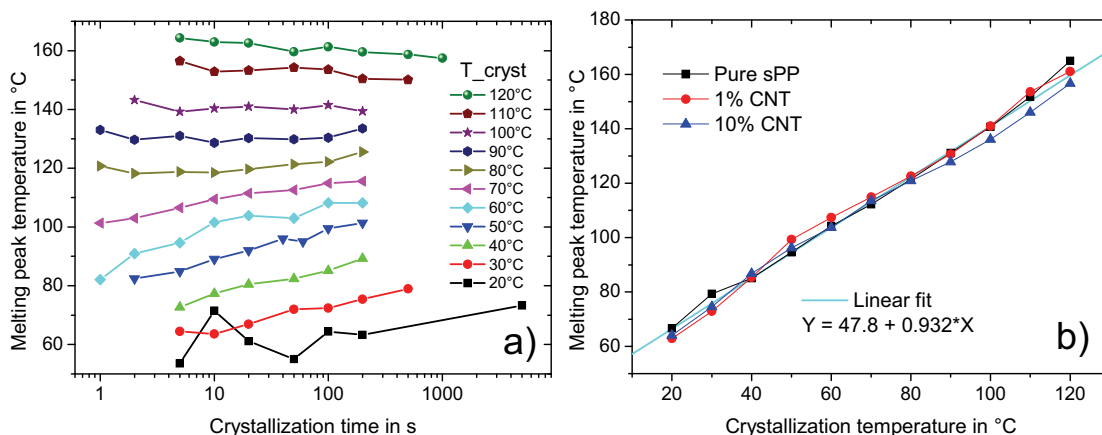
Figure 3.35: a) sPP + 1 % CNT: melting peak temperature versus crystallization time at different crystallization temperatures; b) sPP: melting temperature after crystallization for 100 s versus crystallization temperature.

Upon heating in DSC, one can observe three melting peaks [56]: one about 15 K above the crystallization temperature and another two at temperatures between 100 °C and 130 °C with very weak dependence on the crystallization temperature. This is due to recrystallization after melting at heating rate of 0.33 K/s (20 K/min) used in DSC. We have used heating and cooling rate of 1000 K/s, which is high enough to prevent such recrystallization on heating. Each experiment showed a single melting peak without complicated structure.

Crystallization time of 100 s was chosen for all temperatures for this and other two samples. Melting peak temperature versus crystallization temperature is presented in Figure 3.35 (b). As it follows from the graph, there is no filler dependence of the melting temperature; all three curves are on a straight line with a slope close to 1. The melting temperature is about 40 K above the crystallization temperature in the whole temperature range studied.

Overall crystallization rate for all three samples is shown in Figure 3.36. As in case of PCL (Figure 3.18), it is a bell-shaped curve. All three curves coincide on the low-temperature side. In this region, nucleation rate is high enough even without carbon nanotubes, crystallization rate is defined by the low mobility. On the high temperature side, crystallization rate is controlled by

nucleation, so sample with carbon nanotubes crystallizes an order of magnitude faster than the pure polymer. It is still not clear, why DSC curves come together at 120 °C, may be it was some surface nucleation effect. There is no significant difference between 10 % and 1 % of CNT in crystallization kinetics. This indicates saturation of the effect; for industrial applications, not more than 1 % filler is needed.
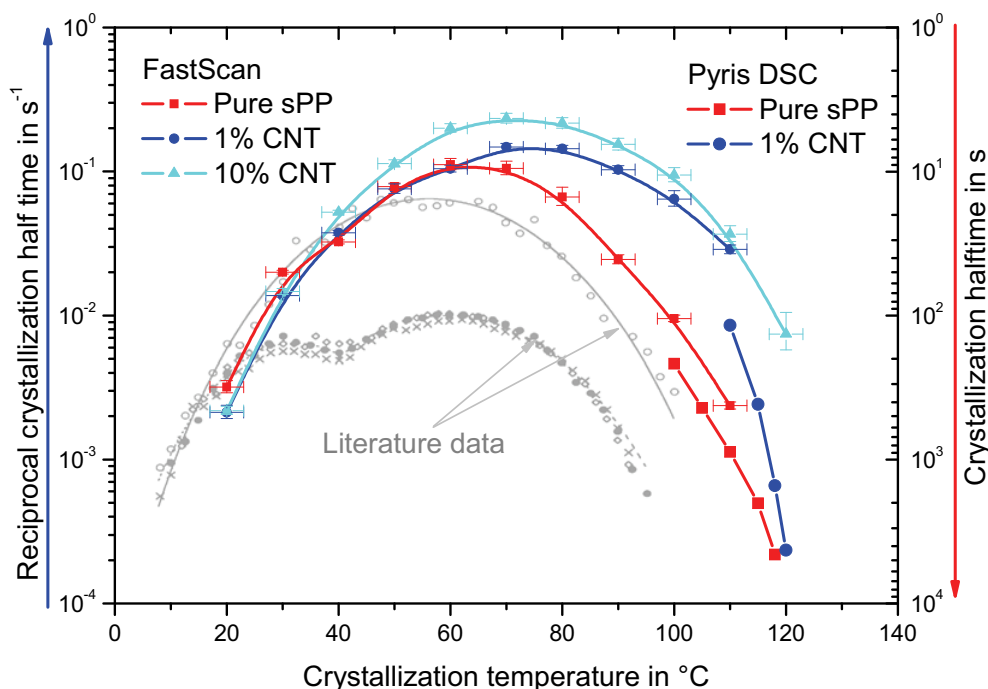
Figure 3.36: sPP and carbon nanotubes (CNT): overall crystallization rate. Data marked gray are taken from [57]: diamonds, crosses and filled circles represent crystallization from melt; open circles are from cold crystallization.

Similar data for "cold crystallization" of pure sPP was obtained by Supaphol and Spruiell [57] (open cycles in Figure 3.36). For "crystallization from melt", which should be similar to our experiment, Supaphol and Spruiell have obtained a double-bell-shaped curve (filled cycles in Figure 3.36). Such double peak is a result of interplay between the nucleation kinetics and crystal growth kinetics having maxima at different temperatures. In our data, there is a small shoulder in the curve of pure sample at 40 °C; it is at the same temperature as reported by Supaphol and Spruiell. However, our curve is generally similar to the "cold crystallization" presented by Supaphol and Spruiell, and the process is even faster at higher temperatures. Most probably, our sample has impurities that accelerate the nucleation process. With carbon nanotubes, overall crystallization rate is defined mostly by crystal growth kinetics and the shoulder at 40 °C is not seen. These experiments show that our technique works well also on the intermediate time scale.

3.9. Faster sensors

For PCL, it is possible to study isothermal crystallization in the whole temperature range between melting and glass transition temperature. In other words, any crystallization temperature was reached while the sample was still in amorphous state. For PE, cooling was not fast enough to prevent crystallization on cooling to crystallization temperatures below 110 °C, see Figure 3.19 on page 36.

One of the curves is shown on larger scale in Figure 3.37. It is a free ballistic cooling to the oven temperature of 108 °C; the heater was switched off at sample temperature of 170 °C. Even though the cooling starts quite fast (14 000 K/s) the last several Kelvin are done at only 500 K/s.
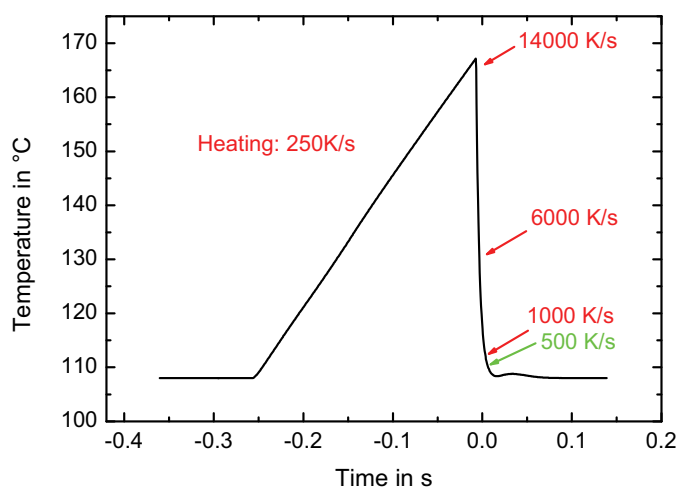
Figure 3.37: Temperature versus time for controlled linear heating and free cooling after switching off the heater power. The local rates are indicated at different temperatures. Surrounding: helium at 108 °C; pressure 5 kPa. Sample: ca. 100 ng polyethylene.

To obtain the sensor capabilities, the oven was set to some low temperature (-168 °C), the heater was switched on to maximum power and then off. Heating rate as function of temperature is presented in Figure 3.38 (a). Heating rate of up to 200 000 K/s and cooling rate of 160 000 K/s were observed with the sensor TCG3880 using the thermopile as temperature sensor.

The question is, "Is it the maximum rate for the sample?" Static temperature distribution was discussed in section 3.5.5 on page 47. However, temperature propagates from the heater to the positions of the thermopile hot junctions not instantly, but with some delay, so some additional, faster thermometer should be used to measure the heating rate of the sample.

Heater resistance could not be used as an "absolute" thermometer, see section 3.5.1. However, one can take dependence between the sample temperature (measured by the thermopile) and measured heater resistance from the same measurement and fit it with some smooth function (the

dependence is almost linear, so quadratic function is fine). Then this function can be used to calculate sample temperature from heater resistance for the particular experiment. Temperature evolution after switching the heater on and almost off (some voltage should remain to measure the resistance) is shown in Figure 3.38 (b). Heater temperature approaches the end value much faster than thermopile temperature; so actual heating/cooling rates are even higher than that shown in Figure 3.38 (a). However, the heater resistance signal is too noisy for heat capacity calculation.
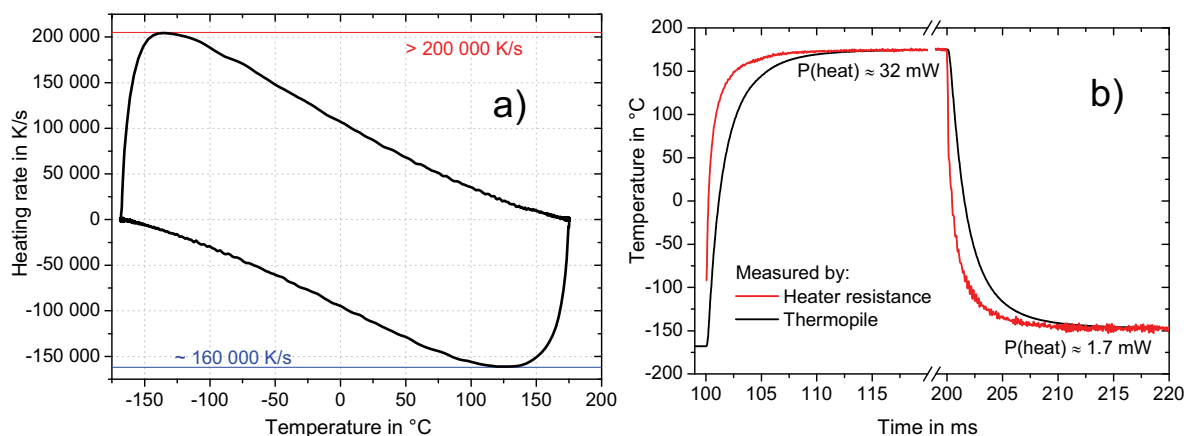
Figure 3.38: Scanning rate of the TCG3880 sensor: a) heating/cooling rate measured by the thermopile after switching the heater on/off; sample: small piece of indium; b) temperature evolution after rapid change of the heater power, empty sensor. Electronics according to Figure 3.29 (page 51); ADC rate 50314 scans/s, decimate factor 1, filter cutoff frequency 5 kHz. Surrounding: helium at atmospheric pressure. Oven temperature -168 °C.

To do faster measurements, hot junctions of the thermopile have to be closer to the sample, in the best case just under the sample, in the center of the heater. Different sensors were designed by Xensor Integration, the supplier [28]. Some of them are presented in Figure 3.39 with the same scale to show differences in the size of the active area.

The first TCG3880 sensor has six thermocouples around the $50*100\ \mu m^2$ heater; six thermocouples of the XI240 are located inside the $60*60\ \mu m^2$ heater (heater stripes including contact pads are 65 μm long). XI273 and XI292 have heater area of $19*27\ \mu m^2$ and $9*15\ \mu m^2$ respectively; each of them has only one thermocouple because of lack of space.

To illustrate the temperature resolution of the XI240 sensor, dotriacontane sample ($C_{32}H_{66}$) obtained from Fluka Chemie GmbH was heated at different rates. On heating, this material shows two endothermic peaks close to each other: solid-solid transition at (64 ± 0.5) °C and melting at (69.5 ± 0.5) °C [58]. DSC traces of the material are shown in Figure 3.40 (a). DSC sample was quite small (0.6 mg), so may be it consisted of some isolated islands; this can explain the double structure of the first peak.
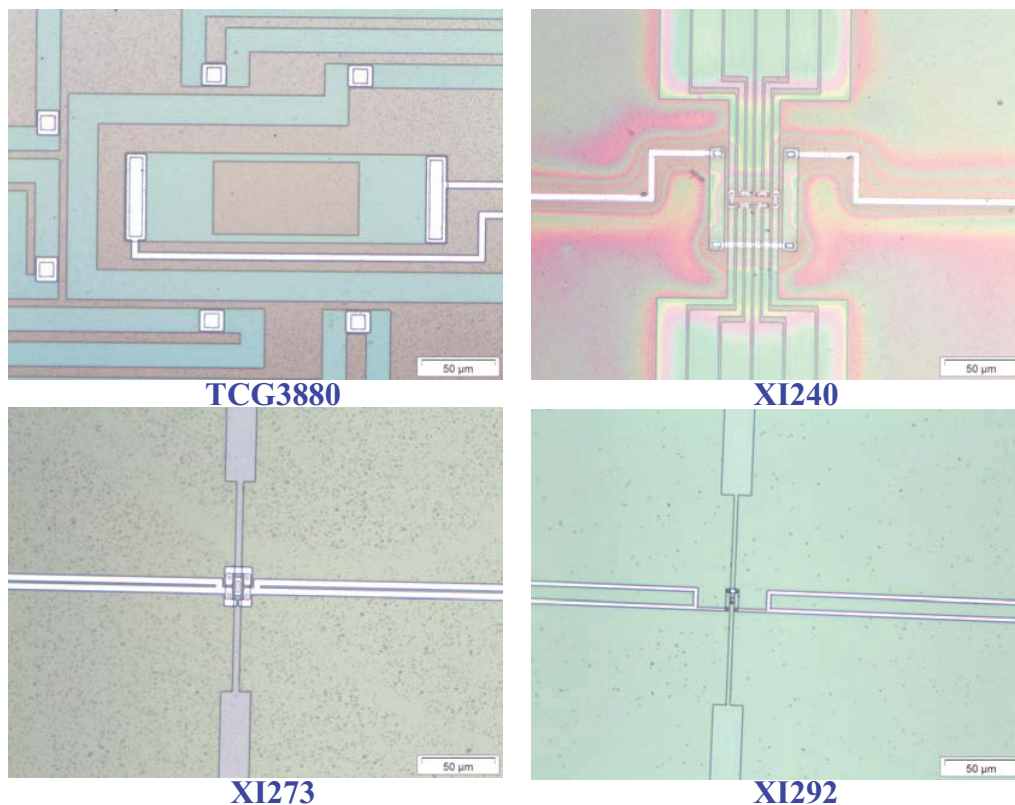
Figure 3.39: Different sensors at the same scale: TCG3880, XI240, XI273 and XI292.

The sample is not mechanically stable in the liquid state; if prepared in the usual way for the fast scanning calorimeter, it spreads over the membrane after several heating cycles. This material was measured using a copper ring as shown Figure 3.14 on page 30. On heating, there are two well-pronounced peaks (Figure 3.40 (b)).
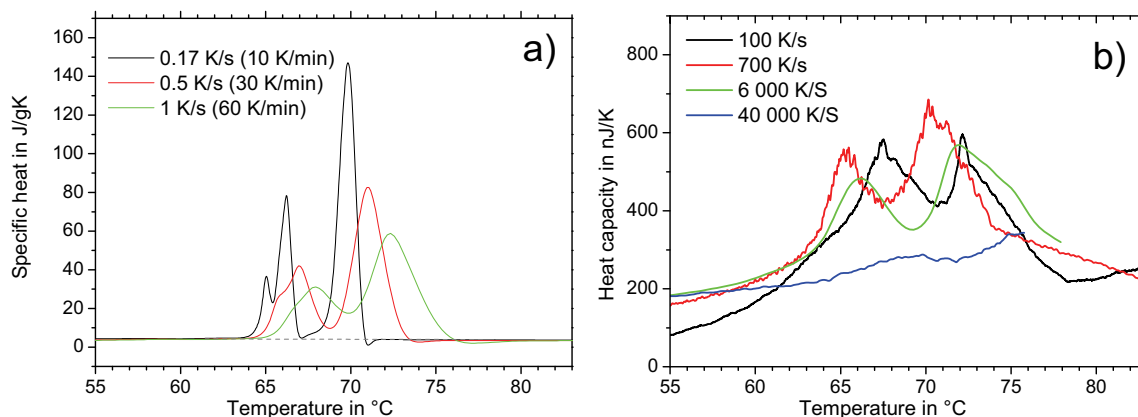
Figure 3.40: $C_{32}H_{66}$ heat capacity on heating: a) DSC; b) FSC. Each heating curve was measured after cooling from the melt at the same scanning rate. Melting conditions – FSC: 0.1 s @ 100 °C; DSC: 5 min @ 90 °C. Lowest temperature – FSC: -47.5 °C; DSC: 30 °C. Sample mass DSC 0.594 mg.

The two peaks with only 5 K in between are well separated at the heating rates of 6 000 K/s; at 40 000 K/s, the peaks are still separated but smeared; this could be caused by the copper ring. This experiment shows that the sensor is suitable for very fast measurements. Temperature resolution of about 1 K can be achieved at heating rate of about 10 000 K/s.

Even faster sensors XI273 and XI292 were used in our group for example to investigate superheating in polymers [59, 60]. The following results were obtained utilizing sensor XI240 because it has good temperature sensitivity due to six thermocouples and the heated area is still large enough to position the sample.

Chapter 4. Measurements of n-alkanes

During crystallization of a polymer material, different structures are formed depending on temperature, chain length, local conditions (fluctuations of temperature, pressure, density, chain configuration). Other processes like attaching/detaching of the parts of molecular chains may take place on the interface between the lamellae and the melt. All these processes take place simultaneously.

To build the theoretical model of the polymer crystallization process one needs an experimental data on a single occurrence of each process that takes place during the crystallization. These data are hard to get because macroscopic methods like calorimetry are able to detect only the average of all processes.

Large step forward was the invention of a method of production of very long, up to 390 C atoms in the backbone, monodisperse n-alkanes [61]. Due to exactly the same chain length and the fact that chains are relatively short (compared to polymers), similar crystals are formed in the whole sample (provided the temperature is uniform), so the signal from the whole sample is proportional to the signal from the single crystal. On the other hand, these materials show polymer-like crystallization and can be therefore used as model materials for understanding the crystallization process in polymers. This makes it possible to study the nanoscale process of polymer crystallization by calorimetric measurements on macroscale.

So far, mostly DSC equipment was used for calorimetric studies of these materials. Because of limited time resolution in the order of several ten seconds, only the high temperature slow-end tail of melt crystallization diagram was accessible. In order to extend the accessible temperature range for the crystallization studies, our fast scanning calorimeter was applied. This allowed studying kinetics of crystallization from the melt in a wide temperature range with crystallization halftimes from milliseconds to hours.

Three samples were studied: $C_{122}H_{246}$, $C_{162}H_{326}$ and $C_{390}H_{782}$. The samples were kindly provided by J. Hobbs, Sheffield, UK.

All measurements presented in this section were performed with sensors XI240 in helium at a pressure of 10 kPa. The sample was kept in the molten state for only tenth of a second, so degradation was not a serious problem and only one sample was used from each material.

4.1. Methods (temperature programs of experiments)

Crystallization parameters of the material are usually defined using one of the two strategies: crystallization on cooling at different rates (also known as Continuous Cooling Transformation -

CCT) and isothermal crystallization. CCT is closer to the praxis because many materials are crystallized on cooling during production of parts out of them. This strategy allows "fast screening" of the material, to define temperature regions interesting for isothermal crystallization study. Isothermal crystallization is rarely used for fast crystallizable materials because of difficulty to realize fast cooling followed by an abrupt change to an isotherm. However, these data are more important for theoretical description of the process because temperature is a very important parameter in the thermodynamic equations and keeping it constant during the experiment reduces the dimensionality of the problem. Our device allows both measurement modes (CCT and isothermal), so both were performed.
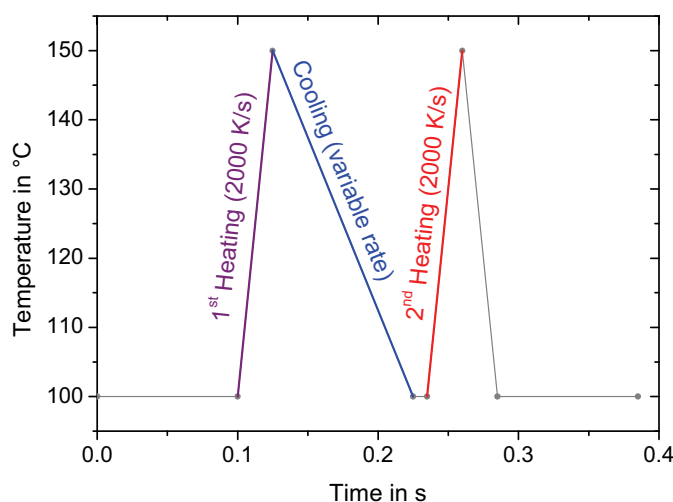
Figure 4.1: Temperature program for Continuous Cooling Transformation (CCT) study by the fast scanning calorimeter (FSC).

Typical temperature program for a **CCT study** utilizing the fast scanning calorimeter (FSC) is represented in Figure 4.1. An isotherm of 0.1 s at the beginning is used for zero drift correction (see Appendix C.2, page 115 for details). During the first heating at 2 000 K/s, the sample melts and the thermal history is erased. Then the cooling with a variable cooling rate is followed by heating (normally 2 000 K/s). Last cooling and isotherm are used to come to the oven temperature and to check zero shifts. A short isotherm of 0.01 s between cooling and heating is needed to reach the oven temperature.

Two types of **isothermal crystallization** experiments were performed. In the first method, oven temperature is kept constant; each crystallization temperature is set using the heater on the membrane (Figure 4.2 (a)). Again, the first isothermal step of 0.1 s is used for zero correction; first heating melts the sample and erases thermal history. Then the program temperature changes fast (at 10 000 K/s) to the crystallization temperature and the isothermal step follows. Crystallized sample

is then quenched to the oven temperature and heated up to the melt to check the melting peak of the structure formed during the isothermal step.

In the second method, the oven temperature is set to the desired crystallization temperature each time; crystallization occurs at the oven temperature (Figure 4.2 (b)).
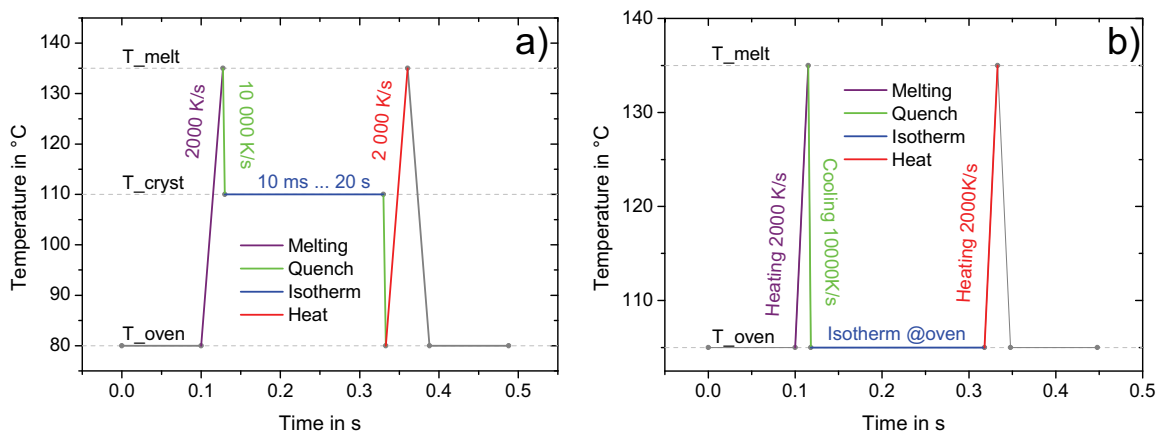
Figure 4.2: Temperature program for crystallization: a) at a temperature above oven temperature; b) at the oven temperature.

In the first method (Figure 4.2 (a)), cooling below the crystallization temperature before the melting can influence the sample in some cases, but it has an advantage that one gets the same temperature range for the heating curves allowing better comparison of the melting peaks after different crystallization temperatures. Large temperature range introduces less artificial curvature in the heat capacity curve – compare Figure 4.13 (page 74) from "crystallization above the oven temperature" and Figure 4.12 (page 74) from "crystallization at the oven temperature".

The second method (Figure 4.2 (b)) is more time consuming because after changing the oven temperature some time is needed for the temperature equilibration inside the oven. On the other hand, the sample is crystallized at the oven temperature that is measured with better accuracy using a good calibrated temperature sensor (PT-100). Additionally the amplitude of temperature change is lower; this was found to be important for mechanical stability of low molecular mass materials (see Figure 3.13).

Most isothermal crystallization experiments on n-alkanes were performed by crystallization at oven temperature according to Figure 4.2 (b).

As it was discussed in section 3.2.2 (page 18), the exact definition of the starting time (reaching the crystallization temperature) is an open question. "Crossing the peak temperature" ($\Delta T = \Delta T(max)$) or "temperature minimum before the crystallization peak" ($\Delta T = min$) as shown in Figure 3.8 (page 22) does not work for $C_{162}H_{326}$ because there is no temperature minimum before

the crystallization peak (Figure 4.9 (a) on page 71). "Approaching the oven temperature with some precision ΔT" is also not very good because the temperature minimum before the crystallization peak can be as high as 5 K above the final temperature (Figure 4.3 (a)). Therefore, this "starting time" should be defined in some "stable" way. The stable starting point is for example the start of the programmed isotherm.
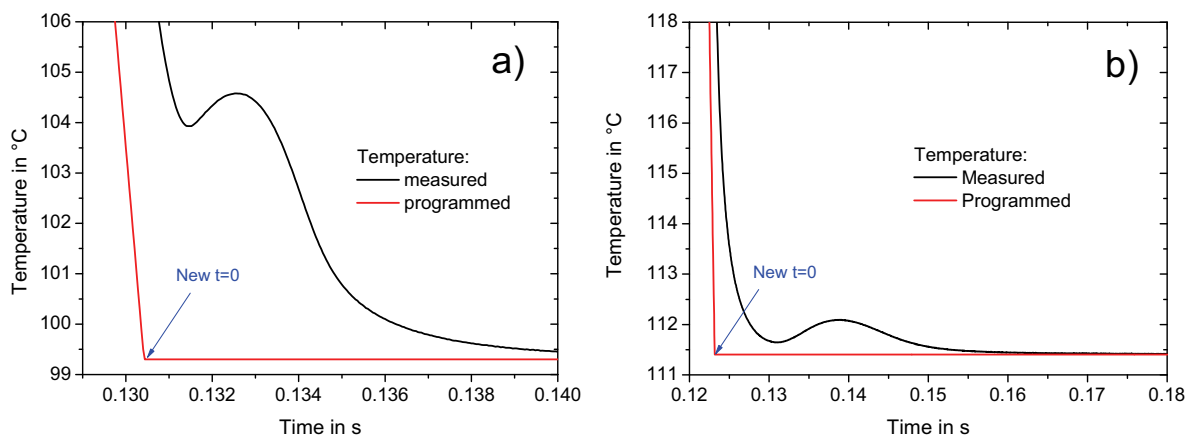
Figure 4.3: $C_{390}H_{782}$ crystallization at oven temperature of 99.3 °C (a) and 111.4 °C (b). Heating at 2 000 K/s to T_{melt} = 150 °C is followed by cooling at programmed rate of 10 000 K/s, then isotherm with the heater switched off. The lowest temperature before crystallization peak was 103.9 °C at T_0 = 99.3 °C and 111.6 °C at T_0 = 111.4 °C.

As one can see from Figure 4.3, all above definitions are close to the last one, so the beginning of the programmed isotherm is a good time reference.

High acquisition rate is needed for the fast melting step; acquisition rate cannot be changed during the experiment. As the total number of points is limited for example by the amount of the computer memory, this fact limits the duration of a single experiment. Maximum crystallization time in a single run was 20 s. For longer crystallization experiments, one can use temperature program with only one heating/cooling cycle (see Figure 3.6 on page 19) and execute it two times with a defined time in between. Crystallization peak during isotherm is obtained from the first run; the melting curve is taken from the second run. This way, the time of the recorded part of the isotherm is still limited to 20 s, but if the crystallization process takes more than several seconds, the effect becomes too small to distinguish from noise. So there is no need to record crystallization, still we get the melting curve afterwards. This technique was used for $C_{390}H_{782}$ sample.

Heating rate of 2 000 K/s was used for melting of $C_{162}H_{326}$ and $C_{390}H_{782}$ samples. $C_{122}H_{246}$ was too liquid in the molten state; so a moderate heating rate of 500 K/s was applied to prevent spreading of the sample across the membrane.

4.2. $C_{122}H_{246}$

4.2.1. Crystallization on cooling

With $C_{122}H_{246}$, there was a problem to keep the sample on the heater because of low viscosity, see Figure 3.13 on page 30. A cuvette like in Figure 3.14 (page 30) could not be used because the large additional heat capacity of the cuvette did not allow high cooling rates. That is why crystallization at different cooling rates was studied only at one oven temperature of 99.6 °C.

Cooling curves are represented in Figure 4.4 (a). The onset of crystallization was 116 °C at 200 K/s and shifted down to 103 °C at 1 000 K/s.
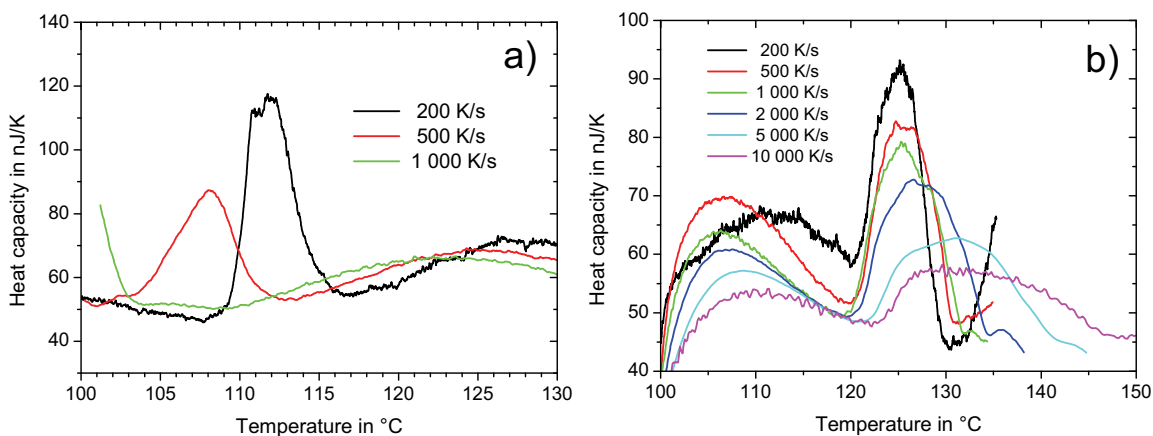
Figure 4.4: $C_{122}H_{246}$: a) crystallization on cooling; b) melting. T_0=99.6 °C, He @ 10 kPa. Melting: heating to 135 °C and switch immediately to cooling without isotherm. The same scanning rate was used for melting, cooling and the following heating.

In melting (Figure 4.4 (b)) there is no rate dependence of the onset of melting up to 2 000 K/s. The reasons for the high temperature shoulder for rates of 500 K/s and higher are not yet known, but it could be due to a change of the sample position and shape.

4.2.2. Isothermal crystallization at different temperatures

Isothermal crystallization was performed at oven temperature according to temperature program in Figure 4.2 (b); crystallization curves are presented in Figure 4.5. For lowest oven temperatures (up to 101.9 °C) there is a single crystallization peak. At 102.9 °C a second shoulder appears (Figure 4.5 b). It is present for temperatures up to 105.8 °C, then starting from 106.8 °C there is again a single peak.

Crystallization halftime versus crystallization temperature is presented in Figure 4.6. As one can see in Figure 4.5, at lowest oven temperatures crystallization mostly occurs during cooling, before

the oven temperature was reached. Therefore, the lowest measured temperature before the crystallization peak was used as crystallization temperature in Figure 4.6.
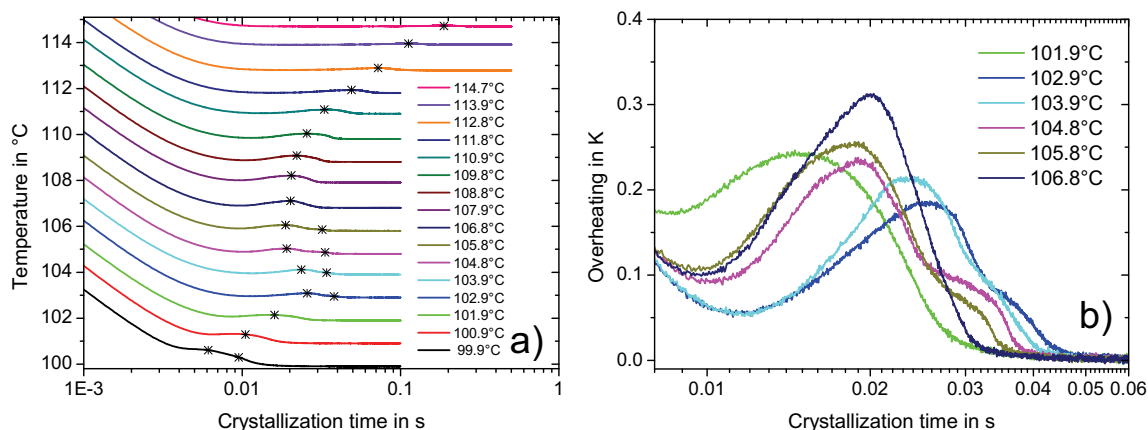
Figure 4.5: Isothermal crystallization of $C_{122}H_{246}$ at different temperatures: a) oven temperatures 99.9 °C to 114.7 °C (sample temperature versus time); b) enlarged double crystallization peak inside the region 101.9…106.8 °C (overheating versus time). Time zero was defined as the beginning of the programmed isotherm; the actual crystallization temperature within 1 K was reached 3…4 ms later. Surrounding: He @ 10 kPa. Melting @150 °C without isotherm; programmed heating rate 500 K/s, cooling rate 10 000 K/s.
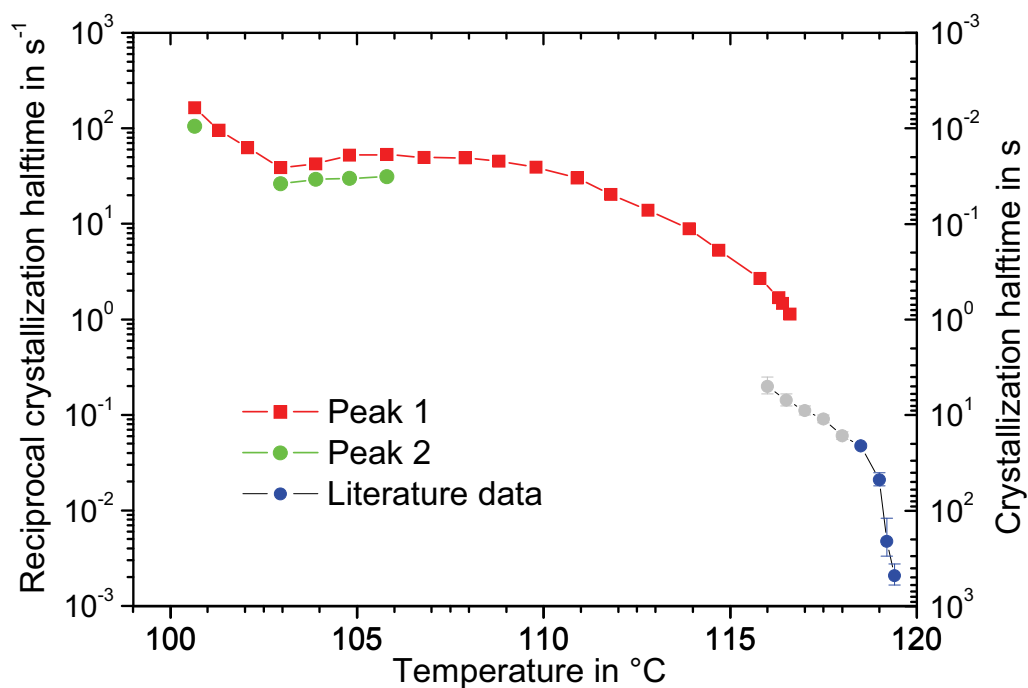
Figure 4.6: $C_{122}H_{246}$ crystallization halftime: data from Figure 4.5 as well as literature data [62]. Literature data shorter than 20 s are marked gray because of time constant of 10 s of the DSC instrument. For FSC results, the crystallization temperature is defined as the lowest sample temperature before the crystallization peak.

One can see a bend at about 103 °C; such behavior was already seen for longer chain materials – $C_{246}H_{494}$ [63, 64], $C_{294}H_{590}$ [65], $C_{168}H_{338}$, $C_{192}H_{386}$ and $C_{240}H_{482}$ [66]. This discontinuity was connected to the change of the integer value of chain folding. As to our knowledge, at this temperature and time scale this process was never observed before.

In Figure 4.6 the data obtained are compared with already published for this material [62]. Although the literature data (it is called "crystallization time") is different from the "crystallization peak time" defined here, the trend can be compared. It is worth to mention that DSC2 device used by Hosier and Bassett had a time constant of at least 10 s, so points faster then 20 s could be shifted. Nevertheless, data of Hosier and Bassett with crystallization times of 20 s and slower (blue points in Figure 4.6) give together with our measurements a smooth curve in the region from 103 to 119 °C.

Melting temperature could not be determined since it was not reproducible due to instability of the sample position, see Figure 3.13 on page 30.

4.3. $C_{162}H_{326}$

4.3.1. Crystallization on cooling
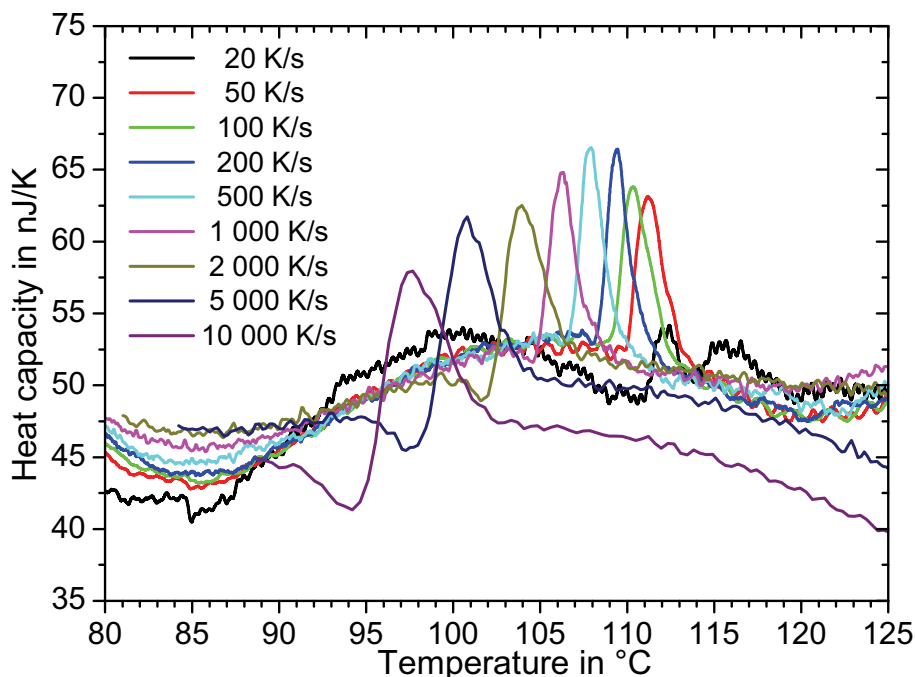
Figure 4.7: $C_{162}H_{326}$ **crystallization on cooling. T_0=80 °C. Surrounding: He @ 10 kPa. Melting conditions: heating to 135 °C @2 000 K/s and switch to cooling without isotherm.**

$C_{162}H_{326}$ at cooling rates above 50 K/s shows a continuous shift of the crystallization peak towards lower temperatures with increasing cooling rate (Figure 4.7). Even though signal to noise

ratio is bad at 20 K/s and lower, double crystallization peaks are seen at these rates at temperatures between 110 and 117 °C. Cooling rates down to 5 K/s were measured, but only 20 K/s is presented because of data quality.

In the melting curves (Figure 4.8) this phenomenon is clearly pronounced: structure formed at a cooling rate of 5 K/s starts to melt at 125 °C; after cooling at rate above 20 K/s the material shows two melting peaks at about 115 °C and 125 °C. With increasing cooling rate during crystallization, the area under the lower melting peak increases and the upper peak almost disappears after cooling at 50 K/s. This supports earlier investigations about different crystal structures formed in these oligomers depending on crystallization conditions.
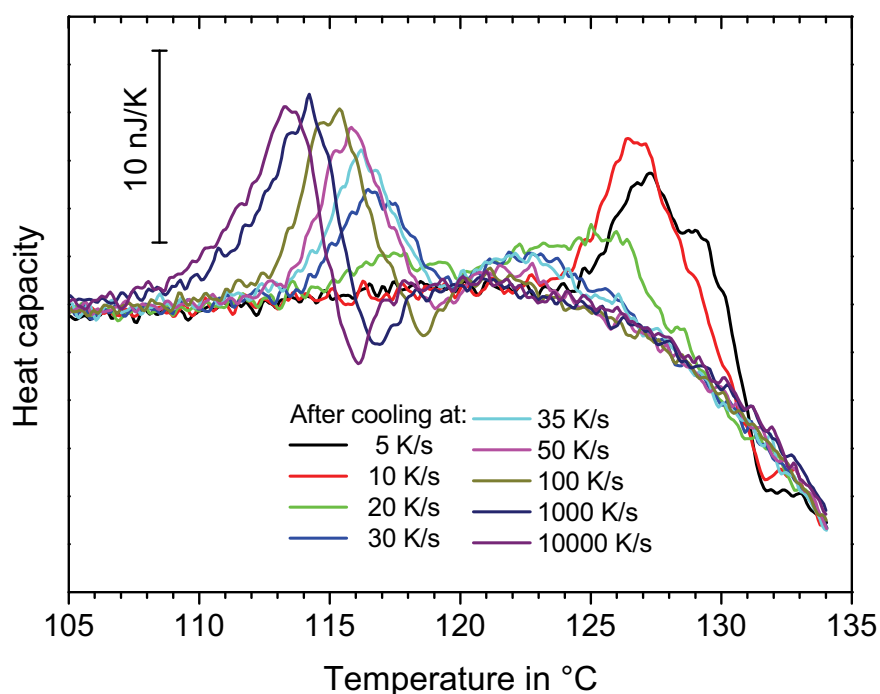
Figure 4.8: C$_{162}$H$_{326}$ heating at 2 000 K/s; preceding cooling rate is indicated in the legend. Decrease of apparent heat capacity above 122 °C is an instrumental artifact. For experimental conditions see the caption to Figure 4.7.

A melting peak at 126-127 °C corresponds to the extended chain crystal structure reported by Hosier and Bassett [62]. With increasing cooling rate, the amount of the thermodynamically preferable extended chain crystals decreases and a once folded structure appears, because it is kinetically preferred at lower temperatures.

At higher cooling rates (above 50 K/s), only a once folded crystal structure with melting temperature of about 115 °C is formed. This means the sample passes the high temperature region fast enough to prevent formation of the more stable extended chain phase during cooling.

With further increase of cooling rate, there is a dramatic shift of the crystallization peak to lower temperatures, but the melting peak does not shift significantly. This indicates that once folded structures are formed at cooling rates up to 10 000 K/s and this material does not show stable double folded structures at such cooling rates. If double folded structures are formed, they may recrystallize at heating at 2000 K/s without detectable heat effect yielding the single melting peak at about 115 °C that corresponds to the once folded structure.

4.3.2. Isothermal crystallization at different temperatures

Isothermal crystallization of $C_{162}H_{326}$ at oven temperature was performed as well. Crystallization curves are shown in Figure 4.9 (a), corresponding melting at 2 000 K/s in Figure 4.11.
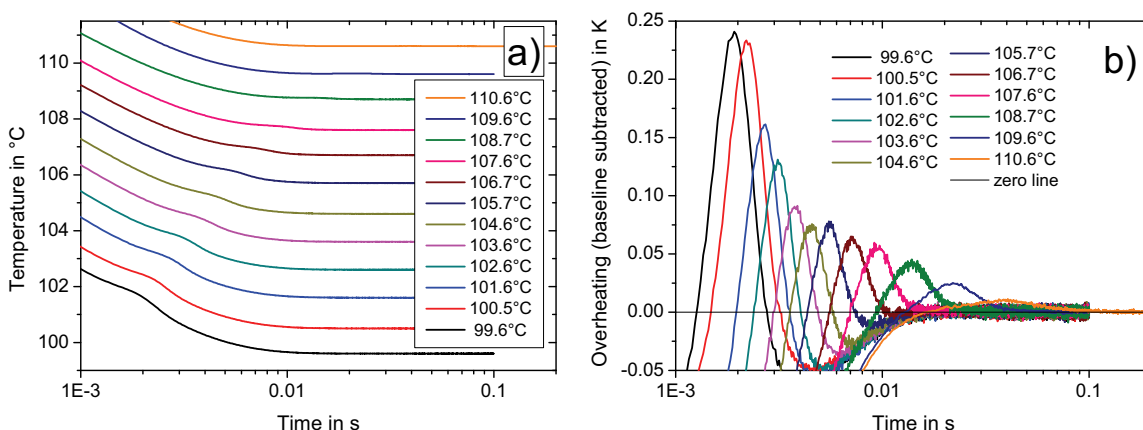
Figure 4.9: $C_{162}H_{326}$ crystallization – overheating versus time: a) original curves; b) after baseline subtraction. Oven temperatures are indicated in the legend; programmed cooling rate 10^4 K/s. Surrounding: He @ 10 kPa. Melting conditions: heating to 130 °C @2 000 K/s and switch to cooling without isotherm.

It is hard to say, where the crystallization peak is. That is why a "base line" was subtracted from the measured temperature. This "base line" had to be a quite similar measurement, but without any exo- or endothermic process inside the sample. One possibility is to reduce the temperature so that the sample will remain crystalline during the heating-cooling cycle. The highest melting onset temperature observed (Figure 4.11) was 123.6 °C. So if we crystallize the sample into that phase and then "cycle" the temperature between 80 °C and 120 °C there should be neither crystallization nor melting. The "base line" was measured at oven temperature of 80 °C in the sample temperature range of 80 to 120 °C. The lower-temperature melting peak at 110…115 °C was present during the first heating, but it disappeared after several cycles and the sample remained crystalline. Overheating versus time curve after base line subtraction shows clearly a crystallization peak

(Figure 4.9 (b)). This peak appeared before reaching of the oven temperature; there was even no temperature minimum before the peak (Figure 4.9 (a)). Therefore, the "crystallization temperature" was defined as sample temperature at the time of the maximum in the subtracted curve.

Crystallization kinetics is shown in Figure 4.10. The data from Hosier and Bassett [62] are shown for comparison; they correspond to extended chain crystal structure.

Figure 4.10: C$_{162}$H$_{326}$ crystallization rate extracted from the data presented in Figure 4.9. DSC: Pyris 1 (Perkin Elmer), sample mass 0.246 mg. Literature data are taken from [62]. The sample thickness dependence and surface effects can cause difference in DSC data. Hosier and Bassett observed structures of up to 0.7 mm size; our sample thickness was below 0.1 mm.

To draw a conclusion about crystal structures formed during crystallization, melting curves at 2 000 K/s after each crystallization were evaluated (Figure 4.11). After crystallization at high temperatures (above 111 °C), there is a melting peak at 126 °C (peak 3 in Figure 4.11). After crystallization at 110.6 °C, this peak is smaller; after crystallization at 109.6 °C and below, it is not present. Another large melting peak (peak 1 in Figure 4.11) is seen at about 114 °C after crystallization at temperatures below 109 °C. An additional small melting peak (peak 2 in Figure 4.11) was seen in the temperature range of 121 to 124 °C.
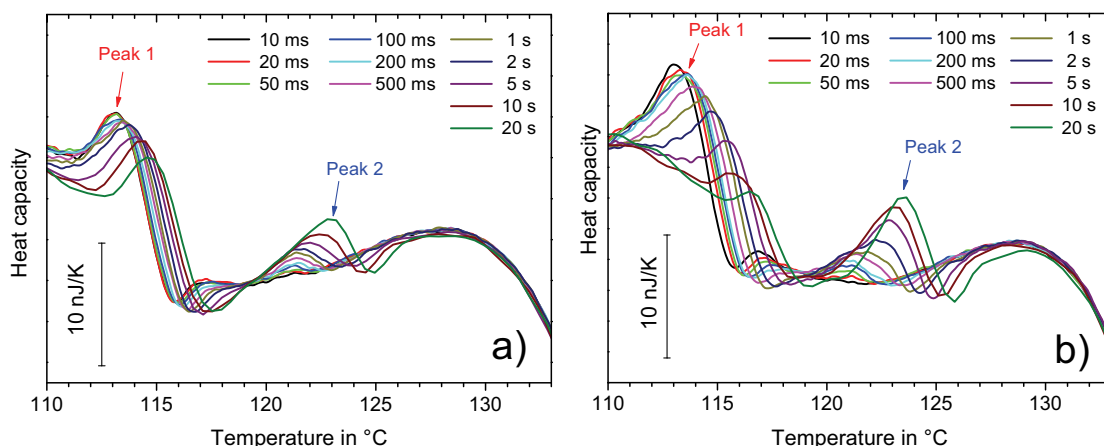
Figure 4.11: $C_{162}H_{326}$ melting after isothermal crystallization at different oven temperatures (for crystallization temperatures see Figure 4.9). Heating rate 2 000 K/s. A band at 116 °C as well as a negative slope below this temperature is an instrumental artifact caused by small scanning range.

We have expected formation of two structures (extended chain and once folded), however three separated melting peaks were observed. To investigate the origin of such behavior, different crystallization times at the same temperature were studied.

4.3.3. Melting peak versus crystallization time

Melting curves for crystallization temperatures of 100, 105 and 110 °C are shown in Figure 4.12 and Figure 4.13. There are two melting peaks after all three crystallization temperatures. After crystallization at 100 °C (Figure 4.12 (a)), only the first melting peak (with a maximum at 113 °C) is pronounced after a short crystallization time. Starting from crystallization time of about 100 ms, the second melting peak (onset about 120 °C) becomes noticeable. With increase of crystallization time, the first melting peak decreases and its onset temperature increases; the second melting peak increases with its onset temperature remaining constant. No saturation is observed up to crystallization times of 20 s.

Similar behavior is observed at 105 °C crystallization temperature. After 20 s crystallization, the first melting peak is already much smaller than the second one.

Figure 4.12: $C_{162}H_{326}$ **melting @ 2 000 K/s after isothermal crystallization at oven temperature of: a) 100 °C; b) 105 °C. Surrounding: He @ 10 kPa. Melting conditions: heating to 135 °C @2 000 K/s followed by cooling @ 10 000 K/s without isotherm. A band at 116 °C as well as a negative slope below this temperature is an instrumental artifact caused by small scanning range.**
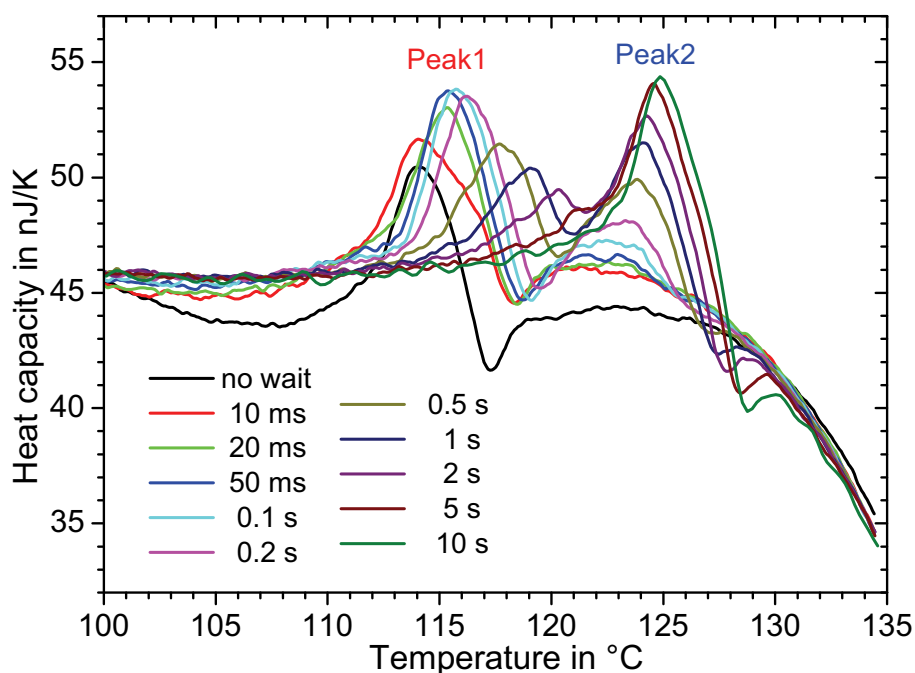
Figure 4.13: $C_{162}H_{326}$ **melting @ 2 000 K/s after isothermal crystallization at 110 °C (T_0=78.9 °C); temperature program see Figure 4.2 (a) Melting temperature 135 °C. "No wait" corresponds to quench directly to the oven temperature at programmed cooling rate of 10 000 K/s.**

For 110 °C crystallization temperature (Figure 4.13), the first melting peak increases with increasing crystallization time and saturates at crystallization time of about 50 ms. This corresponds quite good to the crystallization halftime of 27 ms from Figure 4.10. With increasing crystallization time above 0.2 s, the first melting peak decreases and the second one appears in the temperature

range 122…125 °C. With increasing crystallization time, the first melting peak further decreases in magnitude and shifts to higher temperatures. After 10 s crystallization, the first melting peak is no longer detectable.

For experiments in Figure 4.11, the crystallization time was chosen so that crystallization peak is finished before the melting scan. The time was 100 ms at temperatures 109.6 °C and below, 200 ms at 110.6 °C, 2 s at 111.6 °C and 112.6 °C. This means peak 2 in Figure 4.11 continuously transforms in peak 3 with increasing of annealing time at crystallization temperature as one can see on evolution of peak 2 in Figure 4.13; both peaks correspond to the melting of similar crystal structure.

At all three temperatures, one structure is formed at the beginning (it melts in peak 1) and then it transforms to another one that melts in peak 2 or peak 3.

4.4. $C_{390}H_{782}$

4.4.1. Crystallization on cooling
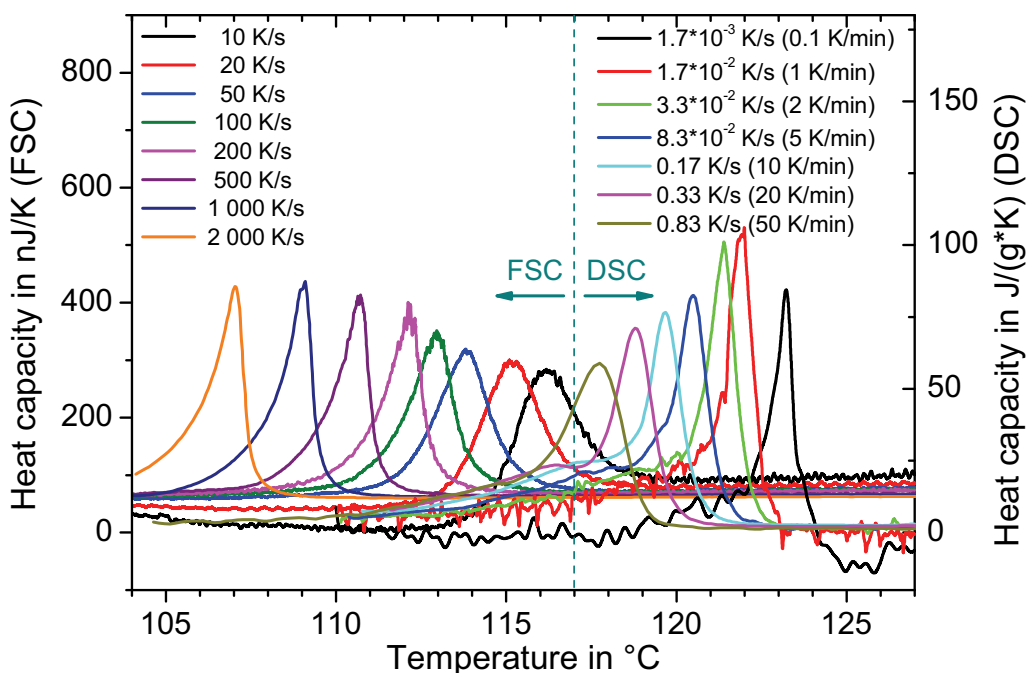
Figure 4.14: $C_{390}H_{782}$: crystallization on cooling at rate indicated. Peaks to the left from the dashed line: fast scanning calorimeter (total heat capacity), to the right – Pyris 1 DSC (specific heat). Experimental conditions – FSC: sample mass about 10 ng; T_0=99.3 °C; surrounding: helium 10 kPa; melting: heat to 150 °C @ 2 000 K/s and switch to cooling without isotherm. DSC: sample mass 74 μg; melting: heat to 140 °C @ 0.17 K/s (10 K/min), isotherm 180 s.

With the longest n-alkane measured ($C_{390}H_{782}$), no anomalies were seen in the heat capacity curves during crystallization on cooling at different rates (Figure 4.14). Crystallization peak shifts continuously to lower temperatures with increasing cooling rate. After each cooling run, the sample was heated up with the same heating rate (Figure 4.15).
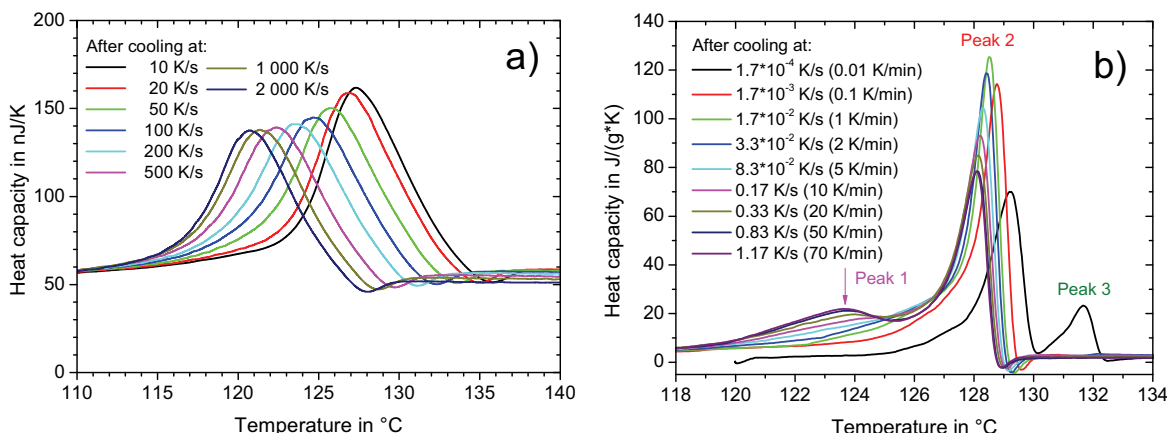
Figure 4.15: $C_{390}H_{782}$ heating scans after cooling with different rates: a) FSC; b) Pyris DSC. Preceding cooling rates are indicated in the legend. Heating rate: FSC: 2 000 K/s; DSC: 0.17 K/s (10 K/min). For experimental conditions, see caption of Figure 4.14.

In the heating curves from the fast scanning calorimeter (Figure 4.15 (a), 2 000 K/s) there is a continuous shift of the melting peak from 120 to 127 °C for cooling rates from 10 to 2 000 K/s. In the DSC experiments (Figure 4.15 (b), 0.17 K/s), there are three peaks: peak 1 at 123-124 °C, peak 2 at 128-129 °C and peak 3 at about 132 °C.

4.4.2. Isothermal crystallization at different temperatures
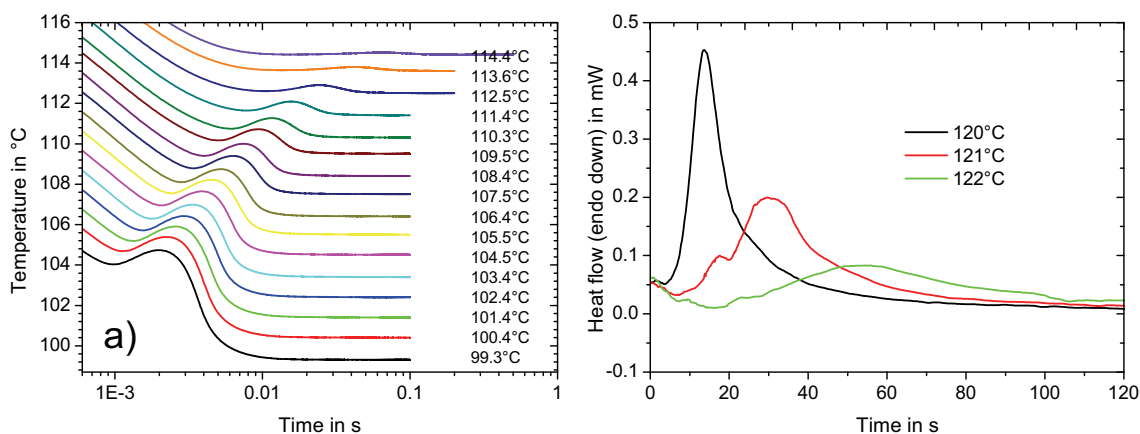
Figure 4.16: $C_{390}H_{782}$ isothermal crystallization: a) FSC; b) Pyris DSC. Experimental conditions – FSC: sample mass about 10 ng; oven temperature is indicated in the legend; melting: heat to 150 °C @ 2 000 K/s and switch to cooling @ 10 000 K/s without isotherm; surrounding: helium at 10 kPa. DSC: sample mass 74 µg, melting: heat to 140 °C @ 0.17 K/s (10 K/min), isotherm 180 s, cooling @ 0.67 K/s (40 K/min), the last 0.6 K are done slow in several steps.

Isothermal crystallization curves for $C_{390}H_{782}$ at different temperatures are presented in Figure 4.16. With increasing the oven temperature, crystallization peak shifts continuously to longer times and its amplitude decreases. At temperatures below 112 °C, most of crystallization occurs during cooling when the temperature is still above oven temperature. At the lowest oven temperature, this difference is more than 5 K. Therefore, the lowest temperature before the crystallization peak was used as crystallization temperature in the following study.

The overall crystallization rate is shown in Figure 4.17. Additionally to Pyris DSC, a Mettler Toledo DSC-822 calorimeter was used for long (up to ten hours) crystallization halftimes.
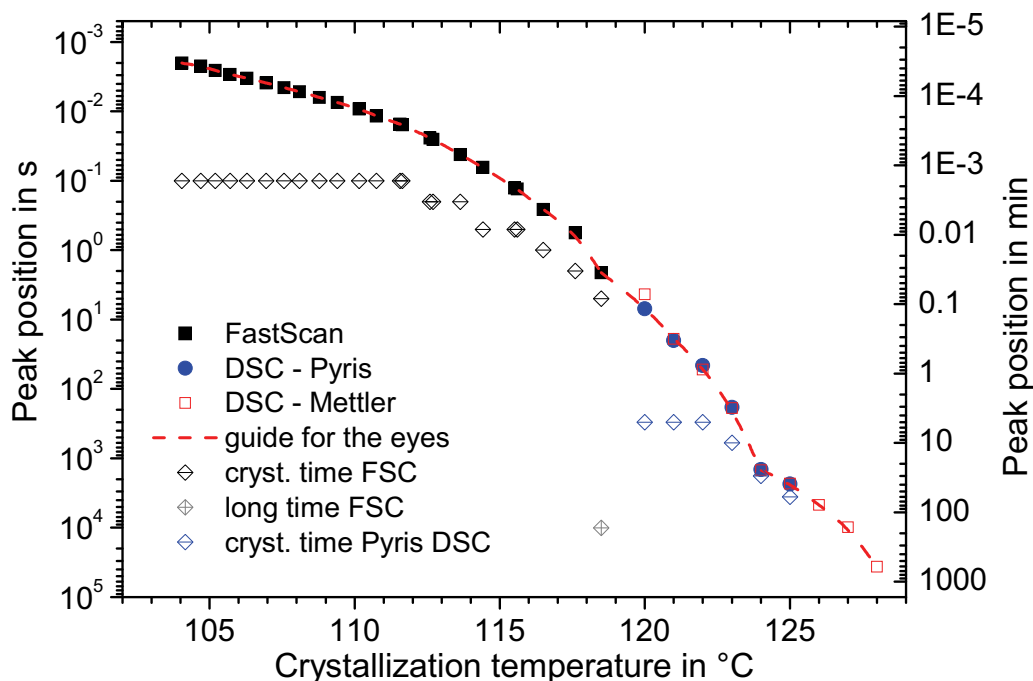
Figure 4.17: $C_{390}H_{782}$ crystallization rate. Experimental details see Figure 4.16. DSC Mettler: Toledo DSC-822, sample mass 0.42 mg. Open diamonds indicate total duration of the crystallization isotherm during the measurement.

As lower molecular mass materials, this sample shows a discontinuity in the slope. For this sample, the bend is at 124 °C. Another bend at 119 °C is less pronounced; still there is some structure change at this temperature, as it will be discussed later.

After each crystallization experiment, the sample was heated up to the melt at the same heating rate. Melting curves are presented in Figure 4.18. With changing the crystallization temperature from 99.3 to 115.5 °C, melting peak shifts continuously to higher temperatures without changing its height.
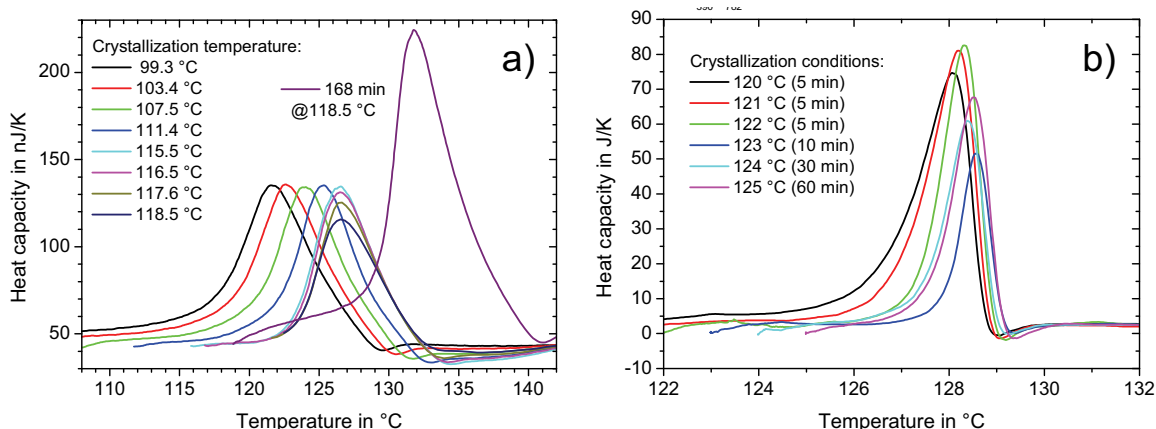
Figure 4.18: C$_{390}$H$_{782}$ **melting after isothermal crystallization shown in Figure 4.16: a) FSC, heating rate 2 000 K/s; b) Pyris DSC, heating rate 0.17 K/s (10 K/min). Crystallization temperature is indicated in the legend; crystallization time is represented by diamonds in Figure 4.17. Sample mass FSC about 10 ng, DSC 74 μg.**

With further increase of crystallization temperature from 115.5 °C up to 118.5 °C, the melting peak at about 126 °C becomes smaller without changing its temperature. Apparently, decrease of the crystallization rate with increase of the crystallization temperature was not compensated by the increase of the crystallization time that is indicated by diamonds in Figure 4.17. However, if one waits longer (e.g. 168 min at 118.5 °C, crossed diamond in Figure 4.17), then the melting peak becomes larger (which means higher crystallinity) and shifts to higher temperature (peak at 131.8 °C, see Figure 4.18 (a)). In DSC experiments (Figure 4.18 (b), Figure 4.19 (a)), crystallization at temperatures between 120 °C and 125 °C resulted in melting peaks at 128 to 128.5 °C.
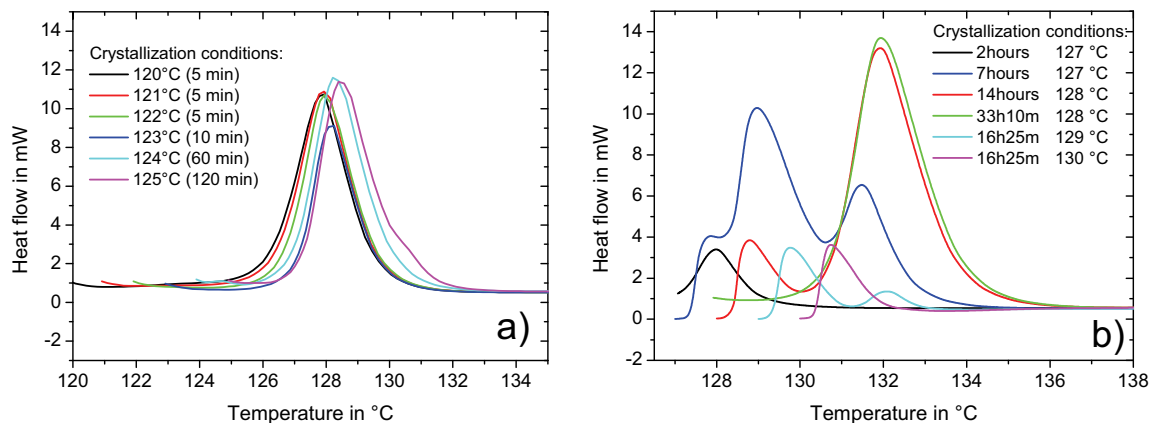
Figure 4.19: C$_{390}$H$_{782}$ **melting after different crystallization. Calorimeter: Mettler Toledo DSC-822. Experimental conditions: heating rate 0.17 K/s (10 K/min); melting: heat to 140 °C @ 0.17 K/s (10 K/min), isotherm 60 s, cool down to the crystallization temperature @ 0.17 K/s (10 K/min). Sample mass 0.42 mg.**

In the results presented in Figure 4.19 (a), the sample was crystallized at 124 and 125 °C longer then at other temperatures and this led to a melting peak even higher than that after crystallization at 120 and 121 °C. Therefore, reduction of the peak height after higher crystallization temperatures in Figure 4.18 (b) was caused by reduced effective crystallization time and not by lower maximum possible crystallinity at higher crystallization temperature.

At 127 °C (crystallization peak time 2.7 hours), a structure with a melting peak temperature of 128 °C is formed after 2 hours; after 7 hours, it is already transformed into a quite complicated structure with a triple melting peak (Figure 4.19 (b)). After 14 hours at 128 °C (crystallization peak time 10 hours), there is a small melting peak at 129 °C and a large melting peak at 132 °C. After 33 hours, only the 132 °C melting peak is present.

After 16.5 hours of crystallization at 129 °C, there is a small melting peak at 132 °C and a larger melting peak at 130 °C. Only the lower melting at 130.7 °C is visible after 16.5 hours crystallization at 130 °C; there may be a shoulder at 132 °C.
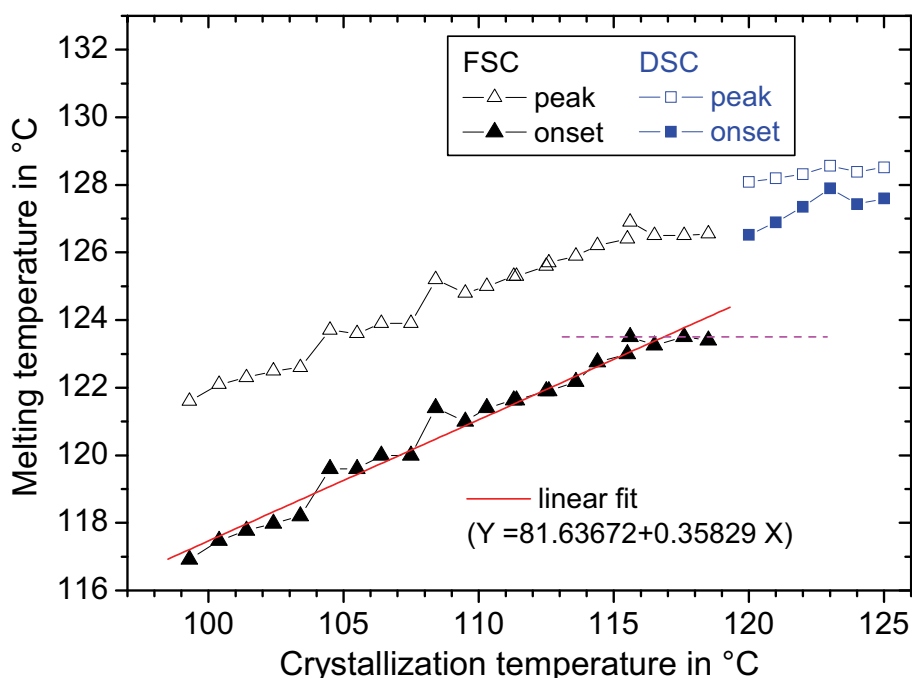
Figure 4.20: **C$_{390}$H$_{782}$ melting temperature versus crystallization temperature. Black triangles represent data from FSC (heating rate 2 000 K/s), blue squares are from DSC (heating rate 0.17 K/s or 10 K/min); solid points represent onset and empty ones – peak temperature.**
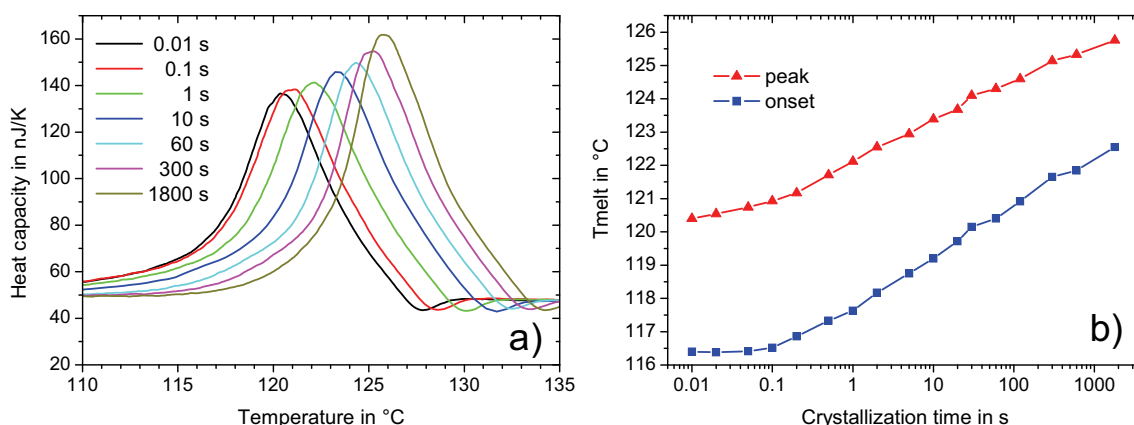
Melting temperature (onset and peak value of the first peak) versus crystallization temperature is presented in Figure 4.20. For FSC results, the melting temperature depends on the crystallization temperature almost linearly with a slope of 0.36, which is quite different from a value of one as observed for PCL, sPP and some other polymers.

Data from DSC shows similar dependence, however, the DSC points are shifted towards higher melting temperatures. Most probably, it is again because the isotherm in DSC (at least 5 min) was much longer than that in fast scanning instrument (at most 5 s). To find the reason of such difference, crystallization time dependence was studied.

4.4.3. Melting peak versus crystallization time

Annealing time dependence at the crystallization temperature was studied for the $C_{390}H_{782}$ at temperatures of 99.3 °C, 119.3 °C and 125 °C.

With increasing annealing time at 99.3 °C melting peak shifts continuously to higher temperatures (Figure 4.21 (a)). The area under the melting peak does not change significantly with increase of the crystallization time and peak shifts continuously to higher temperatures.

Figure 4.21: $C_{390}H_{782}$ crystallized at T_0=99.3 °C: a) melting curves; b) melting temperature versus crystallization time. Temperature program is shown in Figure 4.2 (b). Both heating rates (erasing thermal history and after crystallization) 2 000 K/s, T_melt = 150 °C, first cooling rate 10 000 K/s. There are no isotherms at the highest temperature. The lowest temperature before crystallization peak (cooling curve see Figure 4.16 (a)) was about 104 °C.

Melting temperature (onset and peak values) versus crystallization time is presented in Figure 4.21 (b). Even after 1800 s, the process continues and is far from saturation.

Melting behavior after crystallization at 119.3 °C is more complicated (Figure 4.22). No melting peak was detected after crystallization time between 10 ms and 200 ms; after 0.5 s, a peak at 127 °C appears. Its amplitude increases with increasing crystallization time up to 10 s; then the peak shifts rapidly to the next melting temperature of 131-132.5 °C.

Melting peak temperature and evolution of peak height versus crystallization time is shown in Figure 4.23 (a) and (b) respectively.
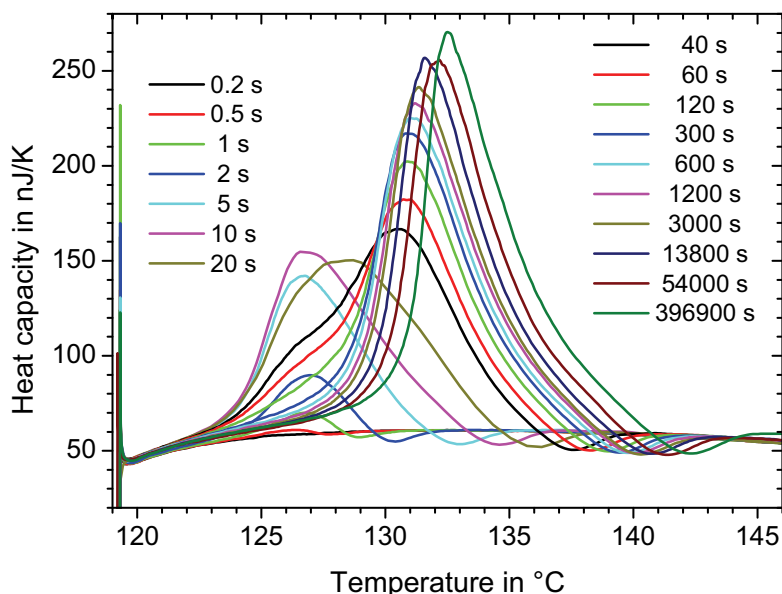
Figure 4.22: Melting curves of C$_{390}$H$_{782}$ crystallized at 119.3 °C for different time. For temperature program see Figure 4.2 (b). Both heating rates 2 000 K/s, first cooling rate 10 000 K/s, T_melt = 150 °C; no isotherms at the T_melt.
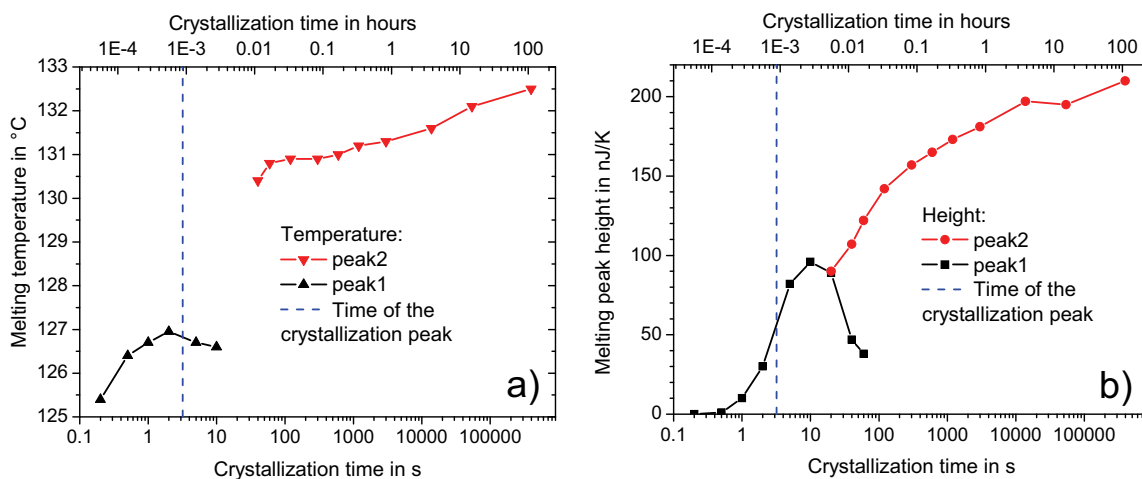
Figure 4.23: C$_{390}$H$_{782}$ crystallized at 119.3 °C for different time: a) melting temperature (peak value) versus crystallization time; b) melting peak height versus crystallization time. Time of the crystallization peak (see Figure 4.17) is labeled with a blue dash line.

Starting from crystallization time of 0.5 s, structure 1 (corresponding melting peak 1) appears; its melting peak increases and reaches its maximum at 10 s. This corresponds to the dynamics of heat release during crystallization: time of maximum in crystallization (dashed line in Figure 4.23) coincides with the maximum slope of the melting peak height versus crystallization time. After 20 s, amount of structure 1 decreases and structure 2 appears; after 100 s, melting peak of structure 1 is not detectable and amount of structure 2 increases.
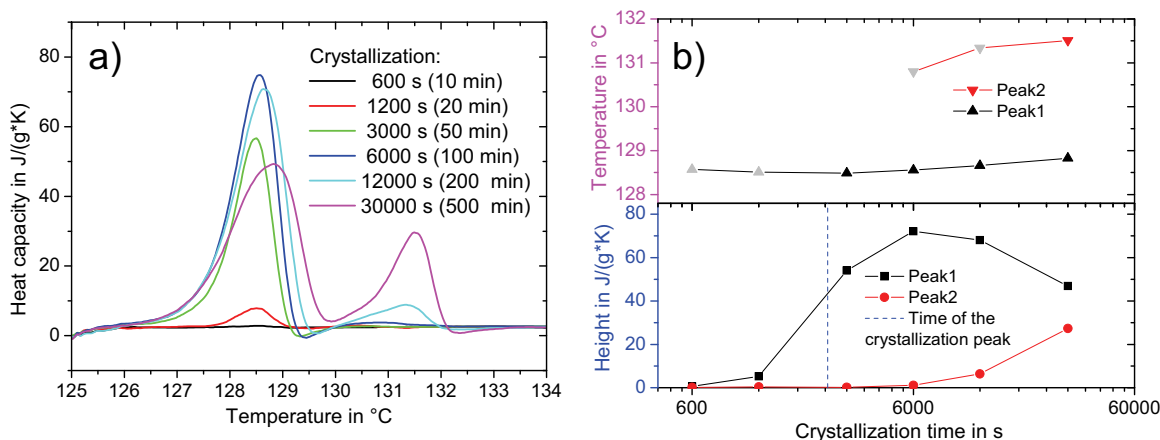
Figure 4.24: $C_{390}H_{782}$ **melting after different crystallization time @ 125 °C (Pyris DSC): a) melting curves; b) melting temperature and melting peak height versus crystallization time. Crystallization peak time from Figure 4.17 is labeled with a blue dash line. Gray color of the temperature peak points an attention to a reduced peak height. Melting conditions: heat to 140 °C @ 0.17 K/s (10 K/min); isotherm 180 s; cool down to 126 °C @ 0.33 K/s (20 K/min); then slower cooling in 3 steps downto 125 °C. Heating rate 0.17 K/s (10 K/min).**

Similar measurements for crystallization temperature of 125 °C were performed in Pyris 1 DSC (Figure 4.24 (a)). There is no melting peak after a short time (at this temperature, it is 10 minutes); after 20 minutes the peak at 128.5 °C appears; peak temperature remains nearly constant with further increase of the crystallization time. After 200 minutes, a second melting peak at 131-131.5 °C appears. With increasing the crystallization time, the second peak increases and the first peak decreases.

Peak temperatures and heights are shown in Figure 4.24 (b). As in the previous experiment, time of the maximum heat production during crystallization (blue dashed line in Figure 4.24 (b)) corresponds to the maximum in the slope of the height of the first melting peak, so heat production measured during crystallization was caused by creation of the structure that melts in peak 1.

4.5. Discussion

4.5.1. CCT results of $C_{390}H_{782}$

The $C_{390}H_{782}$ sample was molten, crystallized at different cooling rates and again molten at the same heating rate for all experiments. The crystallization and corresponding melting temperatures as a function of cooling rate during the crystallization step are collected together in Figure 4.25.

In the **crystallization** curves, there is an apparent shift of 1–2 K between results from DSC and from fast scanning calorimeter. It can be due to a difference in temperature calibration of both instruments: DSC was calibrated on heating; because of symmetry arguments, this calibration was

used for cooling experiments. However, calibration on cooling can be different as discussed in [67, 68]. On the other hand, fast scan calibration has an absolute error of at least ±1 K; see section 3.5. In addition, a different surface under the sample could affect crystallization. The DSC sample was enclosed into aluminum foil; the fast scan sample was located on the deposited SiO_2 film. Nevertheless, the crystallization curves measured with different instruments match each other in Figure 4.25 very well. Crystallization temperature shifts continuously to lower temperatures with increasing cooling rate.
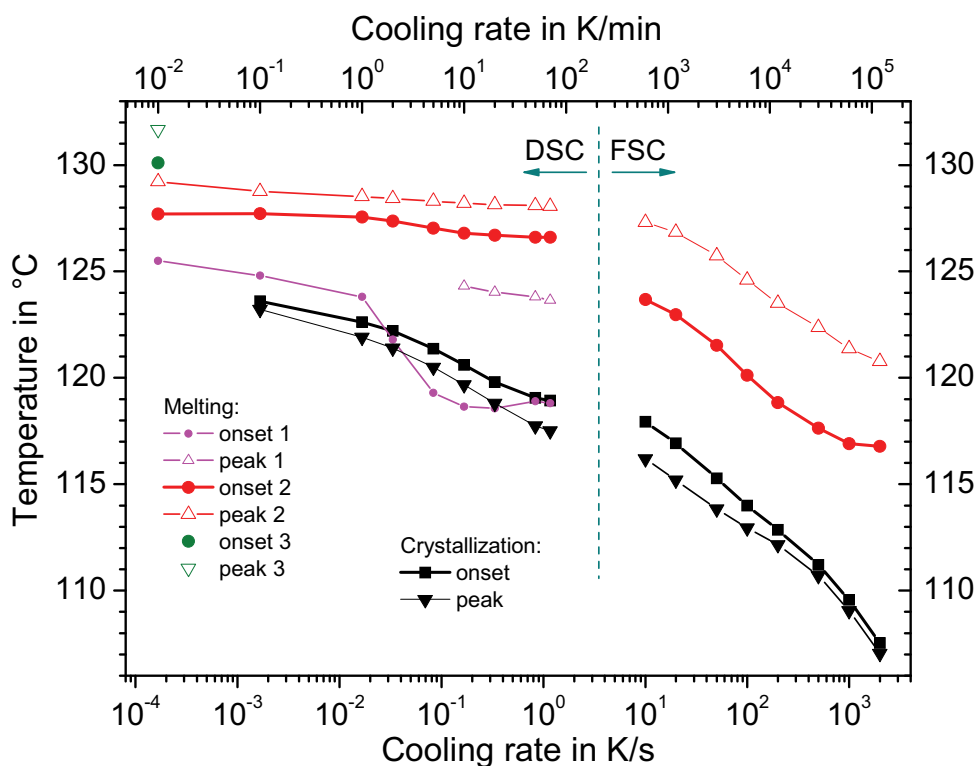
Figure 4.25: $C_{390}H_{782}$ cooling rate dependence. Cooling curves at a given cooling rate are shown in Figure 4.14, heating curves at 2 000 K/s (FSC) and 0.17 K/s (DSC) are in Figure 4.15.

First **melting** peak of the DSC sample (Figure 4.25) starts sometimes at temperature below the crystallization temperature. This means it cannot correspond to the "main" crystallization. In all DSC experiments, between the cooling and the heating, there was a 5 min isotherm at 120 °C (0.01 K/min), 110 °C (0.1 to 5 K/min), 100 °C (50 K/min) and 50 °C (70 K/min) for instrument stabilization. Most probably, this structure was formed during this isotherm. In the fast scanning results, there is no such melting peak; there was only a 0.01 s isotherm at the oven temperature of 99.3 °C. The second melting peak in the DSC curves continues in the fast scan measurements.

As reported earlier, the cooling rate of $8.3*10^{-3}$ K/s (0.5 K/min) produces once-folded crystal structure ("folded in two", *F2*) [69]. In our experiments, the next higher and lower cooling rates

$(1.7*10^{-2}$ K/s (1 K/min) and $1.7*10^{-3}$ K/s (0.1 K/min)) produce structures with similar melting curves (see Figure 4.15 (b)). In both curves, only the second melting peak is well pronounced, so this is melting of once folded structure. The melting temperature (peak value) is 128.5 °C.

The third peak at 131.6 °C was present only after the slowest cooling at $1.7*10^{-4}$ K/s (0.01 K/min). It is in a good agreement with the melting temperature of the extended chain structure (**E**) of 132 °C [69].

In DSC, the melting temperature is relatively rate-independent and it shows significant rate dependence only at higher cooling rates (fast scan). According to Ungar and Zeng [70], a so-called non-integer form (**NIF**) can be formed first; then it changes to the more stable integer form. **NIF** was transformed to the once-folded form on cooling and during the 5 minutes isotherm in DSC; therefore, the melting peak is almost the same for all DSC cooling rates. In the fast scan instrument, the isotherm at lowest temperature was only 10 milliseconds and there was not enough time to build an integer form. As a result, there is a continuous decrease of melting temperature with increasing cooling rate.

4.5.2. Isothermal crystallization

For all three samples, isothermal crystallization halftime versus crystallization temperature does not show a smooth curve (Figure 4.6 for $C_{122}H_{246}$, Figure 4.10 for $C_{162}H_{326}$ and Figure 4.17 for $C_{390}H_{782}$). There is a bend, which was thought to be due to the transition from formation of once folded chain (**F2**) to formation of extended chain (**E**) crystal structures [63, 71].

After isothermal crystallization of $\mathbf{C_{390}H_{782}}$ at 119.3 °C, the first melting peak (Figure 4.22 – Figure 4.23) is at 126.5 – 127 °C. As discussed in the previous section, this is the melting temperature of the once folded crystal structure **F2**. Peak 2 at 131 – 132.5 °C corresponds to the melting temperature of the extended chain structure **E** of 132 °C [69]. Therefore, $C_{390}H_{782}$ crystallizes at 119.3 °C into **F2** first; between 20 s and 100 s, it transforms into **E**, which continues to grow even after 100 hours.

After crystallization at 125 °C, similar two melting peaks were observed (Figure 4.24): peak 1 (128.5 °C) from **F2** and peak 2 (131.5 °C) from **E**.

Therefore, the peak detected during crystallization shows formation of a folded structure (**F2**) which changes then to the extended chain (**E**). The temperatures (119.3 and 125 °C) are on different sides of the bend in Figure 4.17.

At 99.3 °C, no such stepwise change of the melting temperature was observed. Melting peak was shifting continuously from 120.5 to 126 °C (peak value) for crystallization times of 10 ms to 30 minutes. This is most probably due to non-integer folding.

Melting curves of $C_{162}H_{326}$ crystallized at 100 °C, 105 °C and 110 °C show two melting peaks: at 113 – 116 °C and at 125 °C (see Figure 4.12 and Figure 4.13 on page 74). Peak temperatures and heights for 105 °C and 110 °C are presented in Figure 4.26.
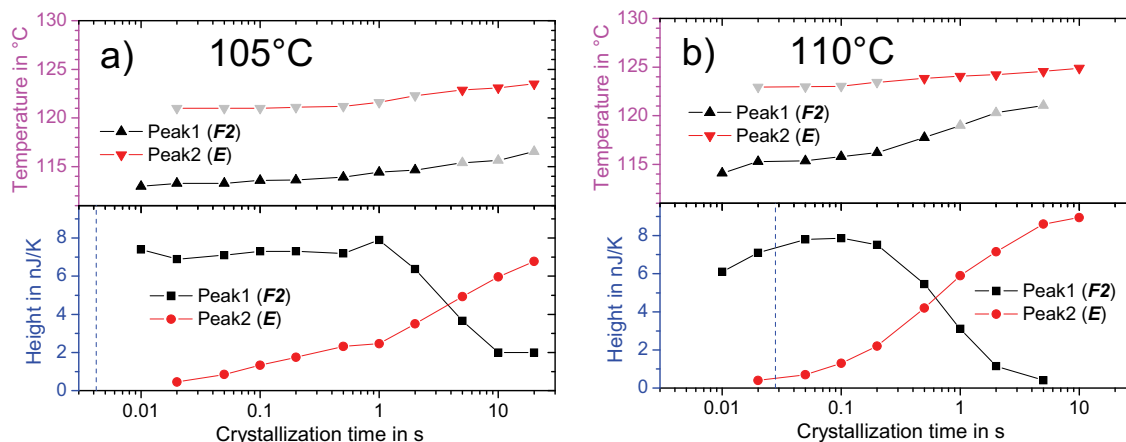
Figure 4.26: $C_{162}H_{326}$ melting peak temperature and height versus crystallization time at a) 105 °C; b) 110 °C. For conditions see Figure 4.12 (b) and Figure 4.13. Crystallization peak time from Figure 4.10 is labeled with a blue dash line. Temperature points are gray where peak height is little.

The temperature of the second peak is in a good agreement with literature data of 126.5 °C for the extended chain structure (*E*) crystallized at 120 – 124 °C for 10 minutes [62]. First melting peak at 113 – 116 °C should be melting of the once folded structure (*F2*).

At 105 °C, crystallization halftime of $C_{162}H_{326}$ is about 4 ms (see Figure 4.10). After 10 ms at this temperature, melting peak of *F2* was fully developed and melting peak of *E* was not detected (see Figure 4.26 (a)). At 110 °C, crystallization halftime of 27 ms from Figure 4.10 corresponds to the maximum increase of the *F2* melting peak in Figure 4.26 (b). Therefore, crystallization peak observed during crystallization corresponds to formation of the *F2*, similar to $C_{390}H_{782}$.

During crystallization of $C_{162}H_{326}$ at 111.6 °C and 112.6 °C (on the left side close to the bend in the kinetics curve), two crystallization peaks were observed. Time of the first crystallization peak (red points in Figure 4.10) continues the kinetic curve of the formation of the once-folded structure. The second peak (green points in Figure 4.10) represents formation of the extended chain structure. At 110 °C, the maximum of the crystallization rate for extended chain is in the range of 0.3 s (Figure 4.26 (b)); this fits together with points of the second crystallization peak in Figure 4.10. Remarkably, the slope of the temperature dependence of the kinetics of the formation of the extended chain corresponds to that of the once folded structure. This could indicate that both crystallizations are diffusion controlled in the same way.

At all three temperatures (100, 105 and 110 °C), once folded structure *F2* with a definite melting temperature is formed first. After some time, it is transformed into extended chain structure *E* (second melting peak). During this process, the remaining *F2* fraction becomes more thermally stable (increase of the melting temperature). This process takes 5 to 10 seconds at 110 °C, above 20 s at 105 °C and much longer time at 100 °C. Remarkably, all temperatures are on the left side from the bend in Figure 4.10 and still we end up with an extended chain structure. This indicates that *F2* is kinetically favored but it is not the thermodynamically stable form.

Once folded structure is formed at least down to 102 °C with a halftime of about 2 ms. No further crystallization modes (like double folding) were observed.

During crystallization of **$C_{122}H_{246}$**, double crystallization peak was seen at temperatures between 102.9 °C and 105.8 °C as well as at 99.9 °C (see Figure 4.5 on page 68). All temperatures except 99.9 °C are on the right side of the bend in the kinetic curve (Figure 4.6). Temperature dependence of the time of the second peak is similar to that of the first peak. Melting peak could not be evaluated because of reproducibility problems as it was described above.

Hosier and Bassett [62] have proven by SAXS measurements that in the temperature range between 116.0 and 119.4 °C, the material crystallizes into extended chain structure with melting temperature of about 121 °C. Our measurements show a smooth kinetic curve from 103 °C to 116.6 °C (see Figure 4.6), so the end structure at higher temperatures should be extended chain. Similar to the other two materials, near the bend in the kinetic curve at 103 °C, $C_{122}H_{246}$ forms once folded structure first (first crystallization peak) and then transforms into extended chain (second peak).

Similar two melting peaks were reported for solution crystallization near the bend in the kinetics curve of $C_{198}H_{398}$ [72], $C_{294}H_{590}$ [73], $C_{168}H_{338}$ [66]. Our results are for melt crystallization; the effect occurs in a broad temperature range. Double crystallization peak was observed up to 106 °C in $C_{122}H_{246}$, which is 3 K above the position of the bend in the kinetic curve of 103 °C; in $C_{162}H_{326}$ at temperatures below the bend (111.6 and 112.6 °C). In C390, the bend is at 124 °C; extended chain structure was obtained at 119.3 and at 125 °C.

Contrary to cited DSC studies, no crystallization was observed if FSC after melting of *F2* during the heating at 2000 K/s. Hence, the second melting peak is melting of *E* structure created during annealing at the crystallization temperature and not during the heating scan.

Therefore, the (first) maximum in heat production during isothermal crystallization comes from the formation of *F2*; then the structure changes to *E*. This happens on both sides of the bend in the

rate-temperature curve (first bend from the right). $C_{122}H_{246}$ shows double crystallization peak at temperatures on the right, $C_{162}H_{326}$ – on the left side of the bend in the kinetic curve.

The bend is not the change in the end structure (folded/extended chain). It is rather due to interplay between different kinetics of the different processes, what finally yield the bend in the crystallization kinetics curve.

4.5.3. Effective chain length and melting temperature

From the melting temperatures of extended chain crystals one can see that the longer the chain, the higher the melting temperature. Folded structure has lower melting temperature than the extended chain.

Melting temperatures of all integer crystallization modes as a function of the (reciprocal) crystal thickness expressed in number of CH_2 groups are presented in Figure 4.27. We have used the onset temperature according to GEFTA recommendation [46], because the peak is due to a sharp first order transition, similar to melting of metals.
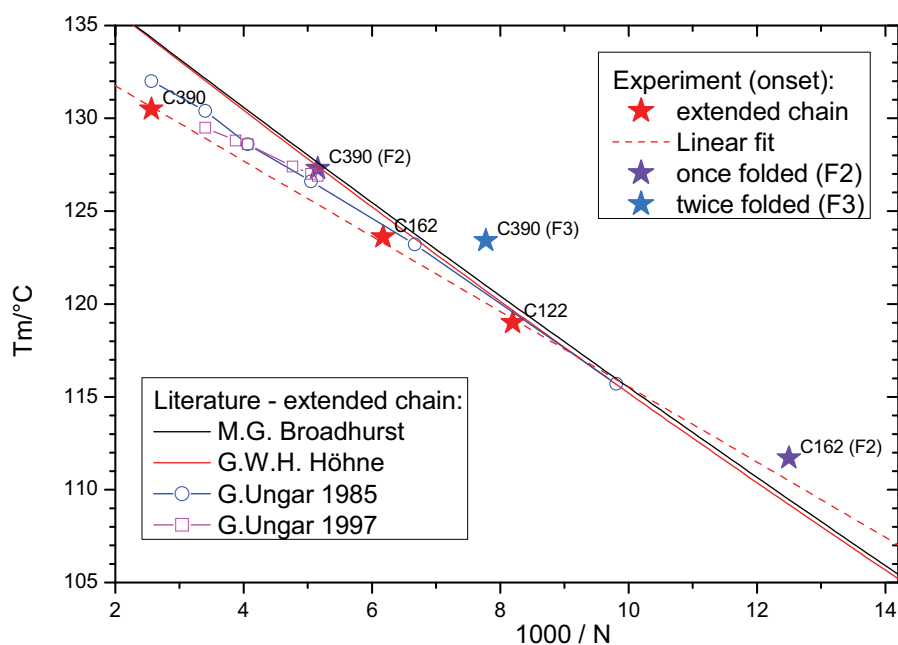
Figure 4.27: Melting temperature of n-alkanes versus reciprocal chain length. Dashed line is a linear fit of the extended chain points. Literature data is taken from [74] (black line, Tm(K) = 414.3(n-1.5)/(n+5.0)), [75] (red line, 1/Tm(K) = 2.413*10⁻³ + 0.0162/n), [69] (blue circles) and [65] (magenta squares).

Melting points of the extended chain structures are on a straight line (dashed red line in Figure 4.27). For once folded structures, half of the chain length was used as an "effective chain length". This way the points $C_{390}H_{782}$ (*F2*) and $C_{162}H_{326}$ (*F2*) fit to the results of the extended chain;

however, "folded" structures have a bit higher melting temperature. $C_{390}H_{782}$ (**F2**) point is 2 K above the line of the extended chain; $C_{162}H_{326}$ (**F2**) is 1.2 K above the extrapolation of that line.

There was a second bend in the crystallization kinetics of $C_{390}H_{782}$ at about 119 °C (Figure 4.17). With increasing crystallization temperature towards this value, melting temperature increases and then saturates at 123.4 °C (Figure 4.18, Figure 4.20). This may be the melting temperature of the double folded structure (**F3**). Corresponding point is 3.4 K above the line of extended chain melting temperatures.

This supports the idea of G.W.H. Höhne [75] that each part of a chain of N CH_2 groups folded into n "feels" the rest of the chain during cooperative movement, especially along the chain in the direction "from the bend". However, only N/n CH_2 groups have to be moved in the direction "from the free end" ("to the fold"). For detaching of the complete segment from the crystal, mostly the length of the segment N/n is important. Therefore, melting temperature of a folded crystal is higher than the melting temperature of extended chain structure of N/n CH_2 groups, but it is lower than that of the extended chain structures of N CH_2 groups.

Our results are presented in Figure 4.27 together with literature data. Melting temperatures of extended crystal structures are in good agreement with experimental points [65, 69].

The black curve represents the formula from Broadhurst [74]: $Tm(K) = 414.3(n-1.5)/(n+5.0)$. The red curve corresponds to a Gibbs-Thomson equation modified by G. W. H. Höhne [75]: $1/Tm(K) = 2.413*10^{-3} + 0.0162/n$. Values of melting temperature of infinite thick crystals are given as 414.3 [74] and 414.42 K [75]. In the range of chain lengths presented in this work, the difference between the results of the two equations is 0.3 K at most. For chain lengths below 1000/8 CH_2 groups, the theoretical results coincide with the extrapolation of the experimental curve for the extended chain. For longer molecules, the difference to the experimental data is more than 3 K.

Melting temperature for $C_{390}H_{782}$ E (extended chain) is below the theoretical curves from [75] and experimental curve 2 [69]; but may be it is on the extension of the experimental curve 3 [65]. The next $C_{390}H_{782}$ melting point (1x folded, or F2) coincides well with known data. And the lowest $C_{390}H_{782}$ melting temperature (after 1 s at 119 °C, see Figure 4.23) is neither F2 nor F3. Most probably, it is a non-integer folded structure. Melting temperatures of $C_{162}H_{326}$ (E and F2) and $C_{122}H_{246}$ (E) coincide with literature data quite well.

Chapter 5. Future possibilities of the method

5.1. Definition of heat losses

The definition of the function $\xi(T)$ is a sensitive point. Therefore, the heat losses function ideally should be measured under the same conditions as the measurement of interest. Some tricks to do this with a sample are described in section 3.2.1 on page 14. However, it is not always possible. A better way would be to take a second (empty) sensor, put it into the same oven and perform the same temperature scan simultaneously on both sensors (two-channel setup). This "reference" sensor will have similar function of heat losses (although not exactly the same: the shape and the surface of the heated part may be different because of the sample). If this problem does not occur the heat losses function $\xi(T)$ can be defined from the reference sensor and applied to the sample measurement.

Alternatively, one can perform measurements in a differential setup as it is continued in our group [76-78].

5.2. Control improvement

According to the formula (2.3), heater power equals

$$P = \left(C_s + C_{add}\right) \cdot \frac{dT}{dt} + \xi(T_s - T_0) \tag{5.1}$$

Only the second term of this equation is used so far. For an isotherm-heating-isotherm-cooling-isotherm temperature program, power profile looks like the black line in Figure 5.1.
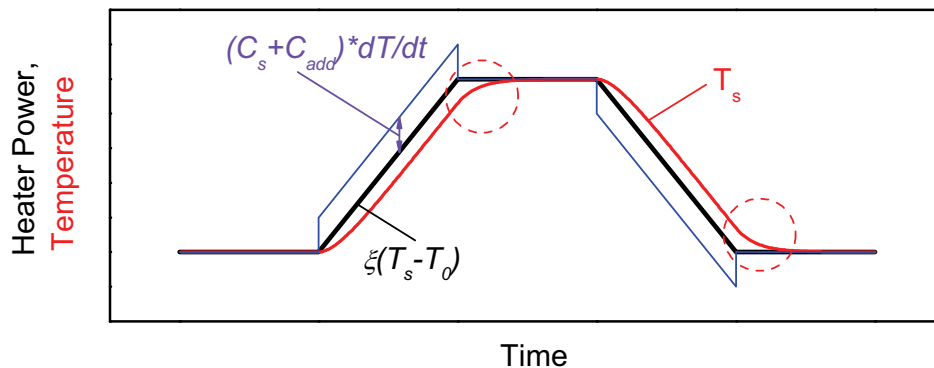
Figure 5.1: Heater power for fast transitions: black line – simple control; blue line – advanced control. Red curve – resulting sample temperature with simple control; exponential temperature decay is indicated by the circles.

At the transition from scanning to isotherm, sample temperature approaches the isothermal value with an exponential decay as illustrated by the red curve in Figure 5.1. To overcome this, one can add the "heating rate" term from the Equation (5.1) to the heater power; see blue line in Figure 5.1 or use a power compensation scheme [77-81]. An approximate value of $(C(T)+C_{add}(T))$ can be taken from a test measurement or estimated using trial-and-error technique and used for the control. This should eliminate delay between the program temperature and the real temperature and improve transitions especially from scanning to isotherm. In ideal case, real temperature will exactly follow the program temperature.

Another point is that any thermal effect in the sample will change the temperature profile. For example, in crystallization of PE (see Figure 3.19 on page 36): at low oven temperatures crystallization occurs so fast that the sample crystallizes already during cooling before reaching the desired crystallization temperature; heat released from the sample keeps the temperature several Kelvin above the desired value.

Active control of the sensor temperature ("power compensation") should be used for the measurements when the heat produced by the sample influences its temperature significantly. Examples of such controls are described in [77, 79-81]. The controller should be fast enough. At 100 000 K/s, the temperature changes by 1 K in 10 µs. A control loop with a cycle time of about 1 µs is needed for such rates. Most of digital controllers are too slow; therefore, an analog control circuit is preferable. However, fast integrated circuits (IC) like analog-to-digital converters[1] and Field Programmed Gate Arrays (FPGAs)[2] are already available; complete units for fast digital control implementations should appear on the market in the next future.

5.3. Other improvements

Modulated mode was realized only in the preliminary setup and not in the final one. Temperature modulation and Fourier transformation of the measured data or (alternatively) integration of a lock-in amplifier in the computer-controlled setup could extend the possibility to follow structure changes on long times, where direct heat signals are not more detectable.

The sensors described in this work operate well with high viscose samples. For **low viscose samples**, some sample cell (holder) has to be manufactured on the membrane. An arrangement for **liquids** could also extend application area of the method.

---

[1] For example, AD9446-100 from Analog Devices [82] performs 16 bit ADC conversion at 100 MHz.

[2] Virtex-6 series from Xilinx® [83] offer digital signal processing (DSP) slices with 600MHz clocking technology

Summary

In modern materials, properties of the material in the final product depend on its thermal history. To optimize the product and achieve specific properties, one has to reproduce the process in the lab with possibility to study how the change of any parameter affects the structure of the material. Cooling rates used in polymer manufacturing reach 1 000 K/s and more. On the other hand, commercially available calorimeters can barely cool faster than 10 K/s. There were works on ultra-fast heating and measurement during this heating. There were also some works with fast cooling, however control possibilities of the cooling rate were limited and there was no measurement during cooling. Here we show controlled ultra-fast cooling and measurement of sample temperature and thermal properties during and after cooling at up to 100 000 K/s with high resolution in time.

Sample holder is a 0.5 µm thick silicon-nitride membrane with a heater and a thermometer in the center where the sample is placed. The sample is cooled mostly by the surrounding gas. In case of helium at 10 kPa, about 5 % of the heat is transferred through the membrane. A frame with the membrane is placed in the **vacuum system** that fits into the Dewar vessel with liquid nitrogen. A temperature-controlled oven around the sample holder can be set at any temperature between -190 °C and +150 °C. The sensor is connected to the ADC board of the computer with LabVIEW software to control the measurements.

With this system, a technique for controlled fast cooling and heating as well as isothermal experiments with high time resolution was developed. The developed system allowed for the first time calorimetric measurements at high cooling rates.

As the sample is cooled from the surface, only a **very thin sample** can be cooled very fast, otherwise heat transfer problem inside the sample limits the cooling rate of the inner part. The samples studied in this work had diameter between 20 and 100 µm and thickness between 5 and 50 µm.

Calculations show that not thermal conductivity of the **cooling medium** alone but the combination of its heat capacity and thermal conductivity limits the cooling rate. It is shown that gas like hydrogen or helium can provide higher cooling rate than a solid cooling medium. Helium at reduced pressure of 10 kPa was used in most experiments presented in this work.

Cooling rates of more than 100 000 K/s were achieved using a TCG3880 sensor. Heating/cooling rates of up to 10^6 K/s were achieved in our group on this device using faster sensors. Scanning and isothermal measurements can be performed with **time resolution** of 0.1 ms.

Absolute **accuracy of temperature** measurement is better then ±2 K and **precision** better than 0.5 K.

Lowest scanning rate for measurement of heat capacity is in the order of 10 K/s depending on sample size. However, there is no low rate limit for the sample temperature treatment. Heat capacity measurement at scanning rates down to zero may be possible using AC-method.

Crystallization kinetics of poly(ε-caprolactone) (PCL), polyethylene (PE), isotactic polypropylene (iPP), syndiotactic polypropylene (sPP) with different content of carbon nanotubes as well as series of monodisperse n-alkanes was studied using the new technique.

Kinetics of isothermal crystallization in the whole temperature range between the glass transition and melting for PCL, iPP, sPP and sPP with addition of carbon nanotubes was studied. Logarithm of reciprocal crystallization halftime versus temperature for PCL and sPP is bell-shaped curve whereas that for iPP shows two maxima. Two different processes take place during crystallization: nucleation and crystal growth. Each of them has its own temperature dependence. Overall crystallization kinetics results from interplay of these two processes and this is the reason for such shape. Addition of as few as 1 % of carbon nanotubes influences dramatically the nucleation rate of sPP (one order of magnitude) making crystallization at high temperatures faster. However, crystallization kinetics in the low-temperature region (towards glass transition) is not affected by the carbon nanotubes. Crystallization rate of the material with 10 % carbon nanotubes is not much different from that with 1 %, therefore concentration of 1 % is enough for improvement of the crystallization rate.

It was found for several polymer materials that scanning rate needed to prevent crystallization on heating (2500 K/s for PCL) is ten times higher than the rate needed to prevent crystallization on cooling (PCL: 250 K/s).

The technique was applied for investigation of structure formation of three monodisperse n-alkane samples: $C_{122}H_{246}$, $C_{162}H_{326}$ and $C_{390}H_{782}$. Continuous Cooling Transformation (CCT) and isothermal crystallization kinetics as well as melting behavior after different crystallization processes was studied. Formation of different crystal structures was observed calorimetrically for the first time on cooling at rates up to 20 000 K/s and isothermally in the range of crystallization halftimes down to 2 ms.

All three samples show different crystalline structures depending on the crystallization conditions. At high temperatures, extended chain crystals are formed from the beginning. At lower

temperatures, significant part of the sample is crystallized into once folded structure (F2) first and then changes to extended chain. At even lower temperatures, folded into three (F3) and more as well as non-integer folded structures can be formed.

As direct methods of crystal thickness measurement were unavailable, crystalline structure was estimated using the melting temperature.

For all three samples, there is at least one bend in the isothermal crystallization halftime versus crystallization temperature curve. The bend is not the change in the end structure (folded/extended chain). It is rather due to interplay between different kinetics of the different processes (crystallization into F2, crystallization into E, transformation F2$\rightarrow$E) and a self-poisoning effect.

Literature

[1]   J.D. Verhoeven, L.L. Jones, Damascus Steel, Part II: Origin of the Damask Pattern, Metallography 20(2) (1987) 153-180.

[2]   M.F.J. Pijpers, V.B.F. Mathot, B. Goderis, R. Scherrenberg, E. van der Vegte, High-speed calorimetry for the analysis of kinetics of vitrification, crystallization and melting of macromolecule, Macromolecules 35(9) (2002) 3601-3613.

[3]   *http://www.hyperdsc.com*, HyperDSC by Perkin Elmer.

[4]   V. Brucato, F. De Santis, A. Giannattasio, G. Lamberti, G. Titomanlio, Crystallization during fast cooling experiments, a novel apparatus for real time monitoring, Macromol. Symp. 185 (2002) 181-196.

[5]   V. La Carrubba, S. Piccarolo, V. Brucato, Solidification of syndiotactic polystyrene by a continuous cooling transformation approach, Journal of Polymer Science Part B: Polymer Physics 45(19) (2007) 2688-2699.

[6]   V. Brucato, S. Piccarolo, V. La Carrubba, An experimental methodology to study polymer crystallization under processing conditions. The influence of high cooling rates, Chem. Eng. Sci. 57(19) (2002) 4129-4143.

[7]   A.D. Rakhel, G.S. Sarkisov, Melting and volume vaporization kinetics effects in tungsten wires at the heating rates of 10(12) to 10(13)K/s, International Journal of Thermophysics 25(4) (2004) 1215-1233.

[8]   B. Wilthan, C. Cagran, G. Pottlacher, Combined DSC and Pulse-Heating Measurements of Electrical Resistivity and Enthalpy of Tungsten, Niobium, and Titanium, Intern. J. Thermophysics 26(4) (2005) 1017-1029.

[9]   L.H. Allen, G. Ramanath, S.L. Lai, Z. Ma, S. Lee, D.D.J. Allman, K.P. Fuchs, 1 000 000 °C/s thin film electrical heater: In situ resistivity measurements of Al and Ti/Si thin films during ultra rapid thermal annealing, Appl. Phys. Lett. 64(4) (1994) 417-419.

[10]   W. Zielenkiewicz, CALORIMETRY Institute of Physical Chemistry of the Polish Academy of Sciences, Warszawa, 2005.

[11]   E. Calvet, H. Prat, H.A. Skinner, Recent progress in microcalorimetry, Pergamon Press, Oxford, London, New York, Paris, 1963.

[12]   O.M. Corbino, Thermische Oszillationen wechselstromdurchflossener Lampen mit dünnem Faden und daraus sich ergebende Anwesenheit geradzahliger Oberschwingungen, Physik. Zeitschr. XI (1910) 413-417.

[13]   O.M. Corbino, Periodische Widerstandsänderungen feiner Metallfäden, die durch Wechselströme zum Glühen gebracht werden, sowie Ableitung ihrer thermischen Eigenschaften bei hoher Temperatur, Physik. Zeitschr. XII (1911) 292-295.

[14]   Y.A. Kraftmakher, Modulation method of heat capacity measurement, Zhurnal Prikladnoi Mekhaniki i Tekhnicheskoi Fiziki 5 (1962) 176-180.

[15]   Y.A. Kraftmakher, Modulated heat capacity measurement using thermoelectrical sensors, Raboty po Fizike Tverdogo Tela 2 (1967) 219-222.

[16]   P. Handler, D.E. Mapother, M. Rayl, AC Measurement of the Heat Capacity of Nickel Near its Critical Point, Phys. Rev. Lett. 19(7) (1967) 356-358.

[17]   P.F. Sullivan, G. Seidel, Steady-State, ac-Temperature Calorimetry, Phys. Rev. 173 (1968) 679-685.

[18]   H. Gobrecht, K. Hamann, G. Willers, Complex plane analysis of heat capacity of polymers in the glass transition region, J. Phys. E: Scientific Instruments 4 (1971) 21-23.

[19]   N.O. Birge, S.R. Nagel, Specific-heat spectroscopy of the glass transition, Phys. Rev. Lett.

54(25) (1985) 2674-2677.

[20]   B. Wunderlich, A. Boller, I. Okazaki, K. Ishikiriyama, Heat-capacity determination by temperature-modulated DSC and its separation from transition effects, Thermochim. Acta 305 (1997) 125-136.

[21]   A. Wurm, M. Merzlyakov, C. Schick, Crystallization of polymers studied by temperature-modulated techniques (TMDSC, TMDMA), J. Macromol. Sci.-Phys. B38(5-6) (1999) 693-708.

[22]   C. Schick, A. Wurm, A. Mohammed, Vitrification and devitrification of the rigid amorphous fraction of semicrystalline polymers revealed from frequency-dependent heat capacity, Colloid Polym. Sci. 279 (2001) 800-806.

[23]   K.H. Illers, Die Ermittlung des Schmelzpunktes von kristallinen Polymeren mittels Wärmeflusskalorimetrie (DSC), Eur. Polym. J. 10(10) (1974) 911-916.

[24]   J.H. Flynn, Thermal analysis kinetics-problems, pitfalls and how to deal with them, J. Therm. Anal. 34 (1988) 367-381.

[25]   A.A. Minakov, S.A. Adamovsky, C. Schick, Non adiabatic thin-film (chip) nanocalorimetry, Thermochim. Acta 432(2) (2005) 177-185.

[26]   D.R. Lide, CRC Handbook of Chemistry and Physics, 79th ed, Boca Raton, Boston London, New York, Washington, 1998.

[27]   J. Brandrup, E.H. Immergut, E.A. Grulke, Polymer Handbook John Wiley & Sons, 1999.

[28]   *http://www.xensor.nl*, Xensor Integration.

[29]   O. Kubaschewski, R. Hultgren, Metallurgical and Alloy Thermochemistry, in: H.A. Skinner (Ed.), Experimental Thermochemistry, Interscience, New York, 1962.

[30]   M. Merzlyakov, Integrated Circuit Thermopile as a New Type of Temperature Modulated Calorimeter, Thermochim. Acta 403(1) (2003) 65-81.

[31]   A.A. Minakov, S.B. Roy, Y.V. Bugoslavsky, L.F. Cohen, Thin-film alternating current nanocalorimeter for low temperatures and high magnetic fields, Rev. Sci. Instrum. 76 (2005) 043906.

[32]   H. Huth, A. Minakov, C. Schick, High Sensitive Differential AC-Chip Calorimeter for Nanogram Samples, Netsu Sokutei 32(2) (2005) 70-76.

[33]   S. Adamovsky, C. Schick, Ultra-fast isothermal calorimetry using thin film sensors, Thermochim. Acta 415 (2004) 1-7.

[34]   X.F. Lu, J.N. Hay, Isothermal crystallization kinetics and melting behaviour of poly(ethylene terephthalate), Polymer 42(23) (2001) 9423-9431.

[35]   L. Sorrentino, S. Iannace, E. DiMaio, D. Acierno, Isothermal Crystallization Kinetics of Chain-Extended PET, J. Polym. Sci. B: Polym. Phys. 43 (2005) 1966-1972.

[36]   S.A. Jabarin, Crystallization kinetics of polyethylene terephthalate. I. Isothermal crystallization from the melt, J. Appl. Polym. Sci. 34 (1987) 85-96.

[37]   J.M. Huang, F.C. Chang, Crystallization kinetics of poly(trimethylene terephthalate), Journal of Polymer Science Part B-Polymer Physics 38(7) (2000) 934-941.

[38]   B.J. Chisholm, J.G. Zimmer, Isothermal crystallization kinetics of commercially important polyalkylene terephthalates, J. Appl. Polym. Sci. 76(8) (2000) 1296-1307.

[39]   V. Balsamo, D. Newman, L. Gouveia, L. Herrera, M. Grimau, E. Laredo, Molecular dynamics and crystallization kinetics in PSMA14/PCL blends, Polymer 47 (2006) 5810-5820.

[40]   *http://athas.prz.rzeszow.pl*, ATHAS databank.

[41]   G.R. Strobl, The Physics of Polymers, Springer, Berlin, 1997.

[42]   H. Yinnon, D.R. Uhlmann, Applications of Thermoanalytical Techniques to the Study of Crystallization Kinetics in Glass-Forming Liquids .1. Theory, Journal of Non-Crystalline Solids 54(3) (1983) 253-275.

[43]   W.H. Cobbs, R.L. Burton, Crystallization of polyethylene terephthalate, J. Polym. Sci. 10(3) (1953) 275-290.

[44]   P.H. Verdier, H.L. Wagner, The Characterization of linear Polyethylene SRM's 1482, 1483, and 1484, Journal of Research of the National Bureau of Standards 83(2) (1978) 169-201.

[45]   M.Y. Efremov, E.A. Olson, M. Zhang, F. Schiettekatte, Z. Zhang, L.H. Allen, Ultrasensitive, fast, thin-film differential scanning calorimeter, Rev. Sci. Instrum. 75(1) (2004) 179-191.

[46]   G.W.H. Höhne, H.K. Cammenga, W. Eysel, E. Gmelin, W. Hemminger, The temperature calibration of scanning calorimeters, Thermochim. Acta 160(1) (1990) 1-12.

[47]   V. Drebushchak, Calibration coefficient of a heat flow DSC - Part III. Electromotive force of a thermocouple as a function of temperature, Journal of Thermal Analysis and Calorimetry 90(1) (2007) 289-298.

[48]   R.V. Castillo, M.L. Arnal, A.J. Muller, I.W. Hamley, V. Castelletto, H. Schmalz, V. Abetz, Fractionated Crystallization and Fractionated Melting of Confined PEO Microdomains in PB-b-PEO and PE-b-PEO Diblock Copolymers, Macromolecules 41(3) (2008) 879-889.

[49]   M. Trujillo, M.L. Arnal, A.J. Muller, S. Bredeau, D. Bonduel, P. Dubois, I.W. Hamley, V. Castelletto, Thermal Fractionation and Isothermal Crystallization of Polyethylene Nanocomposites Prepared by in Situ Polymerization, Macromolecules (2008).

[50]   F. De Santis, S. Adamovsky, G. Titomanlio, C. Schick, Scanning nanocalorimetry at high cooling rate of isotactic polypropylene, Macromolecules 39 (2006) 2562-2567.

[51]   F. De Santis, S. Adamovsky, G. Titomanlio, C. Schick, Isothermal nanocalorimetry of isotactic polypropylene, Macromolecules 40 (2007) 9026-9031.

[52]   K. Wiemann, W. Kaminsky, F.H. Gojny, K. Schulte, Synthesis and Properties of Syndiotactic Poly(propylene)/Carbon Nanofiber and Nanotube Composites Prepared by in situ Polymerization with Metallocene/MAO Catalysts, Macromolecular Chemistry and Physics 206(15) (2005) 1472-1478.

[53]   *http://www.nanocyl.com*, Nanocyl s.a.

[54]   L. Guadagno, C. Naddeo, M. Raimondo, G. Gorrasi, V. Vittoria, Effect of carbon nanotubes on the photo-oxidative durability of syndiotactic polypropylene, Polymer Degradation and Stability In Press, Corrected Proof.

[55]   B. Wunderlich, Reversible crystallization and the rigid-amorphous phase in semicrystalline macromolecules, Progr. Polym. Sci. 28(3) (2003) 383-450.

[56]   P. Supaphol, Crystallization and melting behavior in syndiotactic polypropylene: Origin of multiple melting phenomenon, J. Appl. Polym. Sci. 82 (2001) 1083-1097.

[57]   P. Supaphol, J.E. Spruiell, Isothermal melt- and cold-crystallization kinetics and subsequent melting behavior in syndiotactic polypropylene: a differential scanning calorimetry study, Polymer 42(2) (2001) 699-712.

[58]   M. Dirand, M. Bouroukba, A.-J. Briard, V. Chevallier, D. Petitjean, J.-P. Corriou, Temperatures and enthalpies of (solid + solid) and (solid + liquid) transitions of n-alkanes J.Chem.Thermodynamics 34(8) (2002) 1255-1277.

[59]   A. Minakov, A. Wurm, C. Schick, Superheating in linear polymers studied by ultrafast nanocalorimetry, Eur. Phys. J. E Soft Matter 23(1) (2007) 43-53.

[60]   A.A. Minakov, A.W. van Herwaarden, W. Wien, A. Wurm, C. Schick, Advanced nonadiabatic ultrafast nanocalorimetry and superheating phenomenon in linear polymers, Thermochim. Acta 461(1-2) (2007) 96-106.

[61]   G.M. Brooke, S. Burnett, S. Mohammed, D. Proctor, M.C. Whiting, Versatile process for the syntheses of very long chain alkanes, functionalised derivatives and some branched chain hydrocarbons, Journal of the Chemical Society-Perkin Transactions 1(13) (1996) 1635-1645.

[62]   I.L. Hosier, D.C. Bassett, A study of the morphologies and growth kinetics of three monodisperse n-alkanes: $C_{122}H_{246}$, $C_{162}H_{326}$ and $C_{246}H_{494}$, Polymer 41(25) (2000) 8801-8812.

[63]   G. Ungar, A. Keller, Inversion of the Temperature-Dependence of Crystallization Rates Due to Onset of Chain Folding, Polymer 28(11) (1987) 1899-1907.

[64]   A. Keller, S.J. Organ, G. Ungar, New Trends in Polymer Crystallization Studies Part I — From Alkanes to Polyethylene: the Onset of Chain Folding in Polymer Crystallization, Makromolekulare Chemie-Macromolecular Symposia 48/49 (1991) 93-102.

[65]   E. Boda, G. Ungar, G.M. Brooke, S. Burnett, S. Mohammed, D. Proctor, M.C. Whiting, Crystallization Rate Minima in a Series of N-Alkanes from C194H390 to C294H590, Macromolecules 30(16) (1997) 4674-4678.

[66]   R.G. Alamo, L. Mandelkern, G.M. Stack, C. Krohnke, G. Wegner, Crystallization kinetics of long-chain n-alkanes from the melt and from solution, Macromolecules 27(1) (1994) 147-156.

[67]   S.M. Sarge, G.W.H. Hohne, H.K. Cammenga, W. Eysel, E. Gmelin, Temperature, heat and heat flow rate calibration of scanning calorimeters in the cooling mode, Thermochim. Acta 361 (2000) 1-20.

[68]   S. Neuenfeld, C. Schick, Verifying the symmetry of differential scanning calorimeters concerning heating and cooling using liquid crystal secondary temperature standards, Thermochim. Acta 446(1-2) (2006) 55-65.

[69]   G. Ungar, J. Stejny, A. Keller, I. Bidd, M.C. Whiting, The crystallization of ultralong normal paraffins: the onset of chain folding, Science 229 (1985) 386-389.

[70]   G. Ungar, K.B. Zeng, Learning polymer crystallization with the aid of linear, branched and cyclic model compounds, Chem. Rev. 101(12) (2001) 4157-4188.

[71]   J.D. Hoffman, Transition from extended-chain to once-folded behaviour in pure n-paraffins crystallized from the melt, Polymer 32(15) (1991) 2828-2841.

[72]   S.J. Organ, G. Ungar, A. Keller, Rate Minimum in Solution Crystallization of Long Paraffins, Macromolecules 22(4) (1989) 1995-2000.

[73]   R.L. Morgan, P.J. Barham, M.J. Hill, A. Keller, S.J. Organ, The Crystallization of the N-Alkane C294H590 from Solution - Inversion of Crystallization Rates, Crystal Thickening, and Effects of Supersaturation, J. Macromol. Sci., Phys. B37(3) (1998) 319-338.

[74]   M.G. Broadhurst, An analysis of the solid phase behaviour of the normal paraffins, J. Res. NBS 66A(3) (1962) 241-249.

[75]   G.W.H. Höhne, Another approach to the Gibbs–Thomson equation and the melting point of polymers and oligomers, Polymer 43 (2002) 4689-4698.

[76]   Y.L. Gao, E. Zhuravlev, C.D. Zou, B. Yang, Q.J. Zhai, C. Schick, Calorimetric measurements of undercooling in single micron sized SnAgCu particles in a wide range of cooling rates, Thermochim. Acta 482 (2009) 1-7.

[77]   E. Zhuravlev, C. Schick, Fast scanning power compensated differential scanning nano-calorimeter: 1. The device, Thermochimica Acta 505(1-2) (2010) 1-13.

[78]   E. Zhuravlev, C. Schick, Fast scanning power compensated differential scanning nano-calorimeter: 2. Heat capacity analysis, Thermochimica Acta 505(1-2) (2010) 14-21.

[79]   A.F. Lopeandía, L.I. Cerdó, M.T. Clavaguera-Mora, L.R. Arana, K.F. Jensen, F.J. Muñoz, J. Rodríguez-Viejoa, Sensitive power compensated scanning calorimeter for analysis of phase transformations in small samples, Rev. Sci. Instrum. 76 (2005) 065104.

[80]   A.F. Lopeandia, J. Valenzuela, J. Rodríguez-Viejo, Power compensated thin film calorimetry at fast heating rates, Sensors and Actuators A: Physical 143(2) (2008) 256-264.

[81]   M. Merzlyakov, Method of Rapid (100,000 K/s) Controlled Cooling and Heating of Thin Samples, Thermochim. Acta 442 (2006) 52-60.

[82]   *http://www.analog.com*, Analog Devices, Inc.

[83]   *http://www.xilinx.com*, Xilinx, Inc.

[84]   *http://www.measurementcomputing.com*, Measurement Computing Corporation.

[85]   *http://www.meilhaus.de*, Meilhaus Electronic GmbH.

Appendix A. Electronics of the computer controlled calorimeter

A simple scheme of the calorimeter is presented in Figure A.1. Electrical current for the heater is generated by a digital-to-analog converter (DAC) at a specified rate. Voltage drop on a reference resistor R_{ref} and on the heater are measured by two analog-to-digital converters (ADC). This allows us to calculate heater power and heater resistance. A third ADC is used for the thermopile voltage that gives us a sample temperature.
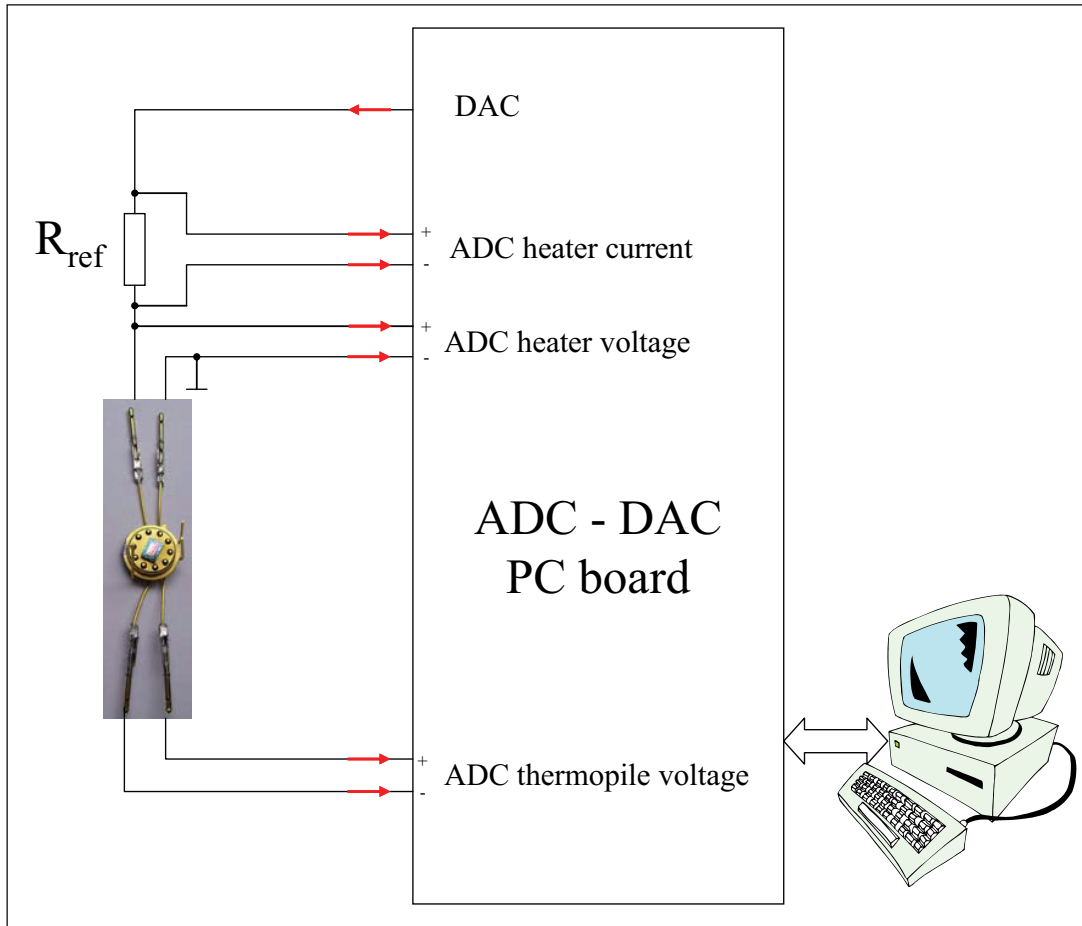

Figure A.1: Simple scheme of a fast scanning calorimeter.

At the beginning a Pentium III computer and a PCI-DAS64/M1/16 board from Measurement Computing™ [84] were used. The board has 64 single-ended (32 differential) multiplexed inputs and a 16-bit ADC which can operate at up to 1 MHz sampling frequency.

According to specifications, a crosstalk between any two input channels ("influence of one channel upon another when scanning two channels at the maximum rate" [84]) has to be not more than 15 LSB (which are $2.3*10^{-4}$, or 0.23 mV/V) in most cases. However, the testing conditions for

this are rather unrealistic: a signal is applied to one channel and another channel is tied to Analog Ground directly at the board connector. In the calorimeter, we have a thermopile connected through a cable to one of ADC inputs. Its internal resistance of about 30 kOhm should be negligible in compare to the specified input impedance of $10*10^{11}$ Ohms. To check if the board performs as it is promised by the manufacturer, the following test was carried out. Channel 0 was grounded through a 10-kOhm resistor, which is even lower than the thermopile, so it is better for the board. A saw tooth generator signal with an amplitude of 2 V (-2 V to +2 V) and a frequency of 1 kHz was applied to channel 1. Channels 2 and 3 were left non-connected to imitate a high impedance signal source. Input channels were acquired in a sequence 0-1-2-3-0-1-2-3-… using the test software supplied with the board. The measured voltage from the ADCs is presented in Figure A.2.
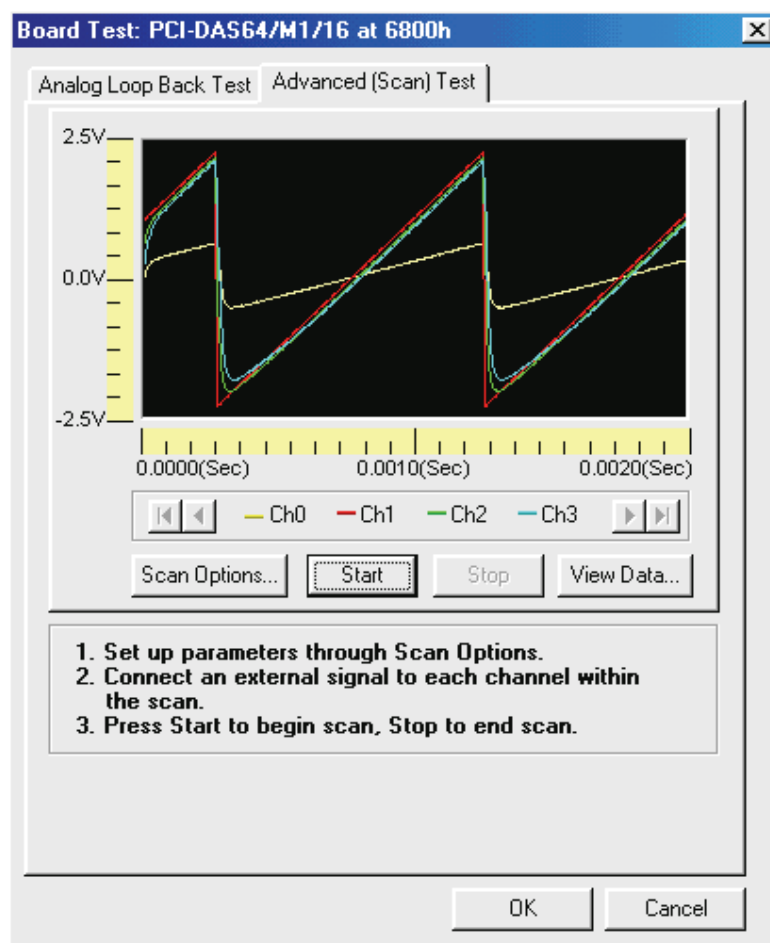
Figure A.2: Cross-talk check of a Measurement Computing PCI-DAS64/M1/16 ADC board. Test conditions: Channel 0: grounded over a 10 kΩ resistor; Channel 1: generator signal; Channel 2 and 3: floated.

There is clean generator signal on channel 1. Almost the same signal is read from unconnected channels 2 and 3. This says definitely that the specified input impedance of $10*10^{11}$ Ohms is

effectively not true in the multichannel operation at rated ADC frequency of 1 MHz. And on the channel 0 we read not the expected zero, but about 25 % of the generator signal which is applied to channel 1. Even if input channel 3 was tied to Analog Ground at the end of the cable there was still about 10 % of the signal of channel 1 which is still 500 times more than it was expected. The reason for such a strange behavior is the internal structure of the board. For such a unit one expects there should be buffer amplifiers for each channel to untie the signal source and a cable from the multiplexer, as it is made in the ME-FoXX Series boards from Meilhaus Electronic according to the manual taken from their web-site [85]. This expected structure is presented in the Figure A.3 (left side). On the right side in Figure A.3 is what we have found in the ADC board from Measurement Computing. All inputs are connected directly to the multiplexer.
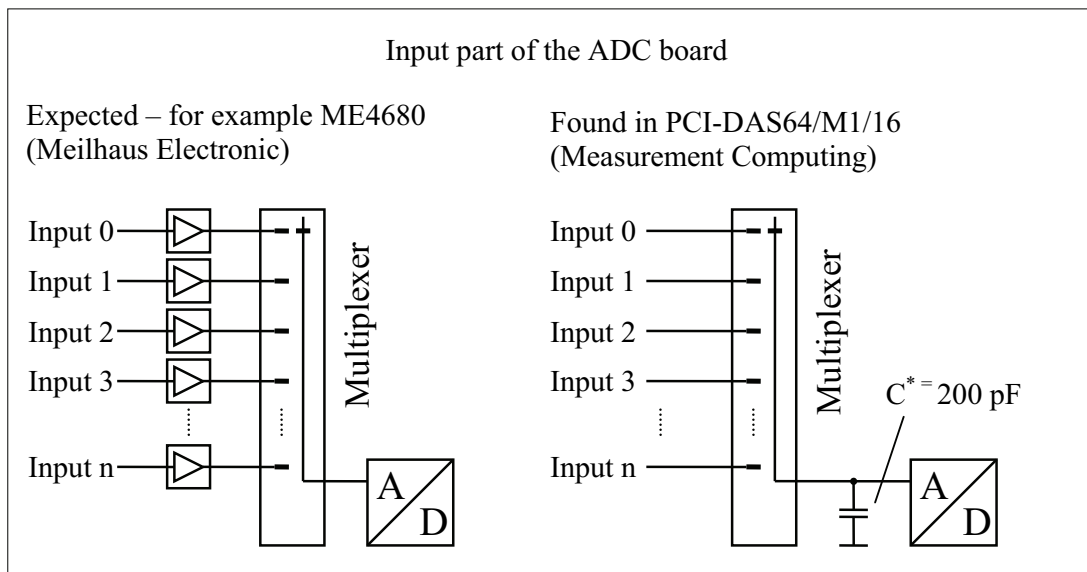
Figure A.3: Internal structure of the input part of an ADC board. In contrary to the expected construction (left side) the PCI-DAS64/M1/16 board has no buffer amplifiers and a large capacity after a switch (right side).

On the multiplexer output, there is a large capacity C^* of the following circuit. We estimate its capacitance about 200 pF. This capacity should be recharged from the voltage of the previous channel to the voltage of the next one in a very short time (less than 1 μs on the highest ADC rate) each time when the multiplexer switches from one channel to the next. For this recharge, a large current is needed from the signal source. A signal source with output impedance of 10-100 kOhm is unable to deliver such current.

There are two workarounds to solve the problem. First, an output impedance of the signal source should be dramatically reduced. The second is to reduce ADC rate; details are given below. To adapt the output impedance of the signal source, a buffer amplifier was built. The circuit diagram is shown in Figure A.4.
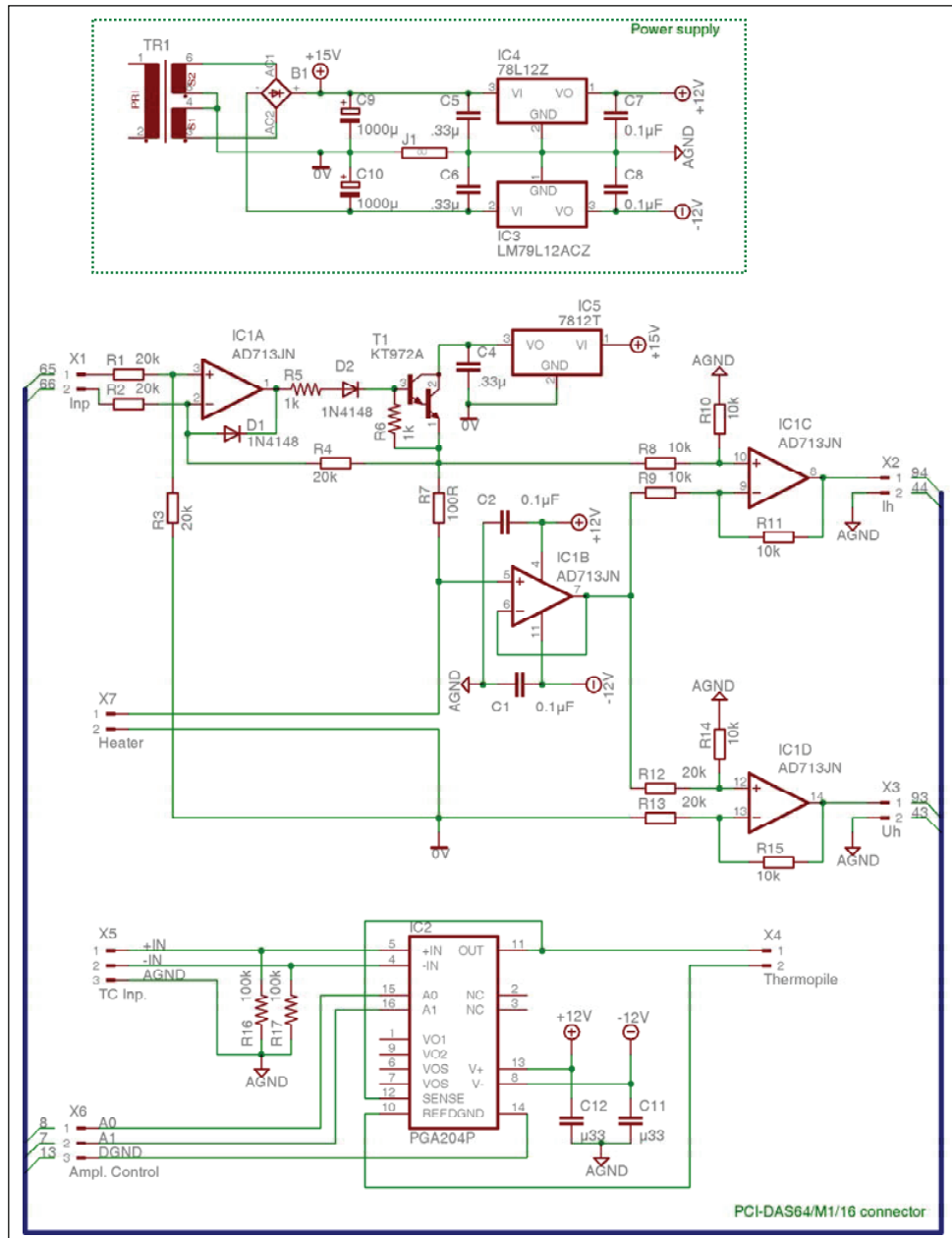
Figure A.4: First electronics for computer controlled calorimeter. R7 is a reference resistor to measure heater current. Blue bus represents a 100-pin cable connector of the ADC board.

Integrated circuit operational amplifier with low zero drift AD713J is used in the heater section (IC1A…IC1D). Its high output current (25 mA) with a good output protection as well as fast settling (1 μs to 0.01%) and wide frequency range (small signal bandwidth of 4 MHz) [82] made it a perfect choice for the buffer amplifier. A four-unit package (four amplifiers on one chip) was used to simplify the board layout and reduce noise.

The amplifier output for the heater is sufficiently positive; this is guaranteed by the diode D2 and transistor T1. T1 is a russian military device of type KT972; it is a Darlington pair with total current gain of more than 750, it operates stable up to high frequencies (200 MHz is the limit) and has a maximum collector current of 4 A.

When differential input voltage of IC1A becomes negative (this can happen at zero input voltage due to zero shifts), the resulting negative output voltage from pin 1 cannot reach the inverting input through the negative feedback circuit R4 because of "positive output sircuit" on D2 and T1. The output of IC1A would saturate at negative supply voltage. To prevent this, a diode D1 keeps it above -0.6 V. This improves recovery time when the input voltage starts to increase.

IC1C with unity gain is used to measure a voltage on a reference resistor R7 to get heater current (this differential amplifier also removes the common voltage component). IC1D with a gain of 0.5 adapts heater voltage signal for ADC. Buffer amplifier IC1B with high input impedance and unity gain feeds 20 kOhm and 30 kOhm inputs of amplifiers on IC1C and IC1D respectively.

Amplifier for the thermopile signal is built on the IC2 PGA204P. This is an instrumental amplifier with very low offset voltage and drift, high input impedance and programmable gain. Gain is selected between 1, 10, 100 and 1000 by two logical inputs. Two resistors (R16, R17) provide a return path for the input bias current as required by specification of the IC. Two resistors are needed because of high resistance of the thermopile (order of 50 kΩ).

Power ground (0V) and alanog ground are connected in one point in the power supply; analog ground is connected to digital groung on the ADC board.

It turned out that the only shielded cable offered by Measurement Computing (to be exact by their German representative, PLUG-IN Electronic GmbH) for this board has most probably wrong wires shielded: the same cable is offered for a larger series of boards with totally different pinout. As a result most of ADC lines had a very noisy signal; only a few of them were found to be good. Channel 4 was chosen for thermocouple voltage, channel 5 for heater current and channel 6 for heater voltage.

A channel scan rate of about 100 kHz (about 300 kHz ADC rate) was found to be maximum rate at which the measured results are still not significantly affected by the rest-charge-effect.

There was a need for a second measurement system in the lab, so another system was built. In the new system, the electronics was replaced by a new and more powerful one. The scheme is presented in Figure A.5. First, a National Instruments™ PXI system from was used to reduce the influence of electromagnetic noise of the computer (power supply etc.). This system was designed for measurements and it is much better shielded than a normal desktop computer.

Second, the National Instruments™ PXI-6120 module helped to avoid many problems related to the ADC board from Measurement Computing™. This module has four separate ADC units (three of them were used), so the problem of cross talk between different ADC channels due to switching was eliminated. Together with good input sensitivity, this allowed to exclude the external input amplifiers and to connect signals from the sensor directly to the ADC module. Zero drift was dramatically reduced and signal to noise ratio was significantly improved. Input impedance for the thermopile was increased from 200 kOhm to 1 MOhm. Anti-aliasing filter of the NI system has also improved the signal quality. Maximum ADC rate per channel was increased from 100 kHz to 500 kHz. According to specification, the highest acquisition frequency is 800 kHz. However, at maximum frequency, the signal is disturbed by some periodic spikes that are most probably caused by some interference between acquisition and copying of data from ADC memory to the main computer memory. At 500 kHz and below, the problem was not observed.
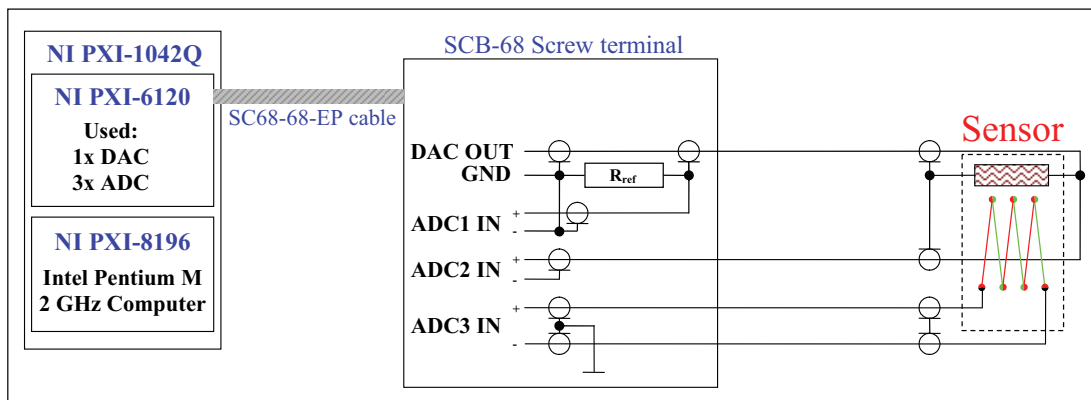
Figure A.5: PXI-based calorimeter.

The output stage of the DAC can provide the output current of up to 5 mA, which is enough to heat up the sample by more than 400 K, so the additional amplifier for the heater was not needed. The output impedance of the DAC amplifier is 50 Ohm (in comparison to nearly 0 Ohm in previous construction), so this had to be taken into account in the formula for calculation of the output voltage.

ADC inputs of the PXI-6120 module are not truly differential (input "-" should be kept within ±2.5 V to the ground for all input ranges). Therefore, a reference resistor for measurement of the heater current was connected in the "ground" wire of the heater. This has slightly increased the average voltage between the heater and the thermopile; however, as isolation on the sensor is good enough, this voltage did not make any problems.

With this module, it was possible to start generation and acquisition simultaneously using hardware triggering. Therefore, the software correction of the time shift in the measured data was not needed.

One should also mention the improvement in the handling of the equipment. The DAC part of the PXI-6120 module produces almost no spikes on the output during power-up, so the sensor and even the sample are not damaged any more if the heater is connected to the board while the system power is switched on.

Appendix B. Mathcad software for thermopile calibration

Mathcad program for thermopile calibration is presented in Figure B.1 and Figure B.2. Original data are copied directly to the worksheet (variable "Data", marked turquoise); format is specified in the worksheet comment. Fit function ("Ux") is marked pink. Division by 10^3 was needed to force Mathcad the right way for optimization. Parameters "c", "d" and "e" were introduced for higher polynomial fit order. Now, they are multiplied by 0 to use only quadratic function.

$$
\text{Data} := \begin{pmatrix}
0.193 & -100 & 156.61 \\
0.168 & -60 & 156.61 \\
0.147 & -30 & 156.61 \\
0.125 & 0 & 156.61 \\
0.102 & 30 & 156.61 \\
0.103 & 30 & 156.61 \\
0.07 & 70 & 156.61 \\
0.037 & 110 & 156.61 \\
0.012 & 140 & 156.61 \\
0.191 & 0 & 231.88 \\
0.168 & 30 & 231.88 \\
0.137 & 70 & 231.88 \\
0.104 & 110 & 231.88 \\
0.078 & 140 & 231.88 \\
0.29 & 0 & 327.47 \\
0.267 & 30 & 327.47 \\
0.269 & 30 & 327.47 \\
0.236 & 70 & 327.47 \\
0.212 & 100 & 327.47 \\
0.202 & 110 & 327.47 \\
0.176 & 140 & 327.47
\end{pmatrix}
$$

Input data format:
voltage, oven temp., sample temperature.
All temperatures are in °C.

$\text{Uexp} := \text{Data}^{\langle 0 \rangle} \quad \text{Tov} := \text{Data}^{\langle 1 \rangle} \quad \text{Tm} := \text{Data}^{\langle 2 \rangle} \quad i := 0\,..\,\text{rows}(\text{Data}) - 1$

$$
\text{Ux}(T, a, b, c, d, e) := \frac{a \cdot T + b \cdot T^2 + 0 \cdot c \cdot T^3 + 0 \cdot d \cdot T^4 + 0 \cdot e \cdot T^5}{10^3}
$$

$a1 := 2 \quad a2 := 0 \quad a3 := 0 \quad a4 := 0 \quad a5 := 0$

Given

$$
\sum_i \left[\left(\text{Ux}\!\left(\text{Tm}_i, a1, a2, a3, a4, a5\right) - \text{Ux}\!\left(\text{Tov}_i, a1, a2, a3, a4, a5\right) \right) - \text{Uexp}_i \right]^2 = 0
$$

$$
\begin{pmatrix} a1 \\ a2 \\ a3 \\ a4 \\ a5 \end{pmatrix} := \text{Minerr}(a1, a2, a3, a4, a5) \qquad
\begin{pmatrix} a1 \\ a2 \\ a3 \\ a4 \\ a5 \end{pmatrix} =
\begin{pmatrix}
7.226039 \times 10^{-1} \\
4.771328 \times 10^{-4} \\
0 \times 10^{0} \\
0 \times 10^{0} \\
0 \times 10^{0}
\end{pmatrix}
$$

$F(T) := \text{Ux}(T, a1, a2, a3, a4, a5)$

Figure B.1: Mathcad program for thermopile calibration (Part 1)

$$Ucalc_i := F(Tm_i) - F(Tov_i) \qquad j := 0..1000 \qquad Ttab_j := j \qquad Utab_j := F(Ttab_j - 273.15)$$

$$dUdT(T) := \frac{d}{dT}F(T) \qquad \delta U_i := Uexp_i - Ucalc_i \qquad \delta T_i := \frac{\delta U_i}{dUdT(Tm_i)} \qquad \max(\delta T) = 3.198083006$$
$$\min(\delta T) = -4.974877592$$

$$\delta T = \begin{pmatrix} 0.736 \\ 1.711 \\ 1.011 \\ 0.15 \\ -0.874 \\ 0.273 \\ -2.235 \\ -2.993 \\ -2.698 \\ -2.344 \\ -3.289 \\ -3.488 \\ -4.187 \\ -4.975 \\ 2.128 \\ 1.266 \\ 3.198 \\ 1.085 \\ 1.193 \\ -0.519 \\ -1.237 \end{pmatrix}$$

$$\text{augment}(Tov, Tm, Tm + \delta T, \delta T) = \begin{pmatrix} -100 & 156.61 & 157.346 & 0.736 \\ -60 & 156.61 & 158.321 & 1.711 \\ -30 & 156.61 & 157.621 & 1.011 \\ 0 & 156.61 & 156.76 & 0.15 \\ 30 & 156.61 & 155.736 & -0.874 \\ 30 & 156.61 & 156.883 & 0.273 \\ 70 & 156.61 & 154.375 & -2.235 \\ 110 & 156.61 & 153.617 & -2.993 \\ 140 & 156.61 & 153.912 & -2.698 \\ 0 & 231.88 & 229.536 & -2.344 \\ 30 & 231.88 & 228.591 & -3.289 \\ 70 & 231.88 & 228.392 & -3.488 \\ 110 & 231.88 & 227.693 & -4.187 \\ 140 & 231.88 & 226.905 & -4.975 \\ 0 & 327.47 & 329.598 & 2.128 \\ 30 & 327.47 & 328.736 & 1.266 \\ 30 & 327.47 & 330.668 & 3.198 \\ 70 & 327.47 & 328.555 & 1.085 \\ 100 & 327.47 & 328.663 & 1.193 \\ 110 & 327.47 & 326.951 & -0.519 \\ 140 & 327.47 & 326.233 & -1.237 \end{pmatrix}$$

💾
E:\Calibr_Xens.csv

Utab

Utab is a tabulated calibration function; it is saved as an array of function values having temperature (in Kelvin) as a point number (starting from 0).

Figure B.2: Mathcad program for thermopile calibration (Part 2)

Function F(T) corresponds to the function defined by equation (3.6) on page 43; array Utab contains 1001 values of this function at temperatures 0 K to 1000 K. Uexp and Ucalc are arrays of measured and calculated thermopile voltages at melting point of reference metals (indium, tin and lead) at all oven temperatures from the experiment. Deviation of measured temperature δT is calculated as difference between measured and calculated thermopile voltage divided by the thermopile sensitivity (slope of the function F(T)) at the temperature of the hot junction of the

thermopile (melting of the corresponding reference metal Tm$_i$). Values of δT from -5.0 K to +3.2 K show that simple quadratic function does not fit the data in such broad temperature range. Therefore, only indium data were used for calibration in this work.

Resulting calibration curve is saved to E:\Calibr_Xens.csv file. This file contains one column of values of calibration function F(T) with a step of 1 K; line number corresponds to an absolute temperature in K (starting from 0). This makes the format universal for exchange between different applications; it is also optimized for fast calculations in LabVIEW using built-in functions (Interpolate 1D Array, Threshold 1D Array).

Appendix C. LabVIEW software for calorimetric measurements

C.1. User interface

Calorimeter control software is written in LabVIEW. Front panel is presented in Figure C.1.
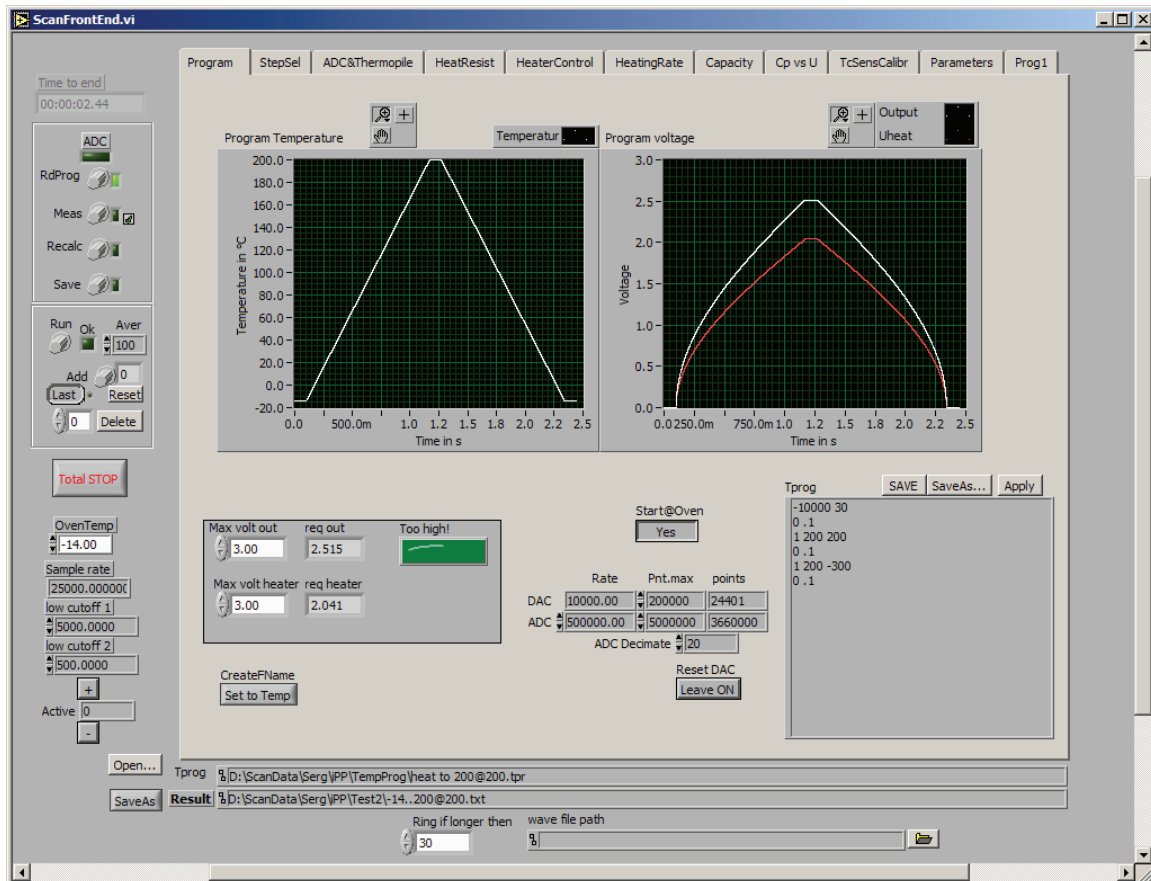
Figure C.1: Front panel of the software – temperature program

Main buttons are on the left side. In the first block, "RdProg" reads the temperature program; "Meas" starts the measurement; "Recalc" recalculates the last result with new parameters (for example if a "filter cutoff frequency" was changed); "Save" saves the result.

The software has two memory buffers for the measurement, a "Last measurement" and an "Average memory". "Last measurement" is updated each time a measurement is started. It can be saved into the "Average memory" then to average over several runs for improving the signal-to-noice ratio. Second block of buttons controls usage of this "average memory". Button "Add" adds the last measurement to the "average memory". A "Run" button runs a measurement automatically and saves the result into the "Average memory" until "Aver" measurements are asquired. A button with "Last" chooses to show (and save) either the last measurement or from the average memory (it

changes to "Aver" then). A selector on the left side selects either a single measurement (value between one and number of measurements) or the average of all measurements (value of zero). Button "Delete" deletes the selected measurement from the average memory.

Next field, "Oven Temp" should be set to the oven temperature as read by the external thermometer before applying the temperature program. It is not automated because change of this parameter implies recalculation of the temperature program and this will influence comparability of different measurements in a series. "Sample rate" indicator helps to choose right values for filter frequencies. "Low cutoff 1" is low cutoff frequency of a Low Pass Butterworth Filter that is applied to raw ADC signals of temperature, heater voltage and heater current. An additional Low Pass Butterworth Filter with "Low cutoff 2" frequency is applied to heating rate and "power to the sample" before they are divided to obtain heat capacity.

"Open…" and "SaveAs" buttons are similar to "RdProg" and "Save", but ask for a filename first. A "Total stop" button terminates program execution.

Each measurement is defined by its temperature program. Time-temperature profile consists of a sequence of segments, or "steps". Each step can be either isothermal or a ramp (heating or cooling) with a constant rate. The first step starts at the "start temperature", which can be either the oven temperature or the value from the temperature program depending on the "Start@oven" button on the front panel (Figure C.1). Each following step starts at the end temperature of the previous step. Step types are described below; they are summarized in Table C.2. The temperature program can be edited inside the software and saved to or loaded from a text file (file extention .tpr is used); the file can be edited using any text editor.

Temperature program file has following structure. First line consists of 2 to 6 parameters as shown in Table C.1.

Table C.1: First line of the temperature program

N_Points (>0) -|DAC_Rate| (<0)	StartTemp(°C)	ADC	Decimate	Low Cutoff 1	Low Cutoff 2

First parameter controls the DAC update rate. Positive value means the total number of DAC points for the temperature program. If the value is negative then its modulus is DAC rate in Hz. **Second parameter** is starting temperature in °C. It is used if the front panel button "Start@oven" is set to "No". This parameter is useful for example if the sample was annealed at some temperature above the oven temperature and the measurement should start from the annealing temperature. **Third parameter** (if present) specifies ADC rate of each ADC channel in conversions/s. If ADC module consists of a multiplexer and single ADC converter (board from Measurement Computing),

actual ADC rate is triple of this parameter; in the National Instruments unit with one ADC per channel, this parameter sets rate of each ADC. **Fourth parameter** (if present) sets a decimate factor. After ADC data acquisition, each [decimate] ADC values in every channel are replaced by one average value to reduce data size; higher ADC rate with decimation is used to enhance signal-to-noice ratio. **Fifth parameter** (if present) is "low cutoff 1" and **sixth parameter** (if present) is "low cutoff 2" frequencies in Hz. If any parameter is present, then all previous parameters should be present too.

Each of the following lines in the temperature program represents one program step and has a structure defined in Table C.2. Starting temperature of each step is the end temperature of the previous step; first step starts at the oven temperature or at the temperature defined in the first line of the temperature program, depending on the "Start@oven" button on the front panel.

Table C.2: Temperature program: second and following lines

1st value	2nd value	3rd value	remark
0	wait (s)	\<not used\>	(isotherm)
1	rate (K/s)	EndTemp (°C)	(ramp to)
2	rate (K/s)	TempStep (K)	(ramp by)

First value in the line defines a step type. For isothermal step (type "0"), only its duration is given. For "ramp to" step (type "1"), parameters are absolute value of the heating/cooling rate and the end temperature in ° C. A "special value" of -300 is automatically replaced by the "start temperature". This makes no limitation, as real temperature cannot be below -273.15 °C. "Ramp by" step is similar to "ramp to"; but the last value ("TempStep") specifies a difference between the end temperature and the start temperature of the step. Any positive and negative values of "TempStep" (including values below -300 K) are considered as valid temperature difference.

Table C.3: Temperature program for heater calibration. Temperature amplitude (here 50 K) is marked red.

-10000	30	500000	20	5000	500
0	.1				
2	200	50			
0	.1				
1	200	-300			
0	.1				

At the beginning of the work with the system and after change of conditions (new sensor; change of the oven temperature, surrounding gas composition or pressure) one should perform a calibration scan with small amplitude and update the calibration functions – heater resistance versus sample temperature $R_h(T)$ and heater power versus overheating $P_h(\Delta T)$.
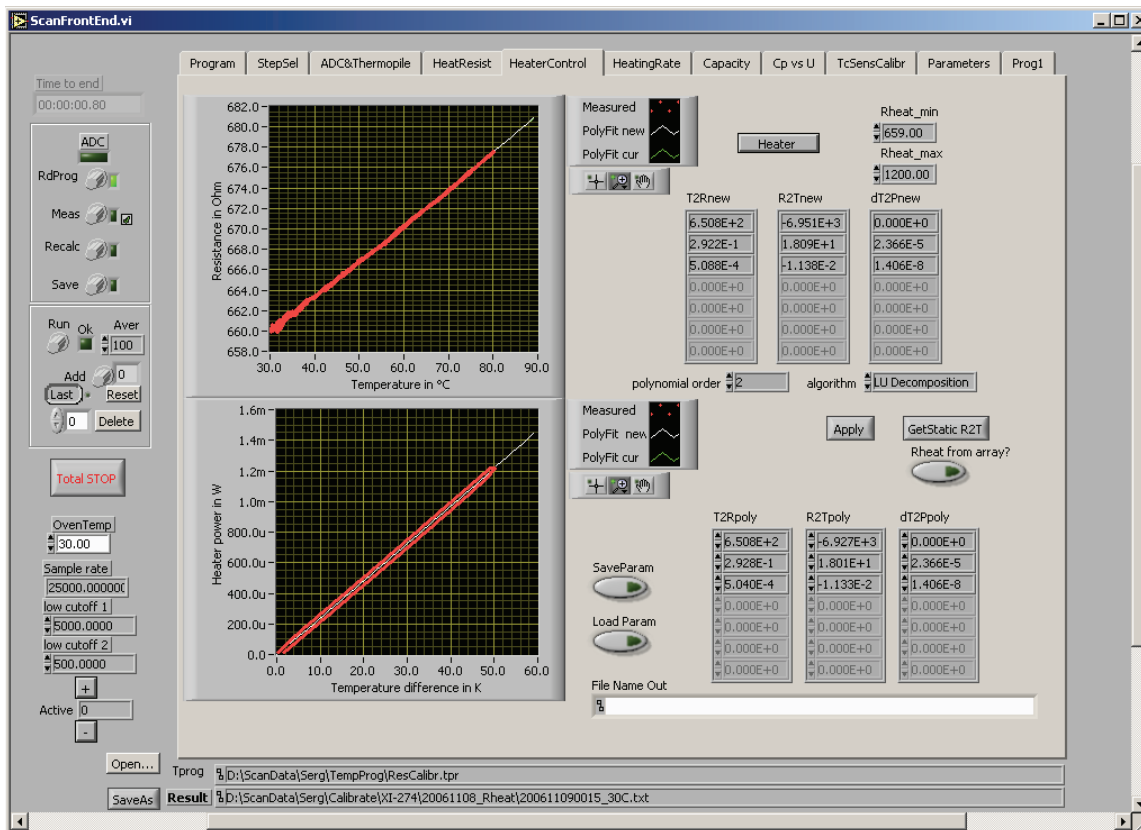
Figure C.2: Heater control parameters

These functions are represented as polynomials with coefficients T2Rpoly and dT2Ppoly on the "HeaterControl" tab (Figure C.2). "Current" coefficients are replaced by the new values from the last measurement T2Rnew and dT2Pnew using the "Apply" button (R2Tnew is also copied into R2Tpoly). Then the amplitude can be increased up to the desired value and $R_h(T)$ and $P_h(\Delta T)$ calibration functions are applied again (this may be done in several steps). Temperature program like the one shown in Table C.3 was used for most of calibrations.
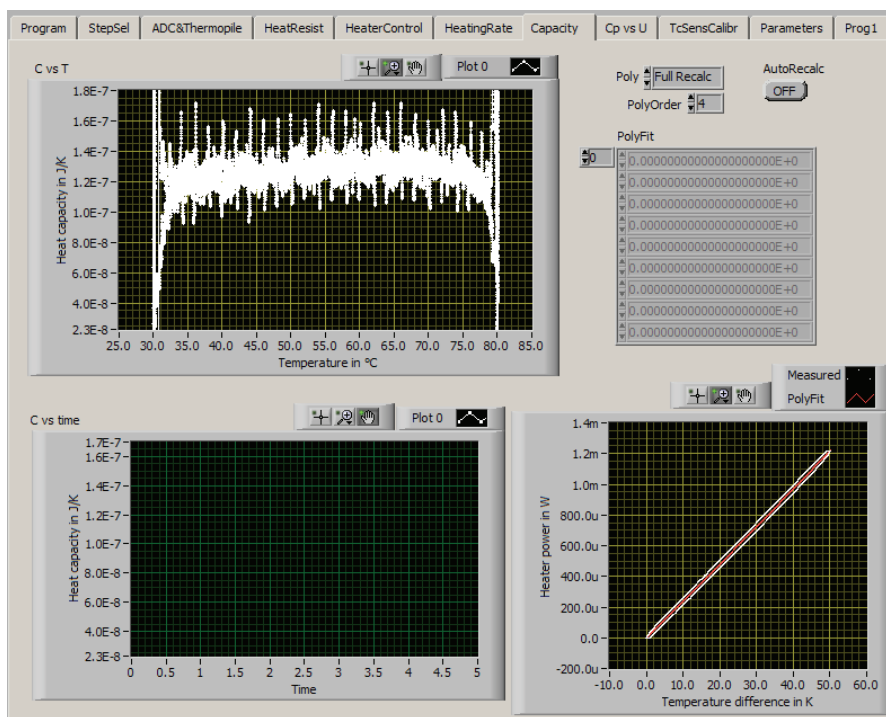
Figure C.3: Heat capacity

When heater calibration is done the desired temperature program for the sample can be run. Heating rate versus temperature ("HeatingRate" page) is useful to see if any transition occurs in the sample; unlike heat capacity, it is not sensitive to the "heat losses" function. Heat capacity and heat losses are plotted on the "Capacity" page (Figure C.3). Here one chooses mode and polynomial order of the fit for heat losses. "Full recalc" stays for complete fit; "only linear" changes only the slope of the fit function leaving higher order polynomial terms unchanged; "1st and 2nd order" fits only linear and quadratic terms of the polynomial; "Frozen" does not change the heat losses function. In any case, constant coefficient is kept zero because heat losses are zero at zero power. During experiments, options "only linear" and "1st and 2nd order" did not bring better results then "Full recalc".

Heat capacity during a single step of the temperature program can be checked in the "StepSel" page. This is useful for example to distinguish between first heating and heating after crystallization, because these data can be overlapped in the heat capacity page.

Special page "Cp vs U" shows heat capacity as function of thermopile voltage instead of temperature; this is the best representation for temperature calibration of the thermocouple.
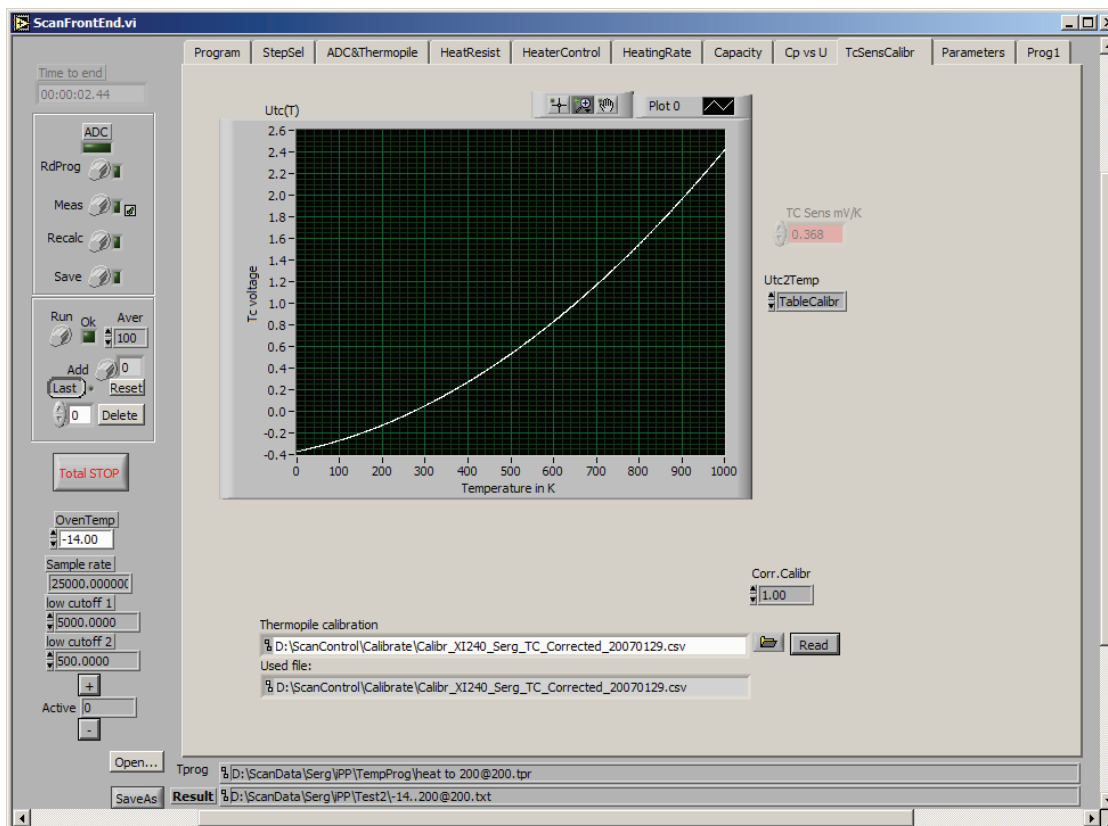
Figure C.4: Thermopile calibration

"TcSensCalibr" page (Figure C.4) contains controls to choose constant thermopile sensitivity or calibration file. Here one can set correction factor to use calibration files created with the old setup (30 kΩ thermopile connected to the amplifier with input impedance of of 200 kΩ) in the new setup (1 MΩ input) and vice versa. One can choose also linear calibration and set sensitivity in μV/K.
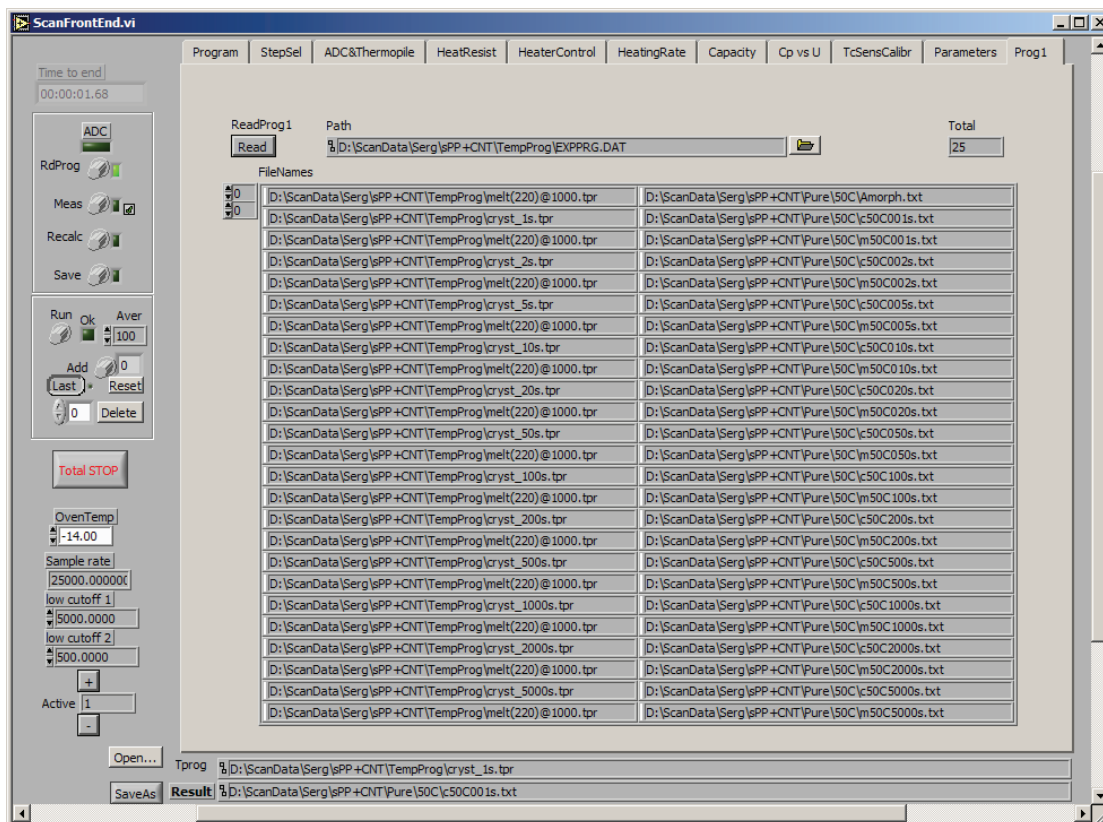
Figure C.5: Program of experiments

"Prog1" page (Figure C.5) allows automation for series of experiments. The table contains two columns. In the first column, one writes filenames of temperature programs; second column contains filenames to store corresponding results of the measurement. This table can be read from the text file. In the test file, each line contains two filenames separated by a single tab character.

C.2. Internal corrections

Hardware trigerring for the beginning of the measurement did not work properly on the board from Measurement Computing; therefore, the software gives a "start" command separately for ADC and then for DAC part of the board. Execution time of the command produces a delay between data acquisition and generation of a waveform; this delay is usually between 8 ms and 13 ms and it is not reproducible. As heater voltage and current are measured synchronously with thermopile voltage, this time shift is not important for evaluation of a single measurement. However, for averaging over several measurements it becomes important. Therefore, the measured data are shifted along the time axes before storing into the average buffer. To calculate the shift factor, the voltage on the DAC amplifier output is calculated as a sum of the measured heater voltage and the voltage drop on the reference resistor. Only heater voltage is less suitable because of change of the heater resistance

during the measurement. In both programmed DAC voltage and measured DAC voltage, amplitude is calculated and then the time is defined, when the value crosses for the first time a level of 5 % of the amplitude. The difference in these two times gives the shift factor. As ADC starts before DAC, corresponding number of points are removed from the beginning of each ADC array. Thise points are added to the end of the array to presume the length. This procedure was not needed with hardware from National Instruments as simultaneous acquisition and generation was garanteed by the hardware.

One should mention the problem of zero drifts of the amplifiers and ADC's. Before the correction, especially near zero voltage, the apparent heater resistance showed strong nonlinear temperature dependence due to the zero shifts in the electronics. The following correction was implemented in the software. The temperature program should start with isotherm at oven temperature, i.e. zero heater voltage. Readout of each ADC is averaged over this interval and the mean value is subtracted from the corresponding channel readout in the whole measurement. A 0.1 s isotherm at the beginning was typically used; the "averaging time" was set to 0.08 s. The difference of 20 ms is to cover the fact that simultaneous start of ADC acquisition and waveform generation by DAC did not work, so they were started one after another. The delay was usually between 9 and 13 ms. If the measurement starts from non-zero heater voltage (for example, after very long crystallization) then one can define "zero averaging" segment at the end of the measurement. To indicate this, negative value for the averaging time is set in the software. Zero correction can be disabled by setting "averaging time" to zero.

C.3. Software structure

The software consists of a main loop with following actions executed in parallel:

❖ Automation for series of experiments – stacked sequence

1. Frame 0: if "ReadProg1" on "Prog1" page is pressed, read FileNames (table of filenames for temperature program to read and result of measurement to save)

2. Frame 1: if "Next" or "Prev" is pressed, get filenames for temperature program and result; activate "Read temp. program" button

❖ TC Calibration

1. If "Read TC calibr" button is pressed or first time execution, read calibration table into global variable "TC calibr array"

❖ Temperature program: If "Open", "RdProg", "Apply", "SaveTProg" or "SaveTPAs" is pressed, then…

1. Module "ProcessTProg.vi"

    1.1. If "Open" is pressed, ask for file name to open

    1.2. If "SaveTPAs" is pressed, ask for filename to save

    1.3. If "Open" or "RdProg" then read temp. program else convert spaces to tabs

    1.4. If "SaveTProg" or "SaveTPAs" then save temperature program

2. "Tprog2array.vi" interprets text temperature program and forms an array of values

3. "RateAdjust_DAC.vi" adjusts DAC rate to the nearest possible from the hardware

4. "RateAdjust_ADC.vi" adjusts ADC rate

5. "Decimate", "Low Cutoff 1" and "Low Cutoff 2" are updated if >0

6. "Calc_DAC_array.vi" calculates an array for program temperature as function of time tabulated at DAC rate

7. "CalcHeaterVolt.vi" calculates an array for heater power using dT2Ppoly polynomial coefficients and an array for heater resistance using T2Rpoly polynomial coefficients. These two arrays and amplifier output resistance, reference resistor resistance and output amplifier gain are used to calculate DAC voltage, amplifier output voltage and heater voltage as functions of time. Maximum voltages on the output and on the heater are compared to the allowed values specified on the "Program" page; further operation is disabled if any value exceeds the limit.

8. "FindCrossXDouble.vi" finds the time when the threshold value (usually 5 %) of the amplifier output voltage is crossed for the first time. Threshold is given in the "DAC Threshold" global variable being "0" the minimum value in the array and "1" the maximum value in the array. "FindCrossXDouble.vi" guarantees proper operation in both cases if starting value is above the threshold and starting value is below the threshold. If the threshold is set to zero the functionality is disabled; "FindCrossXDouble.vi" returns 0 as time shift. Result is stored in the "Time 0.05 Tprog" local variable.

❖ Measurement

1. Calculate number of ADC points and compare with limit. If number of ADC points is greater then the maximum allowed number and button "Measure" is pressed, display an error message. (Run command) is (Measure or (Run and Calculated)). If (number of ADC points OK, temperature program OK and (Run command)) then continue, else break.

2. "ReadArray.vi".

    2.1. ADC and DAC are prepared for burst operation at given rates. DAC array is sent to the DAC buffer.

    2.2. ADC and DAC are started simultaneously (system from National Instruments) or one after another (Measurement Computing).

    2.3. During the measurement, "Time to end" shows the remaining time.

    2.4. "ADC_Shift_gain.vi".

        2.4.1. Decimate all three channels according to "ADC decimate"

        2.4.2. Calculate number of points corresponding to "Sec to average for 0"; correct each channel for zero shift with "SubtractStartMeanDbl.vi"

        2.4.3. Calculates voltages according to input amplifier gains

    2.5. Store voltages to "Store_ADC.vi"

3. Display ADC voltages (calculated to inputs of amplifiers) in the "ADC readout in V" graph on the "ADC&Thermopile" page

4. After the measurement, "Data ready" is set and "Recalc" button is activated. If the measurement was longer then "Ring if longer then" seconds, wave file specified in the "wave file path" is played.

❖ If "Utc gain" was changed or first execution of the cycle, update Utc gain in the hardware

❖ If "Recalc" is pressed (Mechanical action: "switch when released") …

1. Frame 0 of stacked sequence: set "Calculated", "Saved" to "False"; release "Recalc"

2. Frame 1 of stacked sequence

    2.1. If "UseLastValue" is set to "Last", take ADC values from "Store_ADC.vi", otherwise from the average memory

    2.2. Apply 2nd order LowPass Butterworth filter to each ADC channel ("FilterADC.vi"), cutoff frequency "Low Cutoff 1"

    2.3. "ADC_TimeShift_check.vi": Calculate voltage on the DAC output measured by ADC (heater voltage plus voltage on the reference resistor); define time of crossing the same level as was calculated for DAC (usually 5 % of the amplitude) and calculate time shift between DAC and ADC.

2.4. Using voltages on the heater and on the reference resistor, calculate heater current, power and resistance; limit resistance values by Rheat_min and Rheat_max from the "Heater_control" page on the front panel ("Calc_Heater.vi")

2.5. Calculate heater temperature based on its resistance using R2Tpoly polynomial coefficients from the HeaterControl page; calculate sample temperature based on thermopile voltage using thermopile calibration set on the TcSensCalibr page ("Volt2°C.vi"); build an array of program temperatures with the same number of points as in each of the two arrays above ("TprogToOut.vi"); plot all three temperatures versus time in the "Sample Temp" graph on the ADC&Thermopile page

2.6. Plot thermopile voltage versus time on the ADC&Thermopile page

3. Frame 2

3.1. "CalcPlost.vi": update polynomial coefficients for heat losses according to setting of "Poly" ("Full recalc", "only linear", "1st and 2nd order", "Frozen"); calculate heat losses and heat flow into the sample for each measured point

3.2. "Calc_Csam.vi": calculate heat capacity. Apply second order Low Pass Butterworth Filter to sample temperature and power into the sample (cutoff frequency "Low cutoff 2"). Calculate heat capacity

3.3. "StepSelect.vi": plot heat capacity data of a single step of the temperature program chosen by StepNum on the StepSel page of the front panel

4. Frame 3: heater parameters

4.1. "GetRange.vi" calculates the first and the last point in the measurement where heater power is above a threshold (field "Level") set on the HeatResist page of the front panel. The threshold is relative to the amplitude; a good value for PXI system is 0.01 (1%)

4.2. Page "HeatResist" on the front panel: in the window defined by "GetRange.vi", heater resistance is polynomially fitted as function of heater power; heater resistance is extrapolated to zero power; the value and corresponding temperature from the static calibration are displayed

4.3. Page "HeaterControl" on the front panel: in the window defined by "GetRange.vi", polynomial coefficients to recalculate temperature into resistance (T2Rnew), resistance into temperature (R2Tnew) and overheating to power (dT2Pnew) are calculated. Resistance versus temperature and heater power versus overheating is shown along with old and new polynomial fit.

        4.4. Set calculated=True; show time of calculation

❖ Process of buttons (stacked sequence)

1. Frames 0 to 2. Process buttons "SaveAs" (measurement); "CreateFName" ("Set to Temp") – set filename to oven temperature; "Match range" on "ADC&Thermopile" page;

2. Frame 3 – buttons on the page "HeaterControl": "Apply" – copy values of T2Rnew, R2Tnew, dT2Pnew into T2Rpoly, R2Tpoly, dT2Ppoly; "GetStatic R2T" – copy parameters R2Tpoly from the static calibration Rheat(T)

3. Frames 4 and 5: load and save parameters T2Rpoly, R2Tpoly, dT2Ppoly

4. Frame 6: reset average memory (button "Reset")

5. Frame 7: set "recalculate" if "PolyOrder" of fit polynomial for heat losses was changed or "AutoRecalc" is "on" ("Capacity" page)

6. Frame 8: add current measurement to the average memory

7. Frame 9: delete selected measurement from the average memory

8. Frame 10: calculate an average of all measurements in the average memory

❖ If "Save" is pressed and data calculated → save the result

❖ If "ADC range" on "ADC&Thermopile" page is pressed → open "AdcDacParam.vi" (This VI is located in the "ScanHard.llb" library and is replaced with change of the hardware)

❖ If "Heater" on "HeaterControl" page is pressed → open "Calc_Heater.vi" (show heater-specific parameters; values in the graphs are updated during "recalculation")

❖ If "Static heater res" on "HeatResist" page is pressed → open "HeatRes_static.vi" (this VI allows to load an external calibration of heater resistance versus temperature)

❖ All the actions above are executed every 20 ms or after completion of the previous cycle.

Acknowledgements

At this point, I would like to thank all the people who stand by my side and made this work possible. This includes also all those who are not specifically mentioned here.

First of all, I am grateful to my supervisor, Prof. Dr. Christoph Schick, who shared his knowledge and experience and made this work possible, for his guidance and full support during the research work as well as writing of the thesis.

I am also thankful to my first scientific supervisor Dr. Alexander Minakov, for introducing me into the research world as well as fruitful discussions and effective collaboration.

My special thank I would give to Dr. Mikhail Merzlyakov for a valuable support when I came to Germany as well as for the idea to use pressure sensor for ultrafast calorimetric measurements.

I would like to thank the members and visitors of the Polymer Physics Group of Rostock University for nice working atmosphere and good work together.

I want to thank my parents for giving me the life and my wife and my son for giving me the feeling of life, now and here, yesterday, today and tomorrow.

Short summary

Present work describes an ultra-fast scanning calorimeter that is capable of controlled cooling and heating at rates up to 100 000 K/s as well as isothermal measurements with time resolution of 0.1 ms. The technique was applied to study crystallization kinetics of polymers and monodisperse n-alkanes. N-alkanes showed discrete values of melting temperature caused by so-called integer folding (extended chain E, folded-into-two F2, folded-into-three F3 and so on). In the isothermal crystallization halftime versus crystallization temperature curve, there is at least one bend. The bend was thought to be due to the transition between the formation of once folded (F2) and extended chain (E). However, the effect is rather caused by the interplay between different processes, each having its own kinetics (crystallization into F2, crystallization into E, transformation F2 $\rightarrow$ E) as well as a self-poisoning effect.

Kurze Zusammenfassung

Die vorliegende Arbeit beschreibt ein ultraschnelles Kalorimeter, das zum kontrollierten Abkühlen und Heizen mit Raten bis zu 100 000 K/s sowie zu isothermen Messungen mit einer Zeitauflösung von 0.1 Millisekunden fähig ist. Die Technik wurde angewandt, um die Kristallisationskinetik von Polymeren und monodisperse n-Alkanen zu studieren. N-Alkane zeigten diskrete Werte der Schmelztemperatur, die durch so genannte Ganzzahlfaltung verursacht sind (ausgestreckte Kette E, "gefaltet in zwei" F2, "gefaltet in drei" F3 usw.). In der Kurve der isothermischen Kristallisationshalbzeit über der Kristallisationstemperatur gibt es mindestens einen Knick. Bisher dachte man, dass der Knick durch den Übergang zwischen der Bildung einmal gefalteter (F2) und ausgestreckter Kette (E) verursacht wird. Allerdings wird der Effekt eher durch das Zusammenspiel verschiedener Prozesse verursacht, von denen jeder seine eigene Kinetik hat (Kristallisation in F2, Kristallisation in E, Umwandlung von F2 in E), sowie einer "Selbstvergiftung".

Eidesstattliche Erklärung

Ich versichere hiermit an Eides statt, dass ich die vorliegende Arbeit selbstständig angefertigt und ohne fremde Hilfe verfasst habe, keine außer den von mir angegebenen Hilfsmitteln und Quellen dazu verwendet habe und die den benutzten Werken inhaltlich und wörtlich entnommenen Stellen als solche kenntlich gemacht habe.

Potsdam, den 21.07.2010   Serguei Adamovski

List of publications

Also online: *http://www.researcherid.com/rid/A-6702-2009*

1. Minakov AA, Adamovsky SA, Schick C: **Simultaneous measurements of complex heat capacity and complex thermal conductivity by two-channel AC calorimeter.** *Thermochim. Acta* (**2001**), 377:173-182.

2. Adamovsky SA, Minakov AA, Schick C: **Scanning microcalorimetry at high cooling rate.** *Thermochim. Acta* (**2003**), 403:55-63.

3. Minakov AA, Adamovsky SA, Schick C: **Advanced two-channel AC calorimeter for simultaneous measurements of complex heat capacity and complex thermal conductivity.** *Thermochim. Acta* (**2003**), 403:89-103.

4. Adamovsky S, Schick C: **Ultra-fast isothermal calorimetry using thin film sensors.** *Thermochim. Acta* (**2004**), 415:1-7.

5. Minakov AA, Adamovsky SA, Schick C: **Non adiabatic thin-film (chip) nanocalorimetry.** *Thermochim. Acta* (**2005**), 432:177-185.

6. Gradys A, Sajkiewicz P, Minakov AA, Adamovsky S, Schick C, Hashimoto T, Saijo K: **Crystallization of polypropylene at various cooling rates.** *Mater. Sci. Eng. A* (**2005**), 413-414:442-446.

7. Tol RT, Minakov AA, Adamovsky SA, Mathot VBF, Schick C: **Metastability of polymer crystallites formed at low temperature studied by Ultra fast calorimetry* Polyamide 6 confined in sub-micrometer droplets vs bulk PA6.** *Polymer* (**2006**), 47:2172-2178.

8. De Santis F, Adamovsky S, Titomanlio G, Schick C: **Scanning nanocalorimetry at high cooling rate of isotactic polypropylene.** *Macromolecules* (**2006**), 39:2562-2567.

9. De Santis F, Adamovsky S, Titomanlio G, Schick C: **Isothermal nanocalorimetry of isotactic polypropylene.** *Macromolecules* (**2007**), 40:9026-9031.

10. Gradys A, Sajkiewicz P, Adamovsky S, Minakov A, Schick C: **Crystallization of poly(vinylidene fluoride) during ultra-fast cooling.** *Thermochimica Acta* (**2007**), 461:153-157.

11. Alig I, Lellinger D, Oehler H, Adamovsky SA, Schick C: **Microcalorimetry for characterization of film formation and cure of coatings and adhesives.** *Progr. Organic Coatings* (**2008**), 61:166-175.

12. Krumme A, Lehtinen A, Adamovsky S, Schick C, Roots J, Viikna A: **Crystallization behavior of some unimodal and bimodal linear low-density polyethylenes at moderate and high supercooling.** *J. Polym. Sci. Part B: Polymer Physics* (**2008**), 46:1577-1588.